Title
BOSE-EINSTEIN CORRELATIONS IN e+e~ COLLISIONS

Author
Juricic, I.

Publication Date
1987-12-01

Lawrence Berkeley Laboratory
UNIVERSITY OF CALIFORNIA
Physics Division

Bose-Einstein Correlations in e^+e^- Collisions

I. Juričić
(Ph.D. Thesis)

December 1987

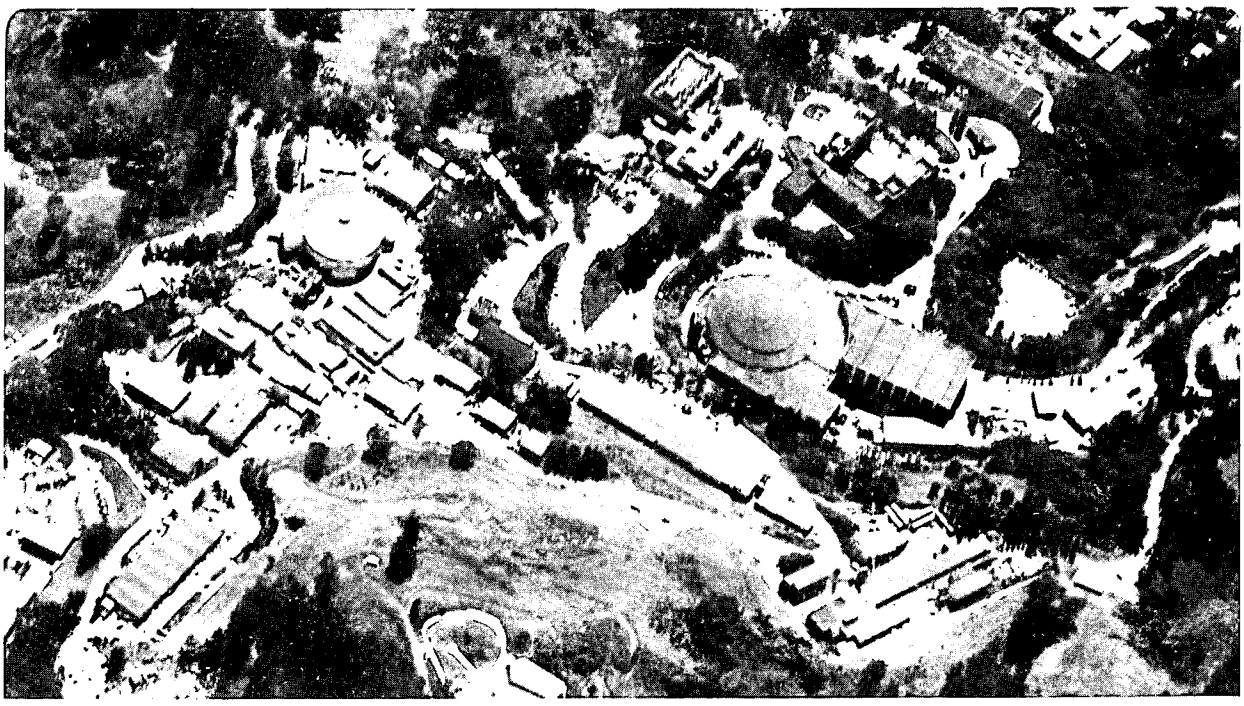

Prepared for the U.S. Department of Energy under Contract DE-AC03-76SF00098

DISCLAIMER

LBL-24493

BOSE-EINSTEIN CORRELATIONS IN e^+e^- COLLISIONS

Ivanna Juričić

(Ph.D. Thesis)

Lawrence Berkeley Laboratory

University of California

Berkeley, California 94720

December 1987

This work was supported by the Director, Office of Energy Research, Office of High Energy and Nuclear Physics, Division of High Energy Physics of the U.S. Department of Energy under Contract Number DE-AC03-76SF00098.

BOSE-EINSTEIN CORRELATIONS IN e^+e^- COLLISIONS

Ivanna Juričić

ABSTRACT

The MARK II detector is used to study the Bose-Einstein correlation between pairs and triplets of charged pions produced in hadronic decays of the J/ψ, the $\sqrt{s} = 4-7\ GeV$ continuum above the J/ψ, two photon events at $\sqrt{s} = 29\ GeV$, and e^+e^- annihilation events at $\sqrt{s} = 29\ GeV$ as a function of Q^2, the four-momentum transfer squared. After corrections for Coulomb effects and pion misidentification, we find a nearly full Bose-Einstein enhancement α in the J/ψ and the two photon data and about half the maximum value in the other two data sets. The radius parameter r (an average over space and time) given by pion pair analyses lies within a band of $\pm 0.10\ fm$ around $0.73\ fm$ and is the same, within errors, for all four data sets. Pion triplet analyses also give a consistent radius of $\approx 0.54\ fm$. Fits to two-dimensional distributions $R(q_T^2, q_C^2)$ of invariant components of $Q^2 = q_T^2 + q_C^2$ give $r_T \approx r_C \approx r$, where q_T is the transverse three-momentum difference calculated with respect to the net pair three-momentum, and q_C is in effect the longitudinal three-momentum difference in the pion pair rest frame. When q_T is calculated with respect to the jet axis for two-jet events in the e^+e^- annihilation data at $\sqrt{s} = 29\ GeV$, a fit to $R(q_T^2, q_C^2)$ also gives $r_T \approx r_C \approx r$. Noting that q_L and q_0 are not invariant, we make fits to $R(q_T^2, q_L^2)$ and to $R(q_T^2, q_0^2)$ (Kopylov formulation), and we find $r_0 \approx r_L \approx \frac{2}{3} r_T$ to $\frac{1}{2} r_T$.

Acknowledgements

A large part of the data used in this thesis was collected with the MARK II before I joined the collaboration. I wish to thank all those who participated in the construction and running of SPEAR, PEP, and the MARK II in its first two incarnations. It has been a priviledge to observe and participate in particle physics done on the front line.

Of the physicists working on the MARK II, two in particular were central to the development of this thesis. I am greatly indebted to my advisor, Gerson Goldhaber, for his guidance, humor, and vision, and for his role in the discovery of the GGLP effect. George Gidal deserves special thanks for his many useful suggestions and interest in this work.

I gratefully acknowledge Mahiko Suzuki for his superlative teaching, his interest in and contributions to the theoretical aspects of the GGLP effect, and for the benefit of his sharp insight.

A multitude of discussions with Dean Chacon have provided me with an excellent first hand education in the GGLP effect in nuclear collision experiments, as well as a better understanding of Life, the Universe, and Everything.

I thank Valerie Heatlie for being a kind friend through some trying times.

My parents' love and support have been indispensable to me in this and all other efforts. I thank my mother for encouraging me to dream, and my father for teaching me how to balance dreams with reality.

Finally, I am especially grateful to my good friend, Uwe Albertin, for his constant encouragement, support, and kindness, his endless patience, keen humor, stunning imagination... and for several "relevant conversations" in the past.

Table of Contents

Chapter 1. THE GGLP EFFECT IN PION PAIRS

1.1 INTRODUCTION

From elementary quantum mechanics we know that the behavior of a wave function of N indistinguishable particles under the interchange of any two of them depends on the nature of the particle statistics. For bosons, which are particles obeying Bose-Einstein statistics, the wave function is symmetrical on such an interchange[1]

$$\Psi(1,2,...N) = \Psi(2,1,...N).$$

This simple requirement leads to an interference term in $|\Psi|^2$, which results in an enhancement in the production of "like" or "approximately indistinguishable" bosons. The precise meaning of "like" will become clear in the next section, when we consider a simple derivation of the interference term.

The enhancement was first noted in 1959 by Goldhaber *et al.*[2] in a study of the annihilation of 1.05 GeV/c antiprotons in a hydrogen bubble chamber,

$$\bar{p} + p \rightarrow N(\pi^+ + \pi^-) + N_0\pi^0,$$

and was interpreted by Goldhaber, Goldhaber, Lee, and Pais (GGLP)[3]. They found that like charged pion pairs were produced with a small relative opening angle more often than unlike charged pion pairs. Figure 1.1, reproduced here from Ref. 3, shows the GGLP distributions of pion pair opening angle for four samples: like charged pairs, unlike charged pairs, and the prediction of a statistical model with and without the Bose-Einstein symmetrization of the multi-pion wave function. The authors found that by using a Bose-Einstein symmetrized wave function in the statistical model they could explain both the like and unlike charged pair opening angle distributions.

The Bose-Einstein enhancement, also referred to as the GGLP effect, has since been observed in a variety of particle production experiments, including heavy

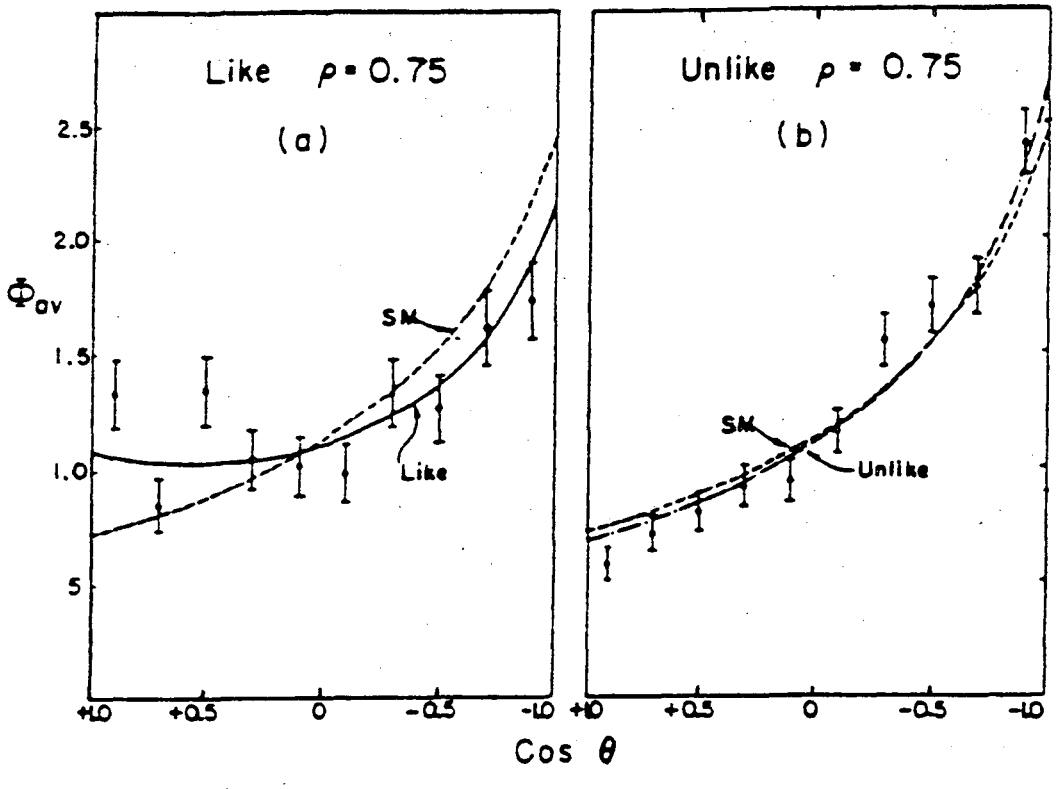

Figure 1.1 *This is a reproduction of Fig.6 from Ref. 3 showing the results of the original GGLP experiment. Figures (a) and (b) show the distributions of pair opening angle for like and unlike charged pairs in the data. The dashed lines are the predictions of a statistical model without Bose-Einstein symmetrization, while the solid lines are the predictions of a modified statistical model which includes Bose-Einstein symmetrization of the wave function.*

ion, hadron, and e^+e^- collisions. Most of these studies have been done with pions. Measurement of the Bose-Einstein enhancement requires high statistics, and the pion is produced more abundantly than any other massive boson because it has the smallest mass. Nevertheless, some work has been done with other particles. Like charged kaon pairs were found to exhibit a similar enhancement[4], while like charged protons show evidence of the analogous Fermi-Dirac depletion[5]. Two reviews of the experimental results can be found in Ref. 6 and Ref. 7.

The Bose-Einstein enhancement is an observable example of an elementary principle at work in the complex process of particle production. As such, it is both rare and elegant. As we will see in the next section, the Bose-Einstein enhancement provides information about the space-time development of the boson source. In the early 1970's, several independent efforts[8,9,10] revived interest in the GGLP effect by showing that it can also be used to study production dynamics.

This breakthrough was a consequence of the analogy between the Bose-Einstein enhancement and second order interference in quantum optics. The work of Hanbury-Brown and Twiss[11] in optical astronomy had shown earlier that second order interference, namely interference in light intensity rather than amplitude, could be used to determine the dimensions of a photon source, such as a star. The analogy between intensity interferometry in optics and the Bose-Einstein enhancement in particle production implies that the GGLP effect provides information about the particle source, including the source dimensions. This is an exciting prospect, since hadronic particle production processes are not well understood. However, although we know that the GGLP effect provides a "microscope" for viewing the hadronic source, the question of what exactly we "see" with it is not firmly established. This is discussed more fully in the next section, where we introduce the *Bose-Einstein correlation function* as the principal tool for investigating the GGLP effect.

The terms *GGLP effect*, *Bose-Einstein correlation*, and *particle* or *pion interferometry* all refer to the Bose-Einstein enhancement in boson production and will be used interchangeably in this thesis.

1.2 THE CORRELATION FUNCTION

1.2.1 Elementary Derivation

Let us consider N point sources radiating pion field with amplitude a_i, where $i = 1, 2, ...N$. The amplitude for the production of a pion with four-momentum k_1 is given by

$$A(k_1) \propto \sum_{i=1}^{N} a_i \exp(ik_1 \cdot r_i),$$

where r_i is the space-time separation between source i and the observation point. Similarly, for the production of a pion with four-momentum k_2,

$$A(k_2) \propto \sum_{j=1}^{N} a_i \exp(ik_2 \cdot r_j).$$

The corresponding single pion production probabilities are

$$P(k_1) \propto \sum_{i,k}^{N} a_i a_k^* \exp(ik_1 \cdot (r_i - r_k))$$

$$P(k_2) \propto \sum_{j,l}^{N} a_j a_l^* \exp(ik_2 \cdot (r_j - r_l)).$$

The amplitude for the joint production of two pions, one with momentum k_1 and one with k_2, is then

$$A(k_1, k_2) \propto \sum_{i,j}^{N} a_i a_j \exp(ik_1 \cdot r_i) \exp(ik_2 \cdot r_j),$$

and the joint production probability is

$$P(k_1, k_2) \propto \sum_{i,j,k,l}^{N} a_i a_j a_k^* a_l^* \exp(ik_1 \cdot (r_i - r_k)) \exp(ik_2 \cdot (r_j - r_l)).$$

Note that these expressions are symmetric on the interchange of k_1 and k_2.

In particle production experiments we can only observe the average of the production probability over all the sources, $\langle P \rangle_N$. The probability of producing two like pions is then given by $\langle P(k_1, k_2) \rangle_N$. The probability of producing two unlike pions is just the product of the single boson production probabilities, $\langle P(k_1) \rangle_N \langle P(k_2) \rangle_N$. We form the following ratio R to compare like pion pair production to unlike pion pair production:

$$R \equiv \frac{\langle P(k_1, k_2) \rangle_N}{\langle P(k_1) \rangle_N \langle P(k_2) \rangle_N}.$$

The analogous quantity in quantum optics involves the averages of intensities and is called the second order correlation function. R is thus often referred to as the *Bose-Einstein correlation function.*

1.2.2 Limiting Cases: Chaotic and Coherent Sources

One of the assumptions made by Hanbury-Brown and Twiss in their derivation of the second order correlation function is that a star is a collection of chaotic photon sources. In the pion model, the chaotic limit corresponds to the case where the pion amplitudes a_i fluctuate randomly over the N sources. Consider the full expression for R, shown in Eqn. 1.1

$$R = \frac{\left\langle \sum_{i,j,k,l}^{N} a_i a_j a_k^* a_l^* \exp(ik_1 \cdot (r_i - r_k)) \exp(ik_2 \cdot (r_j - r_l)) \right\rangle}{\left\langle \sum_{i,k}^{N} a_i a_k^* \exp(ik_1 \cdot (r_i - r_k)) \right\rangle \left\langle \sum_{j,l}^{N} a_j a_l^* \exp(ik_2 \cdot (r_j - r_l)) \right\rangle}. \tag{1.1}$$

If the amplitudes a_i fluctuate randomly over N, then terms with $i \neq k$ and $j \neq l$ in the denominator and ones with $i \neq k, l$ and $j \neq k, l$ in the numerator average out to zero. The expression for R reduces to

$$R_{chaotic} = \frac{\left\langle \sum_{i=k, j=l}^{N} |a_i|^2 |a_j|^2 \right\rangle + \left\langle \sum_{i=l \neq j=k}^{N} |a_i|^2 |a_j|^2 \exp(i(k_1 - k_2) \cdot (r_i - r_j)) \right\rangle}{\left\langle \sum_{i=k}^{N} |a_i|^2 \right\rangle \left\langle \sum_{j=l}^{N} |a_j|^2 \right\rangle},$$

or simply

$$R_{chaotic} = 1 + \frac{\left\langle \sum_{i \neq j}^{N} |a_i|^2 |a_j|^2 \exp(i(k_1 - k_2) \cdot (r_i - r_j)) \right\rangle}{\left\langle \sum_{i,j}^{N} |a_i|^2 |a_j|^2 \right\rangle}.$$

The second term in the last equation is referred to as the *Bose-Einstein enhancement.* We see that if $k_1 = k_2$ we get the maximum enhancement and $R_{chaotic} = 2$. If $k_1 \neq k_2$, then the size of the enhancement depends on the source distribution $(r_i - r_j)$. Thus the behavior of the enhancement term as a function of $(k_1 - k_2)$ gives information about the source distribution.

Now consider the opposite limit, where the N pion sources emit coherently with respect to each other, and there is a fixed relation between the amplitudes a_i. In this case averaging over sources does not result in any simplification of the expression for R. Keeping all the terms in the numerator and in the denominator of Eqn. 1.1, we get

$$R_{coherent} = 1.$$

The coherence of the source, of course, does not eliminate or "turn off" the Bose-Einstein correlation. It merely introduces a correlation (due to the source amplitudes) into all the production probabilities, so that their ratio becomes one.

1.2.3 Between the Limiting Cases: Partially Coherent Source

The measured Bose-Einstein enhancement is often found to be less than maximum, and the result is ascribed to partial coherence of the source. To see how partial coherence acts on the Bose-Einstein enhancement, imagine that the N point sources are grouped into N_c patches of oscillators, and that the sources within each patch radiate coherently with respect to each other to produce a patch amplitude $c_i \equiv c(r_i)$, where r_i describes the location of the patch. Imagine also that the patches radiate chaotically with respect to each other. Proceeding the same way

as in the case of N independent sources, the single pion and joint pion production probabilities are given by

$$P(k_1) \propto \sum_{i,k}^{N_c} c_i c_k^* \exp(ik_1 \cdot (r_i - r_k)),$$

$$P(k_2) \propto \sum_{j,l}^{N_c} c_j c_l^* \exp(ik_2 \cdot (r_j - r - l)),$$

and

$$P(k_1, k_2) \propto \sum_{i,j,k,l}^{N_c} c_i c_j c_k^* c_l^* \exp(ik_1 \cdot (r_i - r_k)) \exp(ik_2 \cdot (r_j - r_l)),$$

and the correlation function R becomes Eqn. 1.2

$$R_{partially\ coherent} = 1 + \frac{\left\langle \sum_{i \neq j}^{N_c} |c_i|^2 |c_j|^2 \exp(i(k_1 - k_2) \cdot (r_i - r_j)) \right\rangle}{\left\langle \sum_{i,j}^{N_c} |c_i|^2 |c_j|^2 \right\rangle}. \qquad (1.2)$$

Note that in the limit of one patch we return to the result for total coherence

$$\lim_{N_c \to 1} R_{partially\ coherent} = R_{coherent} = 1,$$

and if one patch dominates with $|c_n|^2 >> |c_i|^2$, $R_{partially\ coherent} < 2$. This leads us to parameterize R as

$$R = 1 + \alpha(\text{Bose} - \text{Einstein enhancement term}),$$

where α describes the chaoticity of the source:

$$\text{fully chaotic source}: \quad \alpha = 1$$

$$\text{fully coherent source}: \quad \alpha = 0$$

partially coherent source : $0 < \alpha < 1$.

1.2.4 What We Can Learn From the Correlation Function

From the preceding sections it follows that the correlation function provides information about two things: the nature (chaotic or coherent) of the source and the source distribution.

In the simplified pion source model described above, the strength of the Bose-Einstein enhancement term parameterized by α indicates the degree of chaoticity of the source. As we will see in chapter four, the pion production process in our data contains many kinds of correlations, which may or may not include source coherence. These correlations as well as detector performance can interfere with the measurement of the Bose-Einstein enhancement. Careful analysis is required to extract a value for α which measures the correlations due to the source alone.

The simplified model also shows that the behavior of the Bose-Einstein enhancement term as a function of $(k_1 - k_2)$ provides information about the source distribution. In such an interpretation, however, we assume that $\triangle k \equiv k_1 - k_2$ and $\triangle r \equiv r_i - r_j$ are not correlated with each other. If the production momenta are a function of production points, so that $\triangle k$ and $\triangle r$ are correlated, then Eqn. 1.2 will contain this additional correlation within the second term (so called Bose-Einstein enhancement term), and this term will not measure the Bose-Einstein correlation alone.

The interpretation of the parameters describing the GGLP effect is thus highly model dependent. However, a standardized parameterization allows a relative comparison of data sets and contributes to a better understanding of different hadronization processes.

1.3 Models and Parameterizations

In the limit of a continuous source distribution, the quantities in the simple model above become

$$N \to \infty,$$

$$a_i \rightarrow f(r),$$

and

$$R = 1 + \alpha \, |\rho(k_1 - k_2)|^2,$$

where ρ is the Fourier transform of the source distribution f.

In this section we summarize several source parameterizations in order to familiarize the reader with the variables commonly used in GGLP analyses.

1.3.1 Classical Formulation

The classical parameterizations described here are designed for nuclear collision experiments, where the pion sources are considered to be chaotic classical oscillators with lifetime τ: $\exp(-t/\tau)$.

The Gaussian model combines this time dependence with a Gaussian source distribution to give the following expression for R:

$$R_{Gaussian} = 1 + \alpha \frac{\exp(-|\vec{q}|^2 r^2)}{1 + q_0^2 \tau^2},$$

where

$$\vec{q} \equiv \vec{k}_1 - \vec{k}_2$$

is the three-momentum difference of the pions in the pair, and

$$q_0 \equiv |E_1 - E_2|$$

is the energy difference.

The model proposed by Kopylov and Podgoretskii[8] uses the same time dependence but assumes a source distribution corresponding to a sphere of radius r. In this case

$$R_{Kopylov} = 1 + \alpha \left(\frac{2 \mathrm{J}_1(q_T r)}{q_T r} \right)^2 \frac{1}{1 + q_0^2 \tau^2},$$

where

$$\vec{q}_T \equiv \frac{(\vec{k}_1 - \vec{k}_2) \times (\vec{k}_1 + \vec{k}_2)}{|(\vec{k}_1 + \vec{k}_2)|}$$

is the component of the pion three-momentum difference perpendicular to three-momentum sum. The quantity $\vec{q}_T$ is often called the Kopylov variable, and we will refer to the unit axis defined by $(\vec{k}_1 + \vec{k}_2)/|\vec{k}_1 + \vec{k}_2|$ as the Kopylov axis. The variables q_T and q_0 are not kinematically correlated, unlike q_0 and $|\vec{q}|$ which are restricted to one half of the $(|\vec{q}|, q_0)$ plane.

For nearly indistinguishable pions $q_0 \approx 0$ and $q_T \approx 0$. In this limit, the time dependence in the Gaussian and the Kopylov formulations behaves like a Gaussian function. In addition, the Bessel function in the Kopylov formulation is approximated by a Gaussian, since

$$\frac{2J_1(z)}{z} = \sum_{j=0}^{\infty} \frac{(-1)^j}{j!\Gamma(j+2)} \left(\frac{z}{2}\right)^{2j}$$

$$\left(\frac{2J_1(z)}{z}\right)^2 \approx e^{-z^2/2}, \qquad z \to 0.$$

Therefore, in the limit of $q_T \approx 0$ and $q_0 \approx 0$, and absorbing factors of two for convenience, the Gaussian and the Kopylov formulations reduce to

$$R_{Gaussian} = 1 + \alpha \exp\left(-|\vec{q}|^2 r^2 - q_0^2 \tau^2\right)$$

and

$$R_{Kopylov} = 1 + \alpha \exp\left(-q_T^2 r^2 - q_0^2 \tau^2\right)$$

These two formulations are generalized in a commonly used parameterization which assumes a Gaussian distribution of sources in both space and time:

$$R = 1 + \alpha \exp\left(-q_T^2 r_T^2 - q_L^2 r_L^2 - q_0^2 r_0^2\right).$$

The longitudinal three-momentum difference q_L is defined with respect to the Kopylov axis as

$$q_L \equiv \frac{(\vec{k}_1 - \vec{k}_2) \cdot (\vec{k}_1 + \vec{k}_2)}{|(\vec{k}_1 + \vec{k}_2)|}.$$

Parameters r_T, r_L, and r_0 are introduced to describe the source dimensions in the transverse and longitudinal directions and the source lifetime, respectively.

The Kopylov axis determines a unique direction pair by pair and thus can be defined in the pair analysis of any data set. In some data other directions are defined naturally event by event, and these can be used instead of the Kopylov axis to break up $\vec{q}$ into transverse and longitudinal components. For example, in nuclear collision experiments the beam axis enters into the kinematics of pion production and so defines a unique direction in the event. Thus nuclear collision experiments[12] also use $\vec{q}_T$ and q_L determined relative to the beam axis. Another example is provided by data containing hadronic jets, where the jet axis provides a unique direction event by event.

As well as they work in the case of the nuclear pion sources, these formulations are inadequate in describing the hadronic source in e^+e^- collisions. The multitude of partons involved in nuclear collisions can be modeled as a (nearly) continuous distribution of independent chaotic sources. e^+e^- collisions are interactions between two point particles, and assigning a meaningful space-time source distribution is not as straightforward as in the nuclear collision case. In addition, center of mass energies in e^+e^- experiments are typically higher than in nuclear collision experiments, so that e^+e^- produced pions have higher average momenta. Pion momenta in our data are high enough to make a Lorentz invariant formulation desirable. For these reasons we consider an invariant formulation of the correlation function.

1.3.2 Invariant Formulation

Current hadronization models do not explicitly include Bose-Einstein symmetrization and do not offer direct predictions of the hadronic source distribution in space-time. The closest to achieving these goals is the recent work done on the string fragmentation model[13] ,[14] ,[15] to introduce the effects of Bose-Einstein symmetrization in terms of string tension.

Without the guidance of an explicit source model, we adopt the parameter-

ization of Eqn. 1.3

$$R = 1 + \alpha e^{-r^2 Q^2}, \tag{1.3}$$

where

$$Q^2 \equiv -(k_1 - k_2)^2$$

is the four-momentum transfer squared. This expression is invariant and has been shown to describe e^+e^- collision data very well. The parameter r cannot be interpreted as a source dimension in space, but it represents some average of the individual space and time dimensions.

Q^2 can also be written in terms of the invariant mass M_{12} of the pair as

$$Q^2 = M_{12}^2 - 2(m_1^2 + m_2^2),$$

where for a pion pair we get

$$Q^2 = M_{12}^2 - 4m_\pi^2.$$

We can expand Q^2 in terms of q_0 and of the components of $\vec{q}$ transverse and longitudinal with respect to some unit axis $\hat{u}$:

$$Q^2 = |\vec{q}|^2 - q_0^2,$$

$$Q^2 = q_T^2 + q_L^2 - q_0^2 = q_T^2 + q_C^2,$$

where

$$\vec{q}_T \equiv \vec{q} \times \hat{u}$$

$$q_L \equiv \vec{q} \cdot \hat{u}$$

$$\vec{q} = \vec{q}_T + \vec{q}_L$$

$$q_C^2 \equiv q_L^2 - q_0^2.$$

In chapter six we study these variables using two definitions of $\hat{u}$: the Kopylov axis pair by pair in all data, and the jet axis event by event in two-jet data.

To prepare the way for a discussion in chapter six, it is worthwhile to point out several features of these equations. First, the variables q_T and q_C are Lorentz invariant for a boost along $\hat{u}$, while $\vec{q}$, q_0, and q_L are not. Second, the only difference between the classical formulation in the last section and the invariant formulation above is the sign of the q_0^2 term. Finally, note that when $\hat{u}$ is defined as the Kopylov axis

$$\hat{u} \equiv \frac{(\vec{k}_1 + \vec{k}_2)}{|\vec{k}_1 + \vec{k}_2|},$$

there is a simple relationship between q_L and q_0

$$q_L = q_0 \frac{\gamma}{\sqrt{\gamma^2 - 1}},$$

where γ is defined for the pion pair as

$$\gamma \equiv \frac{E_1 + E_2}{M_{12}}.$$

Then

$$q_C^2 \equiv q_L^2 - q_0^2 = \frac{q_L^2}{\gamma^2} = \frac{q_0^2}{\gamma^2 - 1}.$$

From these relationships we see that q_C is just the longitudinal component of the three-momentum difference in the pion pair rest frame.

Our basic measurement of the Bose-Einstein effect is presented in chapter six in the form of a fit to Eqn. 1.3. This parameterization has two major advantages: it is invariant and is commonly used in published literature, making a comparison with other experiments straightforward.

1.4 Goals of This Thesis

This thesis is a phenomenological study of the Bose-Einstein correlation in e^+e^- collisions. The detector used to collect the data, the MARK II, is described in chapter two, and data reduction procedures are discussed in chapter three. In this section we summarize the major aspects of the data analysis, which is done for

pion pairs and triplets in chapters four and five, respectively. Discussion of results is left for chapter six.

1.4.1 *Hadronic Sources in e^+e^- Collisions*

Four separate data sets, representing different kinds of hadronic sources, are used to study the GGLP effect in inclusive pion production.

The first data set consists of e^+e^- annihilation into the J/ψ, at E_{cm} of 3.095 GeV. The J/ψ is the lowest energy charmonium ($c\bar{c}$) state and is not massive enough to decay into charmed mesons. Figure 1.2(a) shows the quark diagram for this favored but energy forbidden decay. Figure 1.2(b) shows the alternative decay mode, where the c and $\bar{c}$ annihilate into gluons, which then hadronize into mesons containing u, d, and s quarks. The J/ψ cannot decay through one gluon, because both the J/ψ and the mesons into which it decays are color singlets. It cannot decay into an even number of gluons, because the J/ψ has charge conjugation quantum number $C = -1$. The simplest decay mode therefore involves three gluons.

Annihilations of e^+e^- at E_{cm} of 4.1 GeV to 6.7 GeV make up the second data set. The center of mass energy in this data is in the continuum above the J/ψ, where charmed meson production is no longer forbidden, but events do not yet show clear signs of jets of produced particles. Figure 1.2(c) shows the corresponding diagram.

The third data set consists of e^+e^- annihilations at E_{cm} of 29 GeV. Like the charm continuum data, these are also $e^+e^- \rightarrow q\bar{q}$ events described by Fig. 1.2(c). Here the center of mass energy is high enough that the $q\bar{q}$ typically produce two or three hadronic jets.

The fourth data set is made up of two photon events at e^+e^- center of mass energy of 29 GeV. A two photon event is one where the colliding e^+ and e^- do not annihilate; rather each radiates a photon, and the two photons annihilate into hadrons. Like their parent photons, the hadrons in these events carry only a fraction of the initial e^+e^- energy. This fraction is between one tenth and one thirtieth in our two photon data. Different hadronization mechanisms are believed to be dominant in different regions of p_T, where p_T is the component of the net

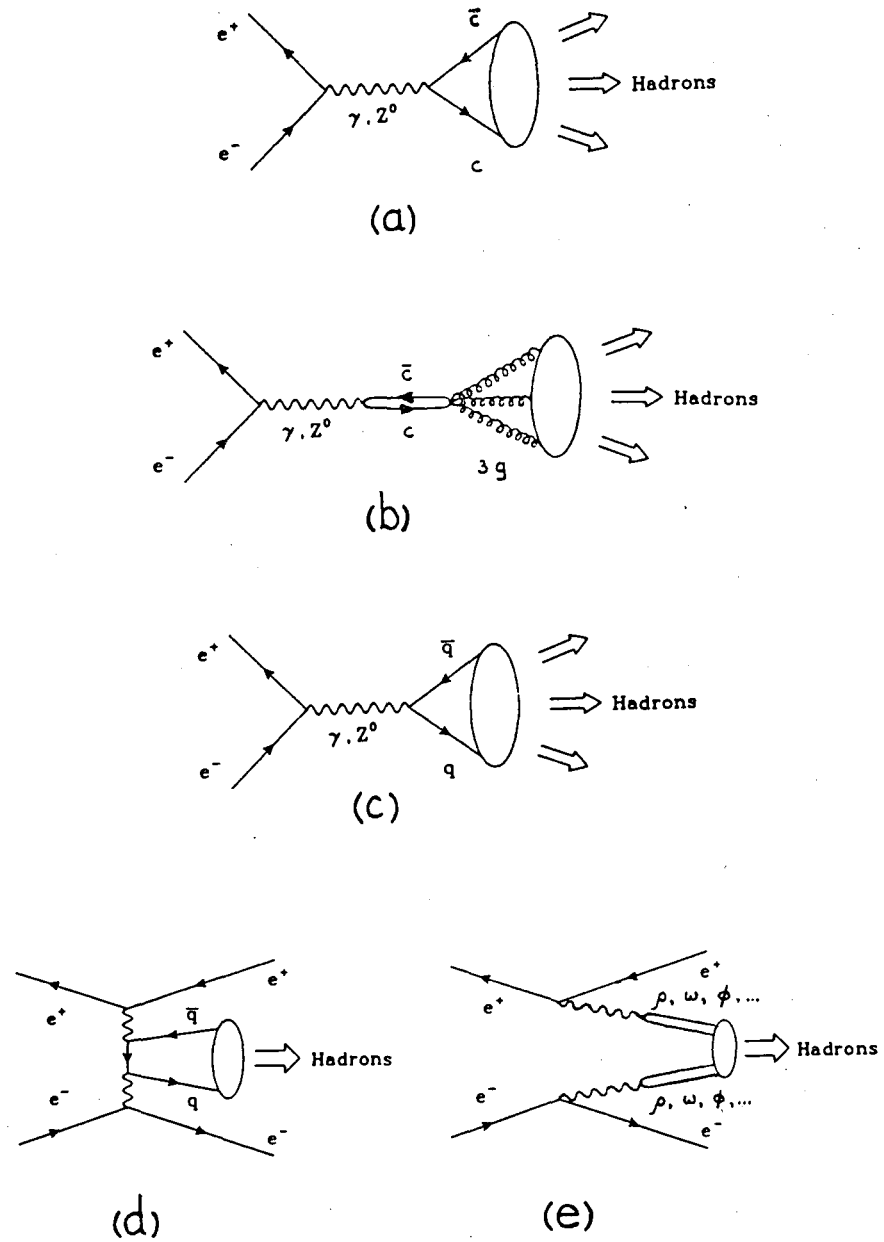

Figure 1.2 *Quark diagrams for different $e^+e^- \rightarrow$ hadrons processes, corresponding to the four data sets studied. The decay of charmonium into charmed mesons (a) is favored over hadronisation through gluons (b), but since (a) is forbidden by energy conservation (b) is the only allowed hadronic decay in the J/ψ data set. The charm continuum and $E_{cm} = 29$ GeV data sets are represented in (c), where e^+e^- annihilate into $q\bar{q}$ which then hadronise. Two photon annihilation in e^+e^- collisions proceeds through $q\bar{q}$ hadronisation (d) at high p_T^2 and through vector meson annihilation (e) at low p_T^2 (Vector Dominance Model).*

hadron three-momentum perpendicular with respect to the beam axis (i.e. the direction of the e^+ and e^- in the event). High p_T means that the radiated photons had a fairly high fraction of the initial e^+e^- energy, whereas low p_T means that the e^+ and e^- lost only a small fraction of their energy in radiating the photons. In the region of high p_T, the two photons annihilate into $q\bar{q}$, as shown in figure Fig. 1.2(d). The quarks then hadronize as in the last two data sets, but the energy available for particle production is of course only a fraction of the original e^+ and e^- energies. In the low p_T region, the Vector Dominance Model (VDM) states that the photons annihilate while in their vector meson form, as in Fig. 1.2(e).

These four data sets give us the opportunity to compare qualitatively some very different hadronic sources. The J/ψ decay to three gluons, as well as the VDM regime in the two photon data, involve more partons in the initial stages of hadronization than the $q\bar{q}$ process. Hence there is some reason to expect that they will exhibit a more chaotic pion source than the latter. We will see in chapter six that the measured values for the parameter α tend to support this interpretation. The full discussion of this and other results in comparing the data sets can be found in chapter six.

1.4.2 Analysis of the GGLP Effect in e^+e^- Collisions

As we saw earlier, a detailed model calculation of the Bose-Einstein enhancement in e^+e^- collisions is not available. Instead, the data being studied is compared to a *reference sample*, free of Bose-Einstein correlations, in order to isolate the Bose-Einstein enhancement in the former. The choice of reference sample is therefore critical to any analysis of the GGLP effect. We use two kinds of reference samples suited to e^+e^- collision experiments. One of these reference samples is commonly used. The other was developed for this analysis.

Both the study sample and the reference sample in general contain correlations other than the Bose-Einstein correlation. A major part of an analysis of the GGLP effect in any experiment is to understand these correlations in both samples and correct for them when possible. Similarly, imperfect detector perfor-

mance affects the measurement of the Bose-Einstein enhancement. These study sample, reference sample, and detector performance effects are discussed for pion pair analysis in chapter four and for pion triplets in chapter five.

1.4.3 GGLP Topics

Finally, we summarize the GGLP effect topics which we will address in chapter six.

The primary goal of this thesis is to compare measurements of α and r in the four data sets using the parameterization of Eqn. 1.3 and to see if the results can be understood qualitatively in terms of the different hadronic sources in the data sets.

For the purpose of comparison with other experiments, we also investigate the Bose-Einstein enhancement in terms of other invariant and non-invariant variables introduced earlier in this chapter.

A derivation of the GGLP effect for pion triplets (chapter five) analogous to the one for pion pairs leads us to expect a similar Bose-Einstein enhancement in triplets. It has not been established whether the enhancement in triplets is merely a reflection of the enhancement in pairs, or whether the triplet enhancement contains additional information. We examine this question using our measured values for pair and triplet enhancements.

Chapter 2. APPARATUS

2.1 INTRODUCTION

The data sets used in this analysis were collected with the MARK II detector during its operation at the SPEAR (1978-79) and PEP (1980-84) e^+e^- collider storage rings located at the Stanford Linear Accelerator Center (SLAC). Relevant parameters of SPEAR and PEP are listed in Table 2.1 .

Table 2.1 *Parameters of SPEAR and PEP collider storage rings.*

Collider Parameter	SPEAR	PEP
E_{cm}	$3-7\ GeV$	$29\ GeV$
ring radius	$32\ m$	$350\ m$
horizontal beam size	$0.27\ E_{beam}\ mm$	$0.48\ mm$
vertical beam size	$0.02\ E_{beam}\ mm$	$0.06\ mm$
size of beam crossing area along beam axis	$32\ mm$	$15\ mm$
time between collisions	$780\ ns$	$2.4\ \mu s$
maximum current per beam	$13\ mA$	$25\ mA$
average luminosity	$6 \times 10^{29}\ cm^{-2}sec^{-1}$	$3.2 \times 10^{32}\ cm^{-2}sec^{-1}$
average number of hadronic events	$\cong$ 2000 per day at the J/ψ	$\cong$ 100 per day

The MARK II is a general purpose magnetic spectrometer designed to study particles produced in e^+e^- collisions. It consists of about half a dozen component systems which specialize in different detection tasks, such as charged particle tracking, electromagnetic calorimetry, and various methods of particle identification. The MARK II has operated in several slightly different configurations as

components were added or upgraded for the move from SPEAR to PEP. The data sets which are studied in this thesis were collected in the SPEAR configuration (data sets at E_{cm} of 3.095 GeV and $4.1 - 6.7$ GeV) and in the longest running PEP configuration (two photon data and annihilation data at E_{cm} of 29 GeV). From here on, the latter will be referred to simply as the PEP configuration.

This chapter contains a description of detector hardware and the event trigger in the SPEAR and PEP configurations. Event reconstruction is discussed along with other data reduction procedures in the next chapter.

2.2 Detector Hardware

Since the MARK II hardware, shown schematically in Fig. 2.1 has been described in great detail elsewhere,[16,17] only a summary is given here. This analysis relies almost exclusively on charged particle tracking by the main drift chamber and on information from the systems used in particle identification (time of flight, liquid argon electromagnetic calorimeter, and the muon system). The small angle tagger is used to tag two photon events. Other important components are discussed below to give an overview of the detector as a whole. They contribute to the analysis indirectly through their roles in the event trigger or their effect on the performance of other systems. Following tradition, the components are described in the order in which they are encountered by the particles produced at the interaction point.

2.2.1 Beam Pipe

At SPEAR the vacuum along the e^+ and e^- beam paths was contained by a 1.5 m long, 0.15 mm thick corrugated stainless steel pipe of radius 7.7 cm. In the PEP configuration, a beam pipe made of 1.4 mm thick beryllium, 1.4 m long and 7.7 cm in radius, was used in order to minimize the multiple scattering contribution to the tracking extrapolation error. A layer of 50 μm tungsten foil lined the inside of the pipe to absorb synchrotron radiation.

The beam pipe at PEP also doubled as the inner wall of the vertex chamber. The outside of the beam pipe was wrapped in a sheet of 50 μm mylar for insulation,

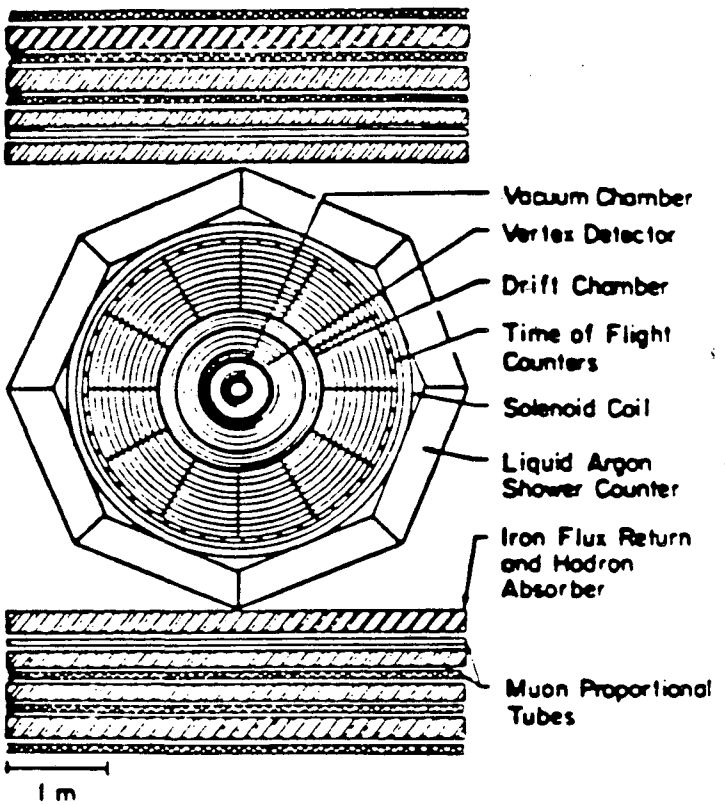

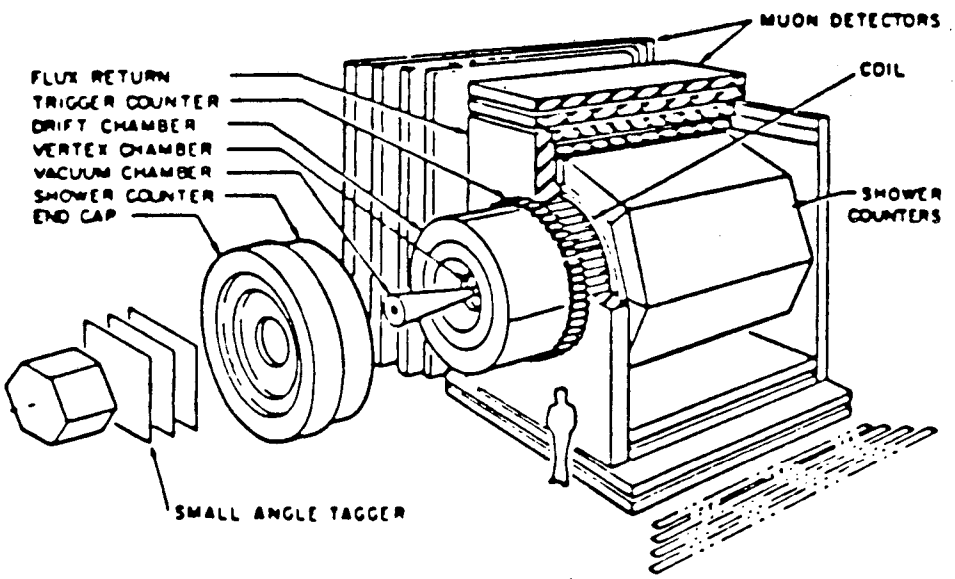

Figure 2.1 *Cross-sectional and isometric views of the MARK II at PEP. In the SPEAR configuration, the small angle tagger and the two outer layers of the muon system were not present, and the space taken up by the vertex chamber was filled by the pipe counter and the trigger chamber.*

followed by a layer of 25 μm aluminum which served as the ground shield of the vertex chamber.

2.2.2 *Pipe Counter*

Surrounding the SPEAR beam pipe were two concentric cylindrical scintillators, each divided into hemicylinders. The scintillators were 81 cm long and 6.4 mm thick, with inner radii of 11.0 cm and 12.5 cm. Their light was passed to photomultiplier tubes for use in the primary trigger logic. There was no pipe counter at PEP.

2.2.3 *Trigger Chamber*

In the SPEAR configuration the space between the pipe counter and the main drift chamber was occupied by the trigger chamber. This was an 86 cm long cylindrical drift chamber consisting of four layers of drift cells providing a resolution of about 300 μm per layer. As its name implies, the trigger chamber was used in the primary and secondary triggers to reject background tracks originating at large distances from the interaction point. Trigger chamber information was not used in charged track reconstruction.

2.2.4 *Vertex Chamber*

The SPEAR pipe counter and trigger chamber were replaced by the vertex chamber[17] at PEP in order to provide more accurate secondary vertex reconstruction. The vertex chamber was a high precision cylindrical drift chamber, 1.2 m long and 0.70 m in diameter. It consisted of seven layers of sense wires grouped into four inner layers, located close to the beam pipe in order to minimize the track extrapolation error, and three outer layers, placed far from the beam axis in order to optimize the track angle measurement. The inner layers had 60 to 75 sense wires per layer at radii of 10 cm to 13 cm, while the outer layers had 180 to 190 sense wires per layer at radii of 30 cm to 32 cm. The whole tracking system, vertex chamber and main drift chamber, was immersed in a uniform magnetic field produced by the

magnet coil. The tracking region of each chamber was a single gas volume filled with a mixture of 50% Argon - 50% Ethane. In the case of the vertex chamber, the operating pressure was 15.5 *psi* (absolute).

Signals from each sense wire were passed through an amplifier and discriminator. Time to amplitude converters compared the discriminator pulses with a reference provided by the beam crossing signal. The pulses were then digitized and corrected for variations in timing offsets and gains. Offline, the measured drift time was converted into a distance of closest approach of the track to the sense wire, taking into account corrections for non-uniformities in drift velocity, the curvature of the ionization cluster trajectories, and the time delay for signal propagation along the wire.

The rms spatial resolution per layer of the vertex chamber was measured to be $\sim 100\ \mu m$, and the rms error on track extrapolation to the origin was given by

$$\sigma_{ex}{}^2 = (95\ \mu m)^2 + \left(\frac{95\ \mu m}{p}\right)^2,$$

where the momentum is in GeV/c. The second term is due to multiple scattering in the 0.006 X_o of material at radii inside the chamber. In addition, the overall momentum resolution of the detector in the PEP configuration was improved substantially by combining the data from the main drift chamber with the tracking information at small radii provided by the vertex chamber. At SPEAR, lacking the vertex chamber, the event vertex could be reconstructed only to about 0.5 *mm* radially and 5 *mm* axially.

This analysis uses the vertex finding capabilities of the vertex chamber only in the search for and elimination of easily identified K^0 and Λ decay products.

2.2.5 Main Drift Chamber

The same main drift chamber[18] was used at both SPEAR and PEP. It consisted of sixteen concentric cylindrical layers of sense wires of lengths ranging from 2.0 *m* in the layer closest to the beam axis to 2.8 *m* in the layer farthest away.

The layers were equally spaced radially, with radii ranging from 41 cm to 145 cm. Six axial layers, with the wires strung parallel to the beam axis, alternated with five right stereo layers and five left stereo layers, where the wires were strung at $\pm 3°$ pitch to provide z information along the track. The wire layers were enclosed in a common gas volume of 50% Argon - 50% Ethane and immersed in a uniform magnetic field produced by the magnet coil.

Main drift chamber signals were processed analogously to vertex chamber signals. They were first passed through a preamplifier and discriminator mounted on the detector, then corrected and digitized by a time to amplitude converter and microprocessor in the counting house, and finally written to tape by the host VAX 11/780 computer. Offline processing combined the measured drift time and the known drift velocity of the ionization signal to reconstruct the distance of closest approach of the track to the sense wire. A separate algorithm decided on which side of the wire the track had passed.

This arrangement allowed charged particle tracking over 85% of 4π and a resolution per layer of about 220 μm. Because the PEP and SPEAR configurations had different magnetic fields and different instrumentation between the beam pipe and the main drift chamber, the rms momentum resolutions were also different. At PEP, the resolution was also improved by combining vertex chamber information with main drift chamber tracking. The resolution in the plane perpendicular to the beam axis was given by

$$\delta p_\perp / p_\perp \cong \sqrt{(0.015)^2 + (0.010 p_\perp)^2}$$

at SPEAR and

$$\delta p_\perp / p_\perp \cong \sqrt{(0.025)^2 + (0.011 p_\perp)^2}$$

at PEP, where $p_\perp$ is in GeV/c. The first term is due to multiple scattering in the material in front of and within the drift chamber. The second term is the intrinsic transverse momentum resolution for a typical track length of about 1 m in the given magnetic field.

2.2.6 *Time of Flight (TOF) System*

Except for a minor change, the hardware of the TOF system[19] was the same in both the SPEAR and the PEP configurations. Forty eight strips of Pilot F scintillator, aligned parallel to the beam axis, formed a ring around the main drift chamber. The strips were 20 cm wide, 3.4 m long, and 25 mm thick. Scintillator light from each end of a strip was passed to an Amperex XP2230 photomultiplier[20] through a lucite light rod, and both the pulse height and the arrival time of the output were digitized. The processed signals were first corrected for pulse height slewing and then used to calculate the time of flight and to associate the TOF hit with a drift chamber track.

Calibration was done online and offline to align the individual time measurements. Online, a nitrogen flash lamp provided an isochronous signal to each scintillator through an optical fiber connected to the center of each strip. This procedure alligned time measurements between the strips to about 100 ps. Offline, further calibration was done by minimizing the variation of predicted and reconstructed times in a sample of Bhabha and muon pair events.

The overall resolution of the TOF system was about 300 ps at SPEAR, giving one standard deviation separation of pions from kaons up to 1 GeV/c and from protons up to 2 GeV/c. To handle the higher average particle momenta at PEP, high resolution time to amplitude converters were installed in the PEP configuration. Unfortunately radiation damage reduced the attenuation length of the scintillator, and the single hit resolution was degraded to about 350 ps for the data taken in the PEP configuration.

The TOF system allowed good pion-kaon separation over most of the observed momentum range at SPEAR. Typical momenta at PEP were significantly higher, so the TOF system provided good separation over a much smaller fraction of the observed momentum range. In this analysis we use the TOF system to reject well identified kaons and protons whenever possible.

2.2.7 *Magnet Coil*

At SPEAR and PEP a uniform magnetic field parallel to the beam axis in the interaction region was supplied by a conventional solenoid magnet located at a radius 1.6 m. The magnet was 1.4 X_o thick and consisted of two layers of water cooled aluminum conductor. At SPEAR the magnetic field was held at 4.06 $kG \pm$ 1.5% in the tracking volume of the main drift chamber. The small variations about the nominal value were measured by a Hall probe and incorporated into the offline tracking fit. The absolute value of the field strength was continuously monitored by a nuclear magnetic resonance probe located near the beam pipe.

For the running at PEP a larger power supply was introduced to raise the nominal field to 4.65 kG, and compensating magnets were rearranged to produce a field uniform to $\pm 0.5\%$. However, an electrical short developed between the two layers of the magnet windings, and it became necessary to power only the outer coil, letting the inner one float. This resulted in a nominal 2.32 kG field. All the PEP data in this thesis was collected with the 2.32 kG field. The magnetic flux return was provided by parts of the muon system.

2.2.8 *Liquid Argon Electromagnetic Calorimeter*

The same liquid argon calorimeter[21] was used both at SPEAR and PEP to detect electromagnetic showers. It consisted of eight self-contained modules arranged like the sides of a barrel around the magnet coil, providing coverage over 65% of 4π. Each module was 3.8 m long, 1.8 m wide, and 0.3 m thick, and was made up of thirty seven planes of 2 mm lead-antimony alternating with 3 mm gaps of liquid argon. Every other lead plane was segmented into readout strips. To allow shower localization, the segmented planes were oriented in three directions: parallel to the beam axis (3.7 cm wide F strips); at 90° to the F strips (5.0 cm wide T strips); and at 45° to the F and T strips (7.4 cm wide U strips). On the side closest to the magnet coil, each module had a section called the trigger gap which was used to calculate corrections for the energy lost in the 1.4 X_o of material in front of the liquid argon calorimeter. The trigger gap consisted of three 1.6 mm aluminum

planes separated by 8 *mm* liquid argon gaps. The middle aluminum plane was segmented into 3.7 *cm* wide readout strips.

To reduce the number of channels of readout electronics to about 360 per module, strips of similar orientation were ganged together in such a way as to optimize the energy resolution as well as information about the spatial development of the shower. The result was seven readout layers in depth, including the trigger gap layer. With the given geometry of the liquid argon calorimeter there was no charge multiplication of the primary ionization in the argon. A completely contained 1 *GeV* shower resulted in an induced charge signal of about 0.5 *pC*, so the signal was preamplified by a charge sensitive, low noise preamp with an FET input. The preamplified signal passed through a shaping amplifier, a sample and hold module, and a microprocessor that performed the analog to digital conversion, and was then written to tape. Showers of energy less than 200 *MeV* could not be distinguished from random noise fluctuations.

Roughly 20% of the particle energy was deposited in the liquid argon, resulting in an rms energy resolution of

$$\sigma(E)/E = 12\%/\sqrt{E},$$

while the spatial resolution was measured to be about 7 *mm* for Bhabha electrons. The overall energy scale was set using non-radiative Bhabha events and scaling to the drift chamber measured momentum.

The major role of the liquid argon calorimeter in this analysis is to reject well identified electrons.

2.2.9 Muon System

The liquid argon calorimeter was enclosed on the top, bottom, and two sides parallel to the beam axis by the four walls of the muon system, which also doubled as the flux return for the magnet coil. At SPEAR each wall consisted of two layers of steel absorber interleaved with two layers of proportional tubes. Two more layers

of steel plus tubes were added to each wall for the running at PEP.[22] The sensitive area of the muon system went from 50% of 4π at SPEAR to 45% of 4π at PEP.

The steel layers varied in thickness from 182 $g\ cm^2$ to 244 $g\ cm^2$. Each tube layer was 4.8 cm thick and was made of extruded aluminum sections honeycombed with tubes of triangular cross section. The tube dimensions and positioning resulted in a 2.5 cm spacing between sense wires, which matched the typical extrapolation error from drift chamber tracking. Tracks were localized by orienting the first tube layer in each wall perpendicular to the beam axis and the remaining layers parallel to the beam axis.

A muon had to have at least 0.9 GeV/c at SPEAR and 1.8 GeV/c at PEP to penetrate through the last layer (second at SPEAR and fourth at PEP). Hadron punch through was less than about 2% at SPEAR and 1% at PEP. Muon identification algorithms used in this analysis are described in the next chapter.

2.2.10 End Cap Electromagnetic Calorimeters

The two ends of the detector perpendicular to the beam axis were also instrumented with electromagnetic calorimeters. At SPEAR one of these end caps consisted of a liquid argon shower detector which followed closely the design of the barrel liquid argon calorimeter, while the other end cap was made of two layers of proportional chambers and lead planes. In the PEP configuration, the liquid argon end cap was replaced by a double of the proportional chamber end cap. The PEP end caps were 4.7 X_0 thick, covered the range of 15° to 40° in the polar angle, and had an rms energy resolution of about

$$\sigma(E)/E = 50\%/\sqrt{E}.$$

Because of their poor energy resolution, the end caps were primarily used as elements in some triggers. End cap calorimetry information is not used in this analysis.

2.2.11 *Small Angle Tagging (SAT) System*

The SAT system[23] at PEP provided tracking and calorimetry at polar angles of 21 *mr* to 82 *mr*. Like the end cap calorimeter, the SAT system consisted of two mirror image groups of components on either end of the detector. A particle coming from the interaction point and entering the SAT region would encounter the following sequence of elements:

1. Three sets of crossed planar drift chambers located between 320 *cm* and 430 *cm* from the beam crossing point. These chambers provided tracking in x and y (the plane perpendicular to the beam axis) with a spatial resolution of about 300 μm.
2. Three layers of acceptance defining scintillator.
3. A 20 X_0 thick lead-scintillator shower counter made of eighteen layers of alternating sheets of 0.25 *in* lead and 0.50 *in* NE114 plastic scintillator, with an rms energy resolution of

$$\sigma(E)/E = 15\%/\sqrt{E}.$$

The SAT system was designed to identify electrons from low momentum transfer Bhabha scattering and from two photon interactions. The rate of small angle Bhabhas also provided an online measure of the luminosity. This analysis uses the SAT system at PEP mainly to tag two photon events.

The analogous system[24] at SPEAR was primarily designed to measure luminosity and consisted of two tungsten-scintillator counters on each side of the detector covering a solid angle of 1.6×10^{-4} of 4π.

2.2.12 *Beam Position Monitor*

Movements of the beam interaction point for different configurations were often greater than the position resolutions made available by the drift and vertex chambers. The beam position monitor[25] (BPM) kept track of these movements online, and mean beam positions were calculated offline.

There were two BPM units, one at each end of the detector 4.9 m from the interaction point. Each unit consisted of four buttons placed on the top, bottom, and two sides of the beam pipe. The voltages induced on the buttons by the passage of electrons were recorded for 96 beam crossings every four minutes during data acquisition. The measurements of relative beam positions within a single data taking run were accurate to 20 μm. Offline, average beam positions derived from drift chamber tracks were compared to the BPM record of relative beam motions.

2.3 EVENT TRIGGER

Events of interest typically include charged particles, so the most useful trigger in a magnetic spectrometer such as the MARK II is based on charged track recognition. Triggers based on patterns in other detector components, such as the calorimeter, become useful in the more complex events at higher E_{cm}.

In both detector configurations the MARK II event trigger[26] was a two level process controlled by the Master Interrupt Controller (MIC) module. If the primary trigger logic found a potentially interesting event, it alerted the MIC module, which then sent out two signals. The first was a wait signal to the detector electronics to prevent a reset. The second was a start signal to the Master Clock (MC) module which controlled the hardware track finding logic. As we will see in what follows, the MIC module made the secondary trigger decision based on the track finding results and on information from other detector components. If the secondary trigger was satisfied, the MIC module sent an interrupt to the host VAX 11/780 computer, which read out detector electronics and wrote the data to tape. When the computer finished reading out the data, or if the secondary trigger was not satisfied, the MIC module cancelled the wait signal, and the detector electronics were reset.

2.3.1 Event Trigger at SPEAR

The primary charged trigger at SPEAR was the coincidence between the beam crossing signal BEAMX, the pipe counter hemicylinders PIPE, and a drift chamber majority DCM. BEAMX was a signal from a beam pickup electrode located

inside the vacuum pipe on the e^- side. DCM was a logical OR of a set of trigger chamber and drift chamber layers. Beam crossing at SPEAR occurred every 780 ns. Since the primary trigger decision was made in about 500 ns, there was more than 200 ns left to clear and reset the detector electronics before the next beam crossing. Primary trigger rates varied between 10 Hz and 1 kHz depending on beam conditions.

If the primary trigger was satisfied, the hardware track finding logic was initiated to search for candidate tracks in the drift chamber. The MC module controlled twenty four curvature modules which scanned the plane perpendicular to the beam axis for drift chamber hits within their specific masks of curvature. A track counter module then collated the hardware tracks into subgroups and sent the results to the MIC module. The track finding process took about 30 μs. The definition of a hardware track was flexible because the curvature modules and the track counter were programmable. For example, a track was labelled an A track if at least four out of the six axial layers in a mask were hit, and there was also an associated TOF signal. A track was called a B track if it had hits in at least three out of the inner five drift chamber layers.

The secondary trigger logic selected events based on programmable combinations of hardware tracks. The "$1\frac{1}{2}$ particle" trigger, for example, required one A track and one B track. Typically two charged tracks, one or both with associated TOF hits, were required. The secondary trigger rate was on the order of a couple of hertz.

2.3.2 Event Trigger at PEP

There were several primary triggers at PEP. The charged track primary trigger required a coincidence between the beam crossing signal BEAMX, a drift chamber majority DCM, and a time-compensated latch from at least one TOF scintillator. The DCM at PEP was a logical OR of a set of vertex chamber and drift chamber layers. The neutral trigger was satisfied if various combinations of liquid argon and end cap modules detected energies above their thresholds. The

thresholds were set at 1 GeV for liquid argon modules and 3 GeV for the end caps. The Bhabha trigger fired if the SAT system detected a small angle Bhabha scattering event. A primary trigger decision was made in under 1 μs, well within the 2.4 μs interval between beam crossings, and the primary trigger rate was about 100 Hz.

Hardware track finding at PEP typically took about 30 μs and was performed by the same MC, curvature modules, and track counter used at SPEAR. Only the shapes of the curvature masks and some of the track definitions were changed. The curvature masks were redefined to improve rejection of background tracks originating at large radii from the beam line. In the more complex event environment at PEP, hardware track definitions were made more demanding. For example, an A track at PEP required hits in at least two out of the four inner vertex chamber layers, at least five out of seven designated drift chamber layers, at least one out of three outer drift chamber layers, and an associated TOF hit.

The secondary trigger could be satisfied in several ways:

1. Two or more hardware tracks were found with momenta greater than 100 MeV/c within the central 75% of the drift chamber tracking volume.
2. Energies above the 1 GeV threshold were detected in the front sections of two or more liquid argon modules.
3. The sum of the signals in all the liquid argon modules, or the sum of the signals in both end caps, or the sum of the signals in the liquid argon and the end caps was greater than 4 GeV.
4. One hardware track was found and one liquid argon module was above threshold.
5. The Bhabha primary trigger was satisfied. Because of its high rate, the trigger for small angle Bhabhas was prescaled by a factor of sixteen.

The typical secondary trigger rate was on the order 1 Hz.

Chapter 3. DATA REDUCTION

3.1 INTRODUCTION

This chapter covers data reduction, by which we mean the steps that lead from the raw detector data read out of the electronics to a sample of pions ready to be analyzed. The first data reduction step is event reconstruction, a process which transforms the raw data into convenient variables such as charge, momentum, energy, and time of flight of particles in an event. The second step is event selection, where a sample of pion rich hadronic events is selected out of the set of reconstructed events. The selection process involves decisions that range from straightforward cuts on particle and event parameters to the fairly sophisticated algorithms used in particle identification.

3.2 EVENT RECONSTRUCTION

The raw event data that was read out of the detector electronics was packed into a large array and written to tape by the VAX 11/780. It included lists of wire numbers and drift times for the tracking chambers, of counter numbers and times for the TOF system, of channels and pulse heights for the calorimeter, and data from smaller systems and monitoring devices. Offline processing was done on an IBM 370/168 for SPEAR data and an IBM 3081 for PEP data. The raw data tapes were run through two production analysis programs called PASS1 and PASS2, which transformed the raw detector information into useful physical quantities such as particle momentum vectors and energies. PASS2 improved on the reconstruction done in PASS1 by using detector constants derived in PASS1.

3.2.1 Charged Particle Tracking

Drift chamber raw data consisted of a list of hit wires and their drift times, ordered by layer and azimuth. The tracking process began with the set of hardware tracks found by the secondary trigger logic. A fast track association algorithm

(TLTRKR) matched hit axial wires with hardware tracks and converted drift times to distances using a constant drift velocity. To decide on which side of the wire the track had passed, TLTRKR used simple circle fits and a constant field approximation. It also searched the list of non-axial wires for hits that could be associated with the track. Because the algorithm had trouble with low momentum or steeply dipped tracks and tracks that were close together, its overall track finding efficiency was $\sim 85\%$. Groups of twelve or more adjacent hits were avoided in this initial pass at track reconstruction because they were often due to showers, grazing tracks, or cross-talk between the wires. Individual hits whose drift times were outside expected limits were also left out.

A more sophisticated tracking program, called TRAKR at SPEAR and PTRAKR at PEP, did the final track finding and fitting. The program performed three tasks:

1. It fitted TLTRKR tracks and made a cut on the χ^2 of the fit.
2. It attempted to find tracks in the set of unused wire hits and to resolve ambiguities.
3. It tried to fit collections of hits where most of the ambiguities were resolved.

The fitting procedure was a linear least squares fit to a helical orbit in the correct magnetic field. The helix parameters were the azimuth (ϕ), the tangent of the dip angle ($\tan\lambda$), the curvature ($1/p\cos\lambda$), and η and ξ which were the distance of closest approach to the origin from two orthogonal directions. In the PEP version of the tracking program the vertex chamber and the drift chamber were treated as a composite tracking system. In this case an additional parameter in the fit allowed for a kink due to multiple scattering at the transition between the two chambers. Requiring the tracks to pass through the beam interaction point as measured by the beam position monitor helped the fit and improved the intrinsic transverse momentum resolution by $\sim 50\%$ at SPEAR energies and $\sim 15\%$ at PEP.

The event vertex was found by taking all the tracks within a 15 cm radius of the beam and finding the point which minimized the summed distance of closest

approach. To minimize displacements of the vertex by strange decays and multiply scattered or poorly measured tracks, any track contributing more than 100 to the χ^2 of the fit was discarded, and the fit was repeated. Further details of the track finding, fitting, and vertexing algorithms can be found in Ref. 19 for the data at SPEAR and Ref. 27 for the data at PEP.

The reconstructed tracks were projected to the TOF, liquid argon, and muon systems and associated with hits there.

3.2.2 Particle Identification with TOF

The raw data from the TOF system consisted of the phototube number, the integral of the scintillator signal pulse height, and the flight time measured by the phototube at a given discriminator threshold. A drift chamber track that projected into the scintillator strip gave the position of the TOF hit along z. The time measurement from each phototube was corrected for time alignment with other phototubes, for time slewing due to pulse height variations, and for travel time along z of the strip. Then the time of flight of the particle was calculated by taking a weighted average of the corrected times from the two phototubes on either end of the active strip. The weighting favored the phototube closer to the track entrance point since photostatistics are better for scintillation light that travels a shorter distance. If the drift chamber indicated that there were two tracks hitting one strip, the time of flight for each was calculated using the phototube nearest to that track in z, and the resolution was degraded to $\sim 500\ ps$ from a single hit resolution of $\sim 350\ ps$.

The mass of the charged particle was determined by combining the time of flight (t) from the TOF counter with the path length (l) and momentum (p) of the corresponding track measured by the drift chamber:

$$m^2 = p^2[(c/l)^2 t^2 - 1]$$

with

$$\delta m^2 = 2p\sqrt{p^2 + m^2}(c/l)\delta t,$$

and $\delta t \cong 350\ ns$. Figure 3.1 is a scatterplot of m^2 versus p, showing the separation of pions, kaons, and protons in a sample of SPEAR events at E_{cm} of 4.5 GeV to 6.8 GeV. The vertical bands centered on ${m_\pi}^2$, ${m_K}^2$, and ${m_p}^2$ widen with increasing momentum and illustrate the range of momenta over which pions can be separated from kaons and protons.

In practice, the mass of the particle was assigned using a weighting technique. The weight for a given mass hypothesis m_i was calculated as

$$W_i = \frac{1}{N} \exp \frac{(t - t_i)^2}{2\sigma^2},$$

where

$$t_i = \frac{l}{pc}\sqrt{p^2 + {m_i}^2},$$

$$N = \sum_i W_i,$$

$$i = \pi^\pm, K^\pm, p^\pm,$$

t is the measured time of flight, σ is the measured TOF resolution, and p is the particle momentum. The section on analysis event selection describes how the weights are used to identify kaons and protons in the four data sets.

Although the TOF system provided good separation between pions and electrons below about 300 MeV, particle momenta at both SPEAR and PEP were typically above that value, and the TOF system was not helpful in electron identification. Further information on TOF data processing can be found in Ref. 28.

3.2.3 Particle Identification with the Liquid Argon Calorimeter

Liquid argon raw data was written to tape as a list of ganged channels and corresponding energies. Figure 3.2 shows the six readout layers and the trigger gap. Our main interest in the calorimeter is its electron identification capability, so the reconstruction algorithms for photons[28] will not be discussed here. Utility algorithms for the identification of electrons and muons have been developed for the MARK II detector at SPEAR and PEP. These are described in detail in Ref. 29,

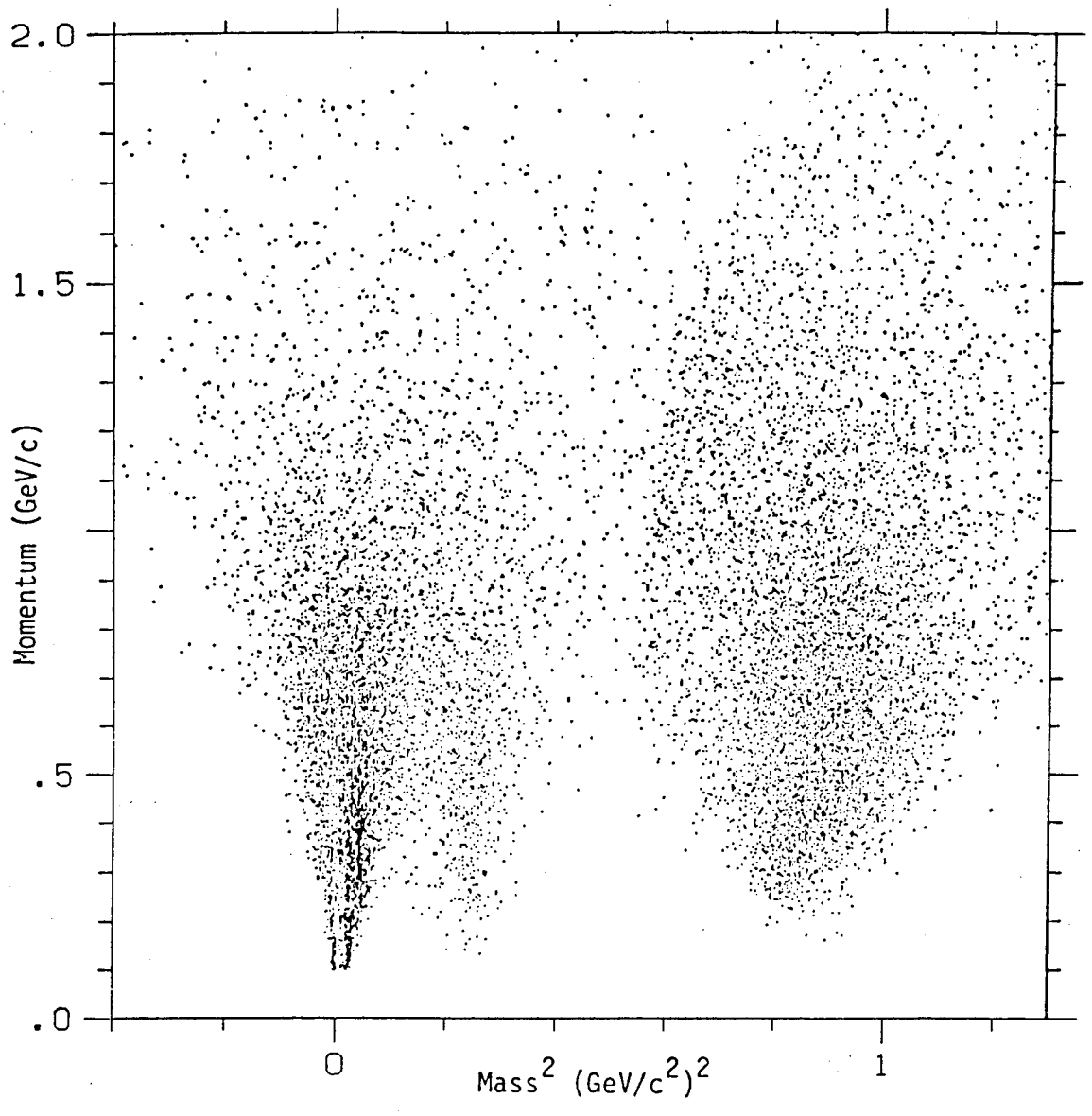

Figure 3.1 *Scatterplot of m^2 versus p for a sample of SPEAR events at* E_{cm} *of* 4.5 – 6.8 GeV.

and only a summary of the electron algorithm is given below. Muons are treated in the next section.

Electron identification is based on the characteristics of the electron's interaction with matter. Bremsstrahlung is the major source of energy loss for electrons with energy above a few MeV. In the MARK II liquid argon calorimeter, an electron with energy greater than about 100 MeV radiates a photon which is energetic enough to produce e^+e^- pairs that radiate in turn and result in an electromagnetic shower. Since the cross section for Bremsstrahlung is inversely proportional to the square of the particle mass, the signature of other massive particles in the calorimeter is typically a minimum ionization track. Occasionally a hadron will interact strongly and lose a fraction of its incident energy in a hadronic shower. Because the interaction length is longer ($\sim$ 17 cm) than the radiation length ($\sim$ 0.6 cm), hadronic showers tend to start deeper in the calorimeter and to exhibit a broader transverse structure than electromagnetic ones.

The MARK II electron identification algorithm used a combination of energy deposition and shower geometry information. The first step was to calculate the path of the incident charged particle through the calorimeter using the projected drift chamber track. A search was then made for energy deposits in nearby channels. The width of the search area was the sum of two terms, the typical width of an electromagnetic shower and a factor that took into account the geometry of the ganging pattern. A channel was included if its center lay within the search area. Typically $\sim 80-90\%$ of the deposited energy in an electromagnetic shower was located within this region. Energy deposits in these channels were summed according to layers into $E_{\mathrm{F1+F2}}$, E_{T1}, and E_{U}, and $E_{\mathrm{front}} \equiv E_{\mathrm{F1+F2}} + E_{\mathrm{T1}} + E_{\mathrm{U}}$. These quantities were used to define

$$E_{\mathrm{min}} = \mathrm{minimum}\left(\frac{E_{\mathrm{F1+F2}}}{\alpha_{\mathrm{F}}}, \frac{E_{\mathrm{T1}}}{\alpha_{\mathrm{T}}}, \frac{E_{\mathrm{U}}}{\alpha_{\mathrm{U}}}, \frac{E_{\mathrm{front}}}{\alpha_{\mathrm{front}}}\right),$$

where the α_i's were chosen to make $E_i > \alpha_i p$ for most electrons (70–90%, depending on momentum p). A particle was an electron candidate if $E_{\mathrm{min}}/p > 1.1$ and if the

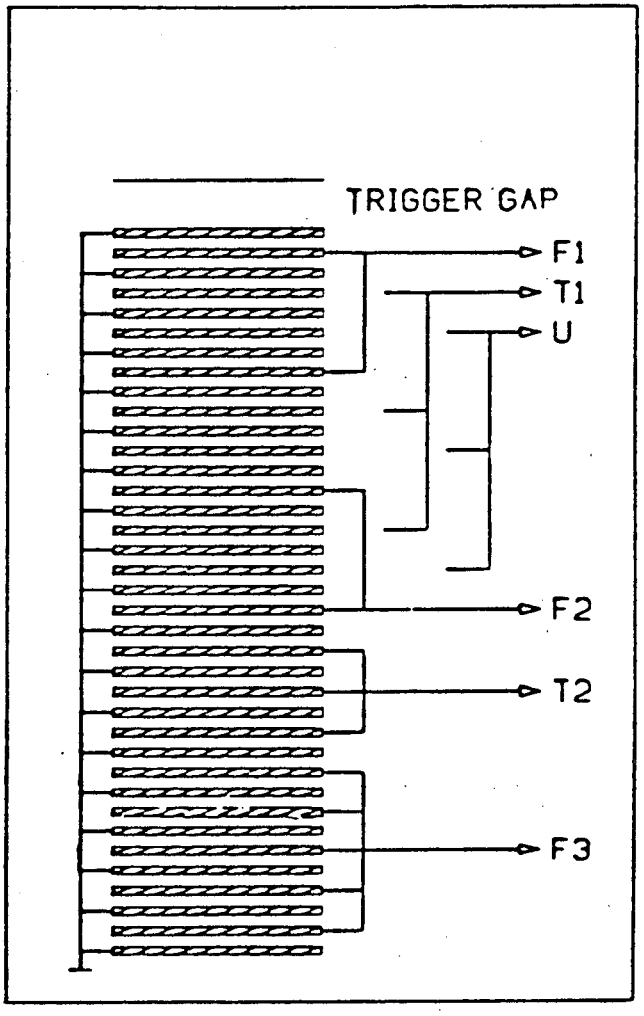

Figure 3.2 *Ganging pattern in the liquid argon calorimeter modules showing the seven readout layers.*

associated shower was not too close to the edge of the liquid argon module.

As discussed in the next chapter, we want to reject as many electrons as possible while losing as few pions as possible in the process. In this case the usefulness of the algorithm is measured by the electron identification efficiency and the pion misidentification probability. For electrons within the sensitive volume of the calorimeter, Fig. 3.3 shows that the identification efficiency varies from $\sim 90\%$ for momenta greater than 2 GeV/c to $\sim 70-80\%$ for 1 $GeV/c < p < 2\ GeV/c$. The efficiency decreases steeply below 1 GeV/c, because electrons with low momenta tend to be close to other tracks, and this worsens the energy overlap problem.

Table 3.1 shows the results of the pion misidentification study done in Ref. 29 using several reliable samples of pions. The hadronic decays $J/\psi \rightarrow 2(\pi^+\pi^-)\pi^0$ from the MARK II running at SPEAR were used to look at pions with momenta $0.5-1.3\ GeV/c$. Another sample was pion beam test data at 2 GeV and 4 GeV taken with one liquid argon module. Both of these indicated that the pion misidentification probability was less than one percent at SPEAR. Two data samples from the running at PEP were also examined: pions from $K^0 \rightarrow \pi^+\pi^-$ and from three pion decays of τ pair events. Because of higher track multiplicities at PEP, track energy overlap became significant enough to increase the pion misidentification as an electron by a factor of about three.

3.2.4 Particle Identification with the Muon System

The MARK II muon system and muon identification algorithm described in Ref. 29 take advantage of the fact that the muon is one of the least interactive massive particles. The muon does not initiate hadronic showers because it does not experience strong interactions, and it typically does not initiate electromagnetic showers because the cross section for muon Bremsstrahlung is suppressed by a factor of $(m_e/m_\mu)^2$ relative to the electron cross section. The main energy loss mechanism for muons above momenta greater than a few hundred MeV is due to ionization of the medium ($dE/dx \cong 200\ MeV$ per interaction length in iron). A muon entering the MARK II muon system (at PEP) at normal incidence requires

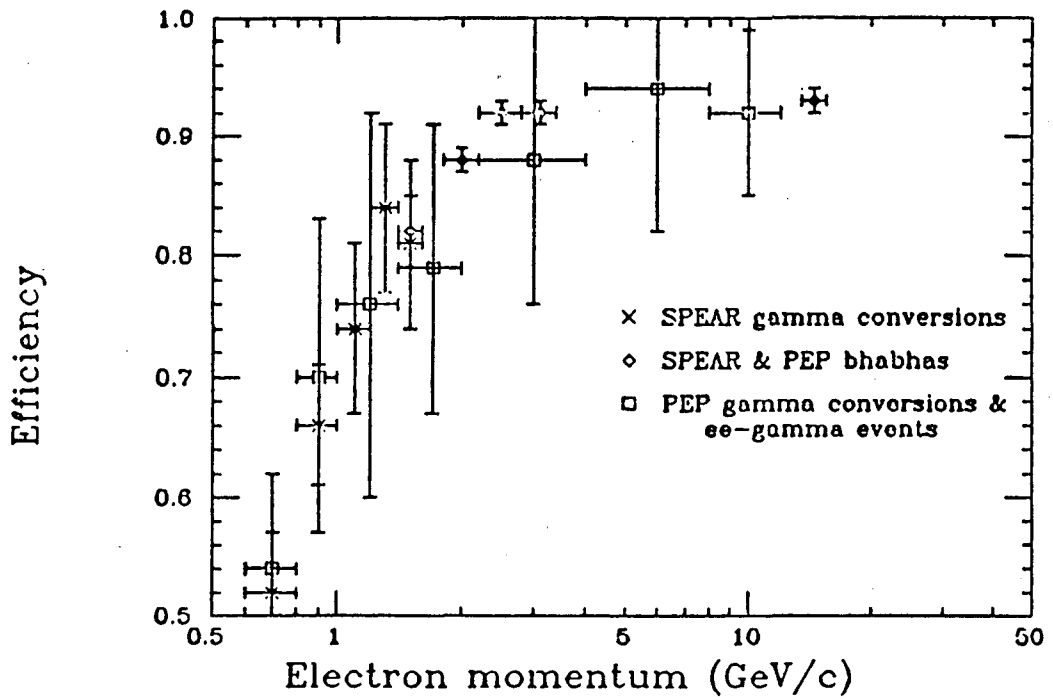

Figure 3.3 *Electron identification efficiency.*

Table 3.1 *Overall pion misidentification probability from Ref. 29. Momenta are given in GeV/c.*

$p \setminus p_T$	$0.0-0.5$	$0.5-1.0$	$1.0-1.5$	≥ 1.5
$1.0-2.0$	0.023	0.010	0.007	0.007
$2.0-3.0$	0.015	0.008	0.007	0.007
$3.0-4.0$	0.010	0.006	0.005	0.005
$4.0-5.0$	0.007	0.005	0.004	0.004
$5.0-6.0$	0.007	0.005	0.004	0.004
≥ 6.0	0.006	0.004	0.003	0.003

a momentum $p \geq 1.5\ GeV/c$ to penetrate all four layers. In general, the signature of a muon is that it penetrates an absorber further than other particles of similar momentum.

The first step of the muon identification algorithm was to project the path of the charged particle through the muon system using drift chamber tracking information. A search was then made in the vicinity for hits in the proportional tube planes. The size of the search area was determined by the tracking projection error, which took into account dE/dx losses, multiple scattering, and bending in the magnetic field due to the flux return. Two variables were formed to summarize the results of the search. MUSTAT was defined as a binary four bit word where each bit corresponded to one layer. A track with an associated hit in layers one and two would have MUSTAT= $0011_2 = 3_{10}$, while hits in all four layers would give MUSTAT= $1111_2 = 15_{10}$. The second variable MULEVE was the number of layers a given muon was expected to penetrate given its momentum and angle of production. The algorithm required that muon candidates satisfy MULEVE= 4 and $p > 2\ GeV/c$.

For tracks within the sensitive volume of the muon system ($\sim 45\%$ of 4π), the muon identification efficiency ranged from $\sim 80\%$ for momenta of $2-3\ GeV/c$ to over 90% for momenta greater than $6\ GeV/c$. Inefficiencies were due to proportional

tube problems and to effects which placed the hits outside of the nominal search area. The latter included range straggling, unusually bad track extrapolation, and multiple scattering losses. Pion misidentification was studied in Ref. 29 to see what fraction of pions penetrated through the muon layers. Table 3.2 shows that the pion punchthrough probability to the third layer was found to be less than a few percent.

Table 3.2 *Measured punchthrough probabilities from Ref. 29. Momenta are given in GeV/c.*

pion sample	momentum	layer 1	layer 2	layer 3
$K^0 \to \pi^+\pi^-$	$2 < p < 6$	0.099	0.034	< 0.011
$\tau \to 3\pi\nu$	$2 < p < 10$	0.215	0.066	0.008
π from D^0	$3 < p < 6$	0.068	0.054	< 0.070

3.3 The Four Data Sets

The reconstructed events were written onto so called PASS2 tapes in the form of arrays containing track and vertex information ready for user analysis. These tapes contained every event that survived reconstruction, including cosmic ray, beam-gas, two photon, and e^+e^- annihilation interactions. Data summary tapes (DST's) were made of specific kinds of events by applying loose cuts to filter out other processes.

As discussed in chapter one, we are interested in hadronic events produced by two distinct processes, e^+e^- annihilation and the two photon interaction, which we abbreviate as e^+e^- and $\gamma\gamma$ for convenience. DST's for hadronic e^+e^- events were made for most of the data collected with the MARK II, and $\gamma\gamma$ DST's have recently been produced for the PEP data. The cuts used to assemble hadronic DST's are looser than the cuts which define a hadronic event in this analysis, so the DST cuts have no effect on the final data sample and will not be discussed here. The $\gamma\gamma$ DST's required similarly loose cuts on the event and the detection of at

least one electron shower of $7-20\ GeV$ in the SAT system, which tagged the event as a $\gamma\gamma$ interaction or a low momentum transfer Bhabha scattering. The selection of hadronic events and the elimination of background processes, including Bhabha scattering, is discussed in the next section.

While nearly all of the running at PEP was at E_{cm} of $29\ GeV$, the operation at SPEAR included energy scans as well as extended runs at several energies in the range of $3.095\ GeV$ to $7.4\ GeV$. By the time this analysis began, roughly 15% of the SPEAR DST's had succumbed to the ravages of time and were unreadable. The PASS2 tapes which were used to make these DST's were too numerous to store for long, so they disappeared into archives soon after the MARK II moved to PEP. They were used less frequently and were probably in even worse condition than the DST's. These factors discouraged the creation of new DST's from archived SPEAR PASS2 tapes as both difficult and haphazard. One set of SPEAR DST's that retains enough statistics to be of use in this analysis is the set of hadronic e^+e^- events at the J/ψ (E_{cm} of $3.095\ GeV$). DST's also exist for hadronic e^+e^- events at E_{cm} of $4.1-4.4\ GeV$, $5.2\ GeV$, and $6.4-6.7\ GeV$, but each of these is too small to be statistically significant on its own. They are added together into a data set labelled SPEAR $q\bar{q}$, which represents a sample of the continuum above the J/ψ.

Data collected during the running at PEP is divided into *good* and *poor* quality data. In the fall of 1982, the MARK II main drift chamber began to draw unacceptably high currents. This phenomenon, also called glow, has been observed in many wire chamber experiments[30] and is usually ascribed to coating of the field wires by products of organic molecules in the chamber gas. In order to continue data taking while the problem was studied, chamber voltages were lowered by $\sim$ $500\ V$ from their optimal values of $3000-3500\ V$, resulting in a degraded drift chamber tracking efficiency. Roughly 40% of the PEP data was collected under these conditions. In the spring of 1983, 0.7% oxygen was added to the drift chamber gas to eliminate the glow problem. The remedy worked, and drift chamber voltages were soon returned to their optimal levels, restoring the original tracking efficiency. Data collected before the glow problem and after the introduction of oxygen is

referred to as *good* PEP data, while data taken with reduced drift chamber voltage is called *poor* PEP data. Two PEP data sets are used in this analysis. One is the set of hadronic e^+e^- DST's made from the good PEP data, and the other is the set of $\gamma\gamma$ DST's made from all the PEP data.

The four data sets we have assembled are summarized in Table 3.3.

Table 3.3 *The four data sets used in this analysis.*

Data Set Name	Process	$E_{cm}(GeV)$	$\mathcal{L}(pb^{-1})$	Comments
SPEAR J/ψ	$\psi \rightarrow$ hadrons	3.1	0.4	hadronic DST's SPEAR data
SPEAR $q\bar{q}$	$q\bar{q} \rightarrow$ hadrons	$4.1 - 4.4$	1.7	hadronic DST's
		5.2	5.1	SPEAR data
		$6.4 - 6.7$	6.4	
PEP $\gamma\gamma$	$\gamma\gamma \rightarrow$ hadrons	29	198.0	two photon DST's all PEP data
PEP $q\bar{q}$	$q\bar{q} \rightarrow$ hadrons	29	113.2	hadronic DST's good PEP data

3.4 Monte Carlo Event Simulation

Monte Carlo data is created in two steps. First, a given model of the hadronization process produces an event consisting of a set of particles and their momenta. This is the Monte Carlo event generator. The particles are then passed through simulations of detector components, where tracking and calorimetric response are modelled. This is the Monte Carlo detector simulation. The resulting Monte Carlo event is written to tape in the form of raw data (drift chamber hits, calorimeter pulse heights, TOF times, etc.) and then processed the same way as a detected event. Monte Carlo data is compared to detected data and is used to study the event generator or the detector simulation.

Ideally, we would like to have four Monte Carlo data sets, corresponding to the four data sets. These Monte Carlo data sets are: a J/ψ event generator

with SPEAR MARK II simulation; a $q\bar{q}$ event generator with SPEAR MARK II simulation; a $\gamma\gamma$ event generator with PEP MARK II simulation; and a $q\bar{q}$ event generator with PEP MARK II simulation. However, this is not possible. We found that the code for the SPEAR MARK II detector simulation, specifically the tracking routine used on the SPEAR data, no longer exists in a usable form. While the PEP MARK II tracking routine is still fully functional, an event generator for $\gamma\gamma$ events is not available to us. These are the major reasons why we are limited to only the last Monte Carlo data set listed above, which was created using the Lund string fragmentation model [31] in the event generator. Since this Monte Carlo data is made to reproduce the PEP $q\bar{q}$ data set, we refer to it as the MC PEP $q\bar{q}$ data set.

Despite the variety of the detected data sets and the scarcity of Monte Carlo data sets, we are still able to accomplish two critical studies of detector performance: pion misidentification and tracking efficiency. The major detector component involved in pion identification is the TOF system. Its performance was essentially unchanged in the transition from SPEAR to PEP, so that the PEP MARK II simulation of the TOF system is nearly the same as the SPEAR MARK II simulation of the TOF system. As discussed in section 4.6.1, this fact allows us to get an accurate estimate of the pion misidentification fraction in all the detected data sets. The study of tracking efficiency requires the full tracking code, so the MC PEP $q\bar{q}$ data allows us to study only the PEP data sets. However, based on these results and on a comparison of known tracking efficiencies, we can make some estimates for the SPEAR data sets (section 4.6.2).

3.5 Hadronic Event Selection

In order to study pions, we must first select well measured hadronic events from the DST's. The major backgrounds common to all the four data sets are beam-gas, cosmic ray, and lepton pair production processes. Except for $\tau^+\tau^-$ production, these background events have characteristically low charged track multiplicity. In addition, the primary vertices of beam-gas or cosmic ray events are usually reconstructed far from the interaction point. $\tau^+\tau^-$ events consist of two to six charged

tracks in a two jet topology, where each jet has a low effective mass. A standard set of cuts has been developed over the course of the MARK II running to select well measured hadronic events with maximum efficiency while minimizing contamination from the above backgrounds. The following sequence of these cuts serves to define a hadronic event in this analysis.

1. A search is made for charged tracks which have well measured momenta and project close to the primary vertex. In order to be called a good charged track,
   a) the momentum of the track must satisfy $p \leq E_{cm}$, and the projection of the momentum in the plane perpendicular to the drift chamber axis (xy plane) must be $p_\perp \geq 0.1\ GeV/c$;
   b) the angle of the track with respect to the beam axis must be within the sensitive tracking volume of the drift chamber:

$$| \cos\theta | = | \frac{p_z}{p} | \leq 0.794;$$

   c) the minimum distance of approach of the track to the primary vertex must be $z \leq 5.0\ cm$ along the beam axis and

$$r_\perp \leq 1.0\ cm \quad \text{for} \quad p > 1\ GeV/c,$$

$$p\ r_\perp \leq 1.0\ cm\ GeV/c \quad \text{for} \quad p \leq 1\ GeV/c,$$

   radially in the xy plane. This cut removes most mismeasured tracks as well as a good fraction of the tracks from K^0 and Λ decays.
2. Neutral tracks are subjected to minimal quality cuts since they are only used in calculating event sphericity and total visible energy. A neutral track is used if
   a) the liquid argon shower energy is above 200 MeV;
   b) the closest approach of a drift chamber projected track to the neutral shower center is more than 7 cm.

3. With this set of good charged and neutral tracks, several cuts are made on the event as a whole. Note that in the case of the $\gamma\gamma$ data, the electron that tags the event by showering in the SAT system cannot be seen in the drift chamber and thus is not included in the list of charged tracks.
   a) The primary vertex of the event must be within 1.0 cm of the interaction point in the xy plane and within 5.0 cm in the direction along the z axis.
   b) The event must have three or more good charged tracks. This cut is chosen to retain maximum pion statistics. Contamination by simple QED events is handled by two additional cuts. First, an event is rejected if it has three or four good charged tracks and it contains at least one well identified[32] e or μ. Second, an event is rejected if it is determined to have two jets[33] each of which has an effective mass less than 2.5 GeV. The latter is intended to remove $\tau^+\tau^-$ pairs.

In the sample of e^+e^- annihilation events, we still need to remove the $\gamma\gamma$ interaction background. Because the final state e^+ and e^- in a $\gamma\gamma$ event typically stay close to the initial beam direction, only a fraction of the E_{cm} is available for the production of hadrons. The signature of the $\gamma\gamma$ interaction is therefore that the sum of energies of charged and neutral tracks in the event, called the total visible energy, is a relatively small fraction of E_{cm}. We require that the total visible energy in an e^+e^- event satisfy $E_{total} \geq 0.25\ E_{cm}$.

The visible energy in a γ event decreases as the final state e^+ and e^- get closer to the beam direction. The triggering of both SAT modules means that the e^+ and e^- radiated very low energy photons, which would have too little energy to annihilate into a lot of hadrons. We want populous hadronic events, so we require a single SAT tag in the $\gamma\gamma$ event sample.

Since the PEP $q\bar{q}$ and PEP $\gamma\gamma$ data sets come from the same pool of PEP data, it is important to check that the separate criteria used to assemble the e^+e^- and $\gamma\gamma$ event samples did indeed produce mutually exclusive sets of events. When

the analysis was run on the $\gamma\gamma$ DST's with the e^+e^- event requirements, only 1.5% of the $\gamma\gamma$ events passed the cuts. The total number of events passing the hadronic cuts is listed for each data set in Table 3.4.

Table 3.4 *Number of events surviving hadronic and analysis cuts, and the mean number of pions per event in events that pass analysis cuts.*

Data Set	Number of DST Events	Number of Hadronic Events	Number of Analysis Events	$\langle N_{\pi\pm} \rangle$ in Analysis Event
SPEAR J/ψ	1,285,000	477,000	308,000	3.6
SPEAR $q\bar{q}$	495,000	78,000	51,000	3.9
PEP $\gamma\gamma$	264,000	42,000	18,000	3.6
PEP $q\bar{q}$	182,000	54,000	52,000	5.2

3.6 Analysis Event Selection

Out of the sample of hadronic events we need to select those which have enough pions to make combinations of like charge and mixed charge pion pairs and triplets possible.

The pion sample is defined as all the ± 1 charged tracks in the event which are not well identified electrons, muons, kaons, or protons. Since pions constitute by far the largest fraction of produced charged particles, the odds are favorable that a particle is a pion when the other identifications are borderline. To handle the residual contamination of the pion sample, a correction for pion misidentification is later applied using a Monte Carlo calculation. This correction is discussed in detail in the next chapter. We use the following particle definitions:

1. A *well identified* electron is a particle with momentum $p \geq 1\ GeV/c$ which satisfies the standard MARK II requirements for an electron candidate discussed in section 3.2.3.
2. A *well identified* muon is a particle with momentum $p \geq 2\ GeV/c$ which satisfies the standard MARK II requirements for a muon candidate discussed in section 3.2.4.

3. A *well identified* kaon is a particle which satisfies
   a) $p \leq 1\ GeV/c$
   b) the TOF weight for a kaon, discussed in section 3.2.2, is $W_K \geq 0.35$
   c) the measured time of flight is within 4σ of the calculated time of flight for a kaon with momentum p.
4. A *well identified* proton is a particle which satisfies
   a) $p \leq 2\ GeV/c$
   b) the TOF weight for a proton, discussed in section 3.2.2, is $W_p \geq 0.35$
   c) the measured time of flight is within 4σ of the calculated time of flight for a proton with momentum p.

Table 3.5 shows the purity of the resulting pion sample, namely what fraction of the particles identified as pions are really pions. These numbers are derived by applying the pion selection criteria to Monte Carlo data, examining the Monte Carlo generated identities of the particles identified as pions, and calculating the fractional contamination by other particles. The Monte Carlo data sets listed in Table 3.5 are described in more detail in section 4.6.1.

Table 3.5 *The table below shows the results of a Monte Carlo study which calculated what fraction of particles identified as pions were really generated e, μ, K, and p.*

Monte Carlo Data Set	π	e	μ	K	p
MC SPEAR J/ψ	0.90	0.05	0.03	0.02	0.00
MC SPEAR $q\bar{q}$	0.90	0.04	0.03	0.02	0.01
MC PEP $\gamma\gamma$	0.90	0.04	0.03	0.02	0.01
MC PEP $q\bar{q}$	0.84	0.03	0.02	0.08	0.03

In order to eliminate the products of $\gamma \rightarrow e^+e^-$ which can be misidentified as an unlike charged pion pair, we apply a cut on the pair angle: $\cos\theta_{pair} \leq 0.997$. The same cut is applied to like charged pairs to preserve the phase space match

between the like and unlike pairs. About 70% of the conversion pairs misidentified as pion pairs are removed in this way, and the angle cut is small enough to fall well within the first bin of our Q^2 distributions. As we will see in chapter six, this cut does not measurably influence the fitted values of parameters α and r.

Finally, we must ensure that there are enough pions to make pairs and triplets. Events with two pions would overwhelmingly favor unlike charged pairs, which would distort the kinematic phase space match between the like and unlike pairs. For pair analysis, therefore, we require that at least three pions and both charges be present in an event. For similar reasons a minimum multiplicity of five pions and both charges are required for making triplets. Each pair, alone or in a triplet, is subject to a cut whose purpose is to remove photon conversion pairs. Namely, the opening angle between an unlike pair is required to be greater than five degrees, and a similar cut is made on like pairs in order to preserve the phase space match.

Table 3.4 gives the total number of events that survive the analysis cuts, and Table 3.6 shows the total number of pions, pairs, and triplets in each data set. The relative numbers of like and mixed charge combinations are the result of the combinatorics involved in forming pairs and triplets. Note also that not all events used to make pairs ($N_{\pi\pm} \geq 3$) can be used to make triplets ($N_{\pi\pm} \geq 5$).

Table 3.6 *Pion statistics in the four data sets.*

Data Set	$N_{\pi\pm}$	$N_{\pi\pm\pi\pm}$	$N_{\pi\pm\pi\mp}$	$N_{\pi\pm\pi\pm\pi\pm}$	$N_{\pi\pm\pi\pm\pi\mp}$
SPEAR J/ψ	911,000	484,000	813,000	55,000	436,000
SPEAR $q\bar{q}$	236,000	149,000	224,000	36,000	216,000
PEP $\gamma\gamma$	109,000	61,000	94,000	13,000	73,000
PEP $q\bar{q}$	281,000	278,000	323,000	341,000	1,375,000

Chapter 4. DATA ANALYSIS FOR PION PAIRS

4.1 INTRODUCTION

In the previous chapter we discussed the four data sets, event selection, and the identification of pions. This chapter deals with data analysis, namely the steps leading to the observation and measurement of the Bose-Einstein enhancement in a given set of pion pairs. The analogous steps for triplets are discussed in the next chapter.

Why use pions? A study of the GGLP effect requires large statistics, and pions are the most abundantly produced bosons in e^+e^- collisions. The MARK II π^0 reconstruction is too poor to permit a measurement of the effect in $\pi^0\pi^0$ pairs. We therefore confine the investigation to like charged pions.

Other groups have seen the Bose-Einstein enhancement in like charged kaons[4] and the analogous Fermi-Dirac depletion in like charged protons[5]. We are unable to make comparable measurements for lack of kaon statistics.

4.2 STUDY SAMPLE

We expect to see the GGLP effect in like charged pions, which we will also call the *study sample* from here on, because in the limit of similar momenta they become identical bosons; they are subject to Bose-Einstein statistics and are expected to exhibit the Bose-Einstein correlation. The study sample contains other correlations as well. In order to look for evidence of the Bose-Einstein enhancement we must first consider competing effects.

All particles produced in hadronic processes are subject to correlations from two general sources: conservation laws and dynamics. These can be further subdivided as follows.

1. Conservation Laws:

a) Conservation of energy-momentum leads to strong correlations when particles are produced near a kinematical boundary.

b) Conservation of quantum numbers and internal symmetries, such as isospin and parity, imposes constraints on the identity and number of particles produced.

2. Dynamics:

a) The particle production mechanism, such as production of resonances, can lead to correlations. Some of the hadronization models discussed in chapter one predict production related correlations.

b) Final state interactions between the newly formed particles can also introduce correlations in observed particle distributions. It is difficult to make a rigorous separation between production and final state dynamics since the strong force is the dominant interaction during and immediately after production. Once the particles are out of its range, however, the Coulomb interaction becomes dominant for charged particles.

Let us examine how each of these effects is manifested in the study sample.

Energy-momentum is conserved in the event as a whole, but the charged pions constitute only a part of the hadronic event. Other particles, detected and undetected, carry a significant fraction of the event energy and momentum. This "leftover" part of the event provides a buffer against the kinematical boundary for the charged pions. Figure 4.1 shows the distribution of the fraction of E_{cm} carried by charged pions in the study sample. In each of the four data sets, the distribution is close to symmetric and peaked about a value well below one, and the number of events goes smoothly to zero as the charged pion energy sum goes to E_{cm}. Thus the set of charged pions within an event is well away from the kinematical boundary in nearly all the analysis events. Similarly, the "leftover" part of the event acts as a reservoir of quantum numbers, allowing the smooth distribution of π^+ and π^- multiplicities shown in Table 4.1. Although conservation laws do not impose

constraints directly on the charged pions, energy-momentum considerations and pion multiplicities together determine the kinematical phase space distribution of the study sample.

Final state dynamics turn out to be relatively unimportant compared to the Bose-Einstein enhancement. The Coulomb interaction between produced pions can be calculated[34], and strong force final state interactions have recently been estimated for pions in Ref. 35. Sections 4.5.2 and 4.5.3 contain a discussion of these effects.

Assuming we understand the effects of kinematical phase space and final state interactions, measuring a less than maximum Bose-Einstein enhancement could be interpreted several ways.

To start with the most mundane explanation, we consider detector performance. The two track resolution of the drift chamber is important because it determines the minimum momentum difference, and therefore the maximum length, that we can resolve with the pion interferometer. If the pion source is bigger than this maximum, we will not be able to "see" it. In addition, if like charged pairs with a small pair angle are resolved less efficiently than unlike charged pairs with the same pair angle, then in the ratio of like to unlike pairs we will measure a Bose-Einstein enhancement lower than its true value. Finally any particles which were misidentified as pions will not be subject to Bose-Einstein statistics and will contaminate the true $\pi^{\pm}\pi^{\pm}$ pairs with an uncorrelated background. These effects and the performance of the MARK II are discussed in detail in section 4.6.

Many of the charged pions in the study sample are the decay products of resonances, which are produced abundantly in hadronic e^+e^- processes. The resonances are either short lived or long lived relative to the time it takes to traverse the size of the primary source. If a pion from a long lived resonance is paired with a pion from the primary source, that pair will give a measure of the resonance decay length rather than the dimension of the primary source. Depending on the number of resonances produced, a significant fraction of the pion pairs will measure various decay lengths and will mix together in the total sample to give some complicated

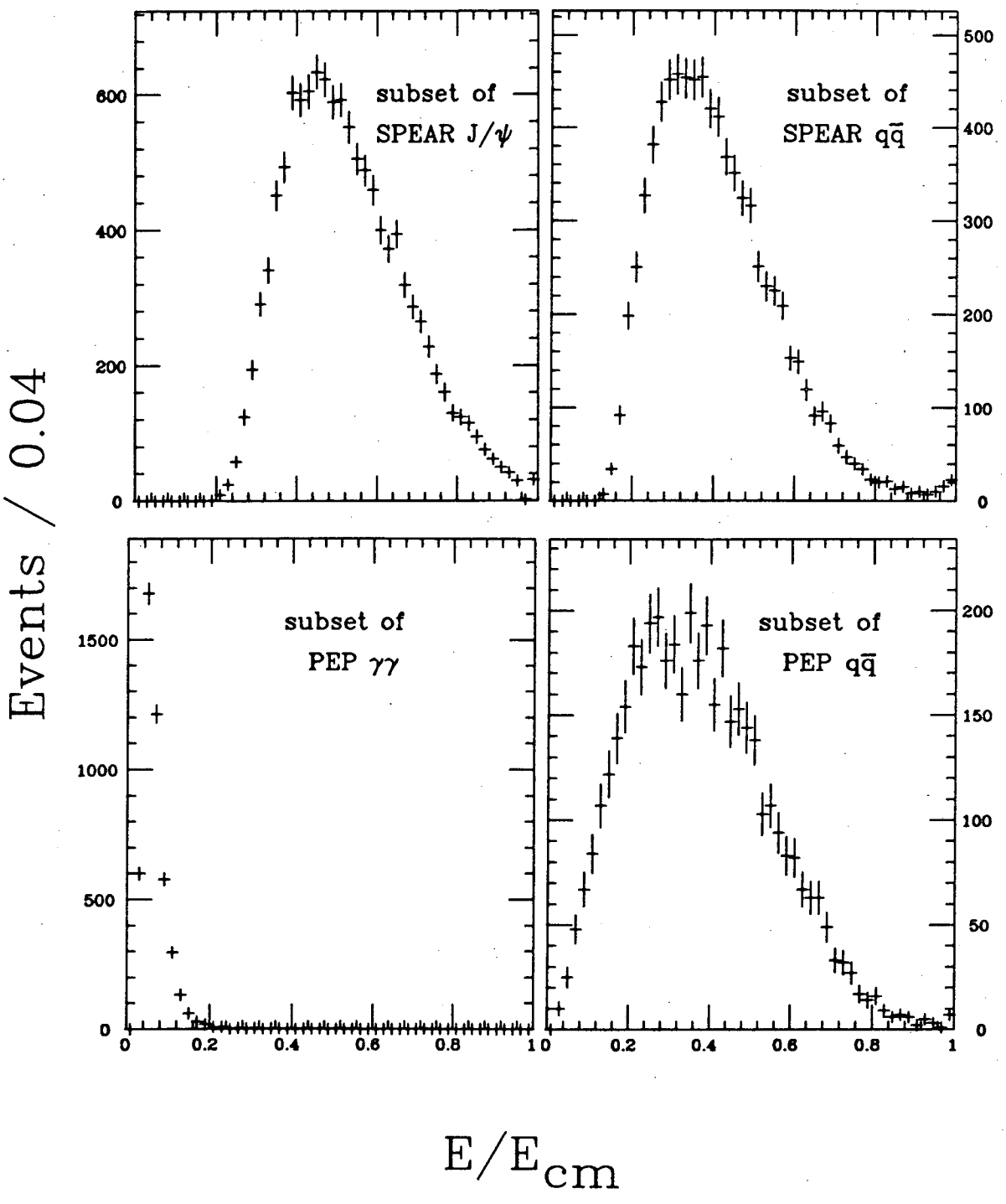

Figure 4.1 *Distributions of the fraction of E_{cm} carried by charged pions in the analysis event.*

Table 4.1 *Distributions of π^+ and π^- multiplicities within an event for the four data sets. The entries are percentages of analysis events with the given $(N_{\pi+}, N_{\pi-})$ multiplicity.*

	$N_{\pi+}$	% events with $(N_{\pi+}, N_{\pi-})$							
$N_{\pi-}$		1	2	3	4	5	6	7	8
SPEAR J/ψ	1		27	4	< 1				
	2	27	22	5	< 1				
	3	4	5	2	< 1				
	4	< 1	< 1	< 1	< 1				
SPEAR $q\bar{q}$	1		19	6	< 1				
	2	20	21	8	1				
	3	6	8	4	< 1				
	4	< 1	1	< 1	< 1				
PEP $\gamma\gamma$	1		22	6	< 1				
	2	22	22	6	1				
	3	6	6	3	< 1				
	4	< 1	1	< 1	< 1				
PEP $q\bar{q}$	1		3	1	< 1	< 1			
	2	3	5	5	3	1	< 1		
	3	1	5	7	5	3	1	< 1	
	4	1	3	5	5	4	2	< 1	
	5	< 1	1	3	4	4	3	1	< 1
	6		< 1	1	2	2	2	1	< 1
	7			< 1	1	1	1	1	< 1
	8				< 1	< 1	< 1	< 1	< 1

average of all the lengths. In appendix B we discuss further the effect of resonances on the Bose-Einstein enhancement.

If detector performance and the effect of resonances are accounted for, and the corrected Bose-Einstein enhancement is still less than maximum, then we turn to the remaining unknown. As we saw in chapter one, a less than maximum Bose-Einstein enhancement can also be interpreted as evidence of partial coherence in the hadronization process.

Figure 4.2 shows the distribution of the like charged pairs in Q^2. Over most of Q^2, the shape of the distribution reflects pion pair phase space. The GGLP effect leads us to expect an excess of pairs over the prediction of phase space alone in the region of small Q^2. We use a "reference sample" to try to measure this excess.

4.3 Reference Sample

The central problem in the analysis of the GGLP effect is to separate the Bose-Einstein enhancement from other correlations in the study sample. To do this we introduce the *reference sample*, which is a representation of the study sample in the absence of Bose-Einstein statistics. The *ideal* reference sample

a) contains all of the correlations that exist in the study sample except the Bose-Einstein correlation and
b) is free of correlations which are absent from the study sample.

Unfortunately, the ideal reference sample for our study sample does not exist in nature. All the reference samples that have been used or proposed thus far fail to satisfy one or both of the requirements for the ideal reference sample. This section describes the advantages and disadvantages of several commonly used reference samples and introduces one new candidate.

4.3.1 Unlike Charged Pion Pairs

If the study sample consists of like charged pion pairs, then at first glance unlike charged pion pairs are the natural choice for the reference sample. $\pi^+\pi^-$ pairs have the same kinematical phase space as $\pi^\pm\pi^\pm$ pairs, and since π^+ and π^- are different particles the Bose-Einstein enhancement is absent.

There are some complications, however.

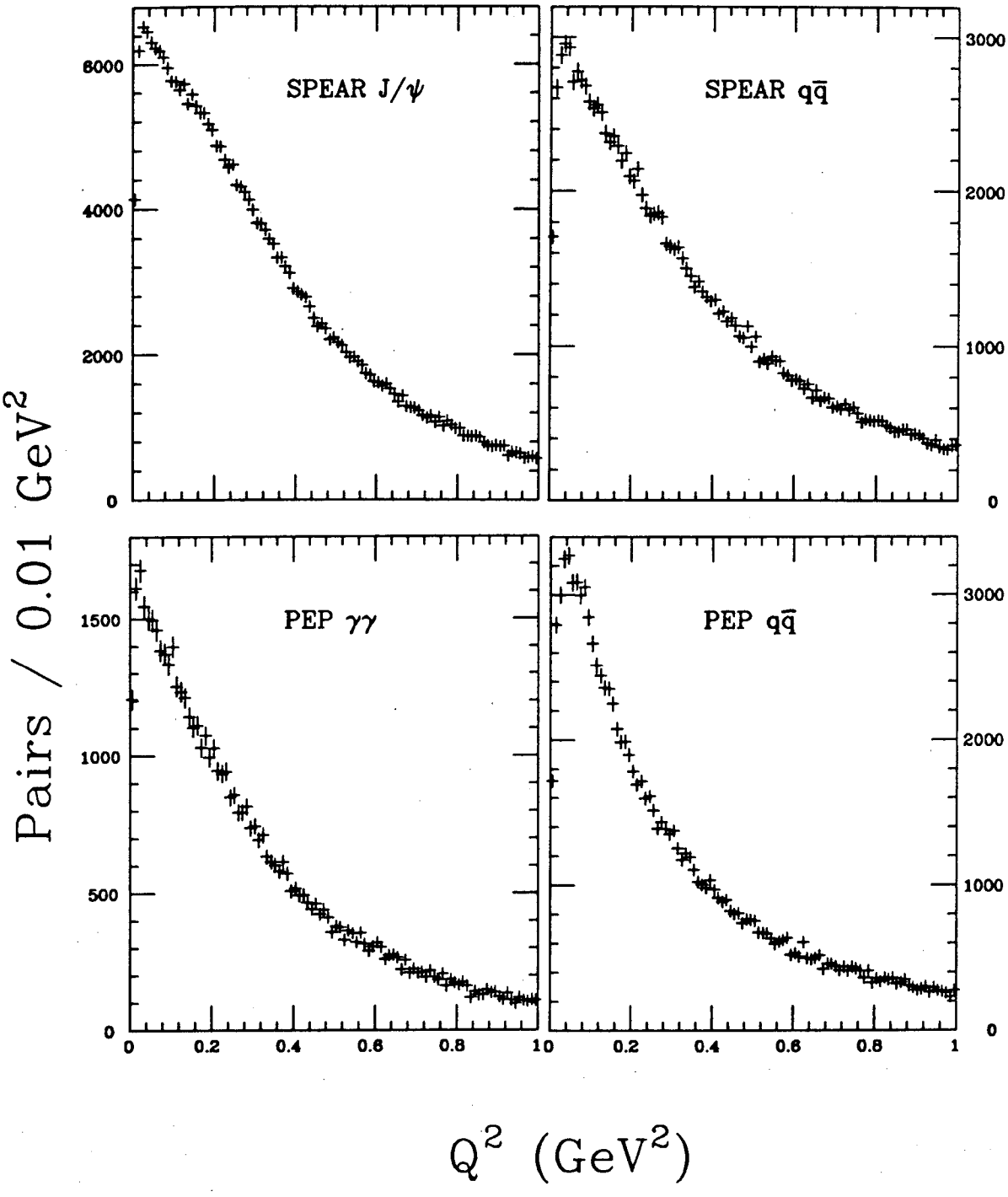

Figure 4.2 *Distributions of like charged pairs in Q^2 for the four data sets.*

As we saw in the preceding section, decay products of resonances make up a large fraction of the charged pions. Many $\pi^+\pi^-$ pairs reconstruct to all or part of a resonance, distorting the kinematic phase space of the unlike pairs in the region of the resonance mass. Problems could arise if a resonance distorts the unlike pair phase space so much that the latter cannot be used to "divide out" the like pair phase space in the region of the Bose-Einstein enhancement. Figure 4.3 shows the distribution of the unlike charged pairs in Q^2. Keeping in mind that Q^2 is equal to the effective mass of the pair to within an additive constant, it is easy to find the K^0 and ρ^0 signals at $Q^2 \approx 0.19\ GeV^2$ and $Q^2 \approx 0.4-0.6\ GeV^2$, respectively. There is no clear evidence for other resonances in the range of Q^2 shown. If we normalize the number of like pairs to the number of unlike pairs, and we superimpose the Q^2 distributions of like and unlike pairs as in Fig. 4.4, then we can see the agreement in the phase space envelopes of the two samples, the Bose-Einstein enhancement in the region of small Q^2 in the like charged pairs, and the resonance signals in the unlike charged pairs. These features can also be seen in Fig. 4.5, which shows the result of subtracting the normalized unlike pair distribution from the like pair distribution. Normalization was done by rescaling the total number of unlike pairs in the region of $0.0\ GeV^2 \leq Q^2 \leq 1.0\ GeV^2$ to the total number of like pairs in the same region.

Another kind of phase space distortion is evident in the PEP $q\bar{q}$ data set: the ratio R of like to unlike charged pairs rises slowly with Q^2. This long range correlation is the result of charge and energy conservation and is most evident in events containing jets[36]. Although it does not distort R locally in the Bose-Einstein enhancement region of Q^2, the long range correlation affects the overall fit to R. Corrections for resonances in the unlike charged pairs and for long range correlations in Q^2 are discussed further in section 4.5.1.

Complications also arise from final state interactions. The Coulomb attraction between unlike pairs is opposite to the repulsion in like pairs. Thus the Coulomb force creates a net suppression in the ratio of like to unlike charged pairs, and the suppression gets stronger as the pair effective masses get smaller. Similarly, the

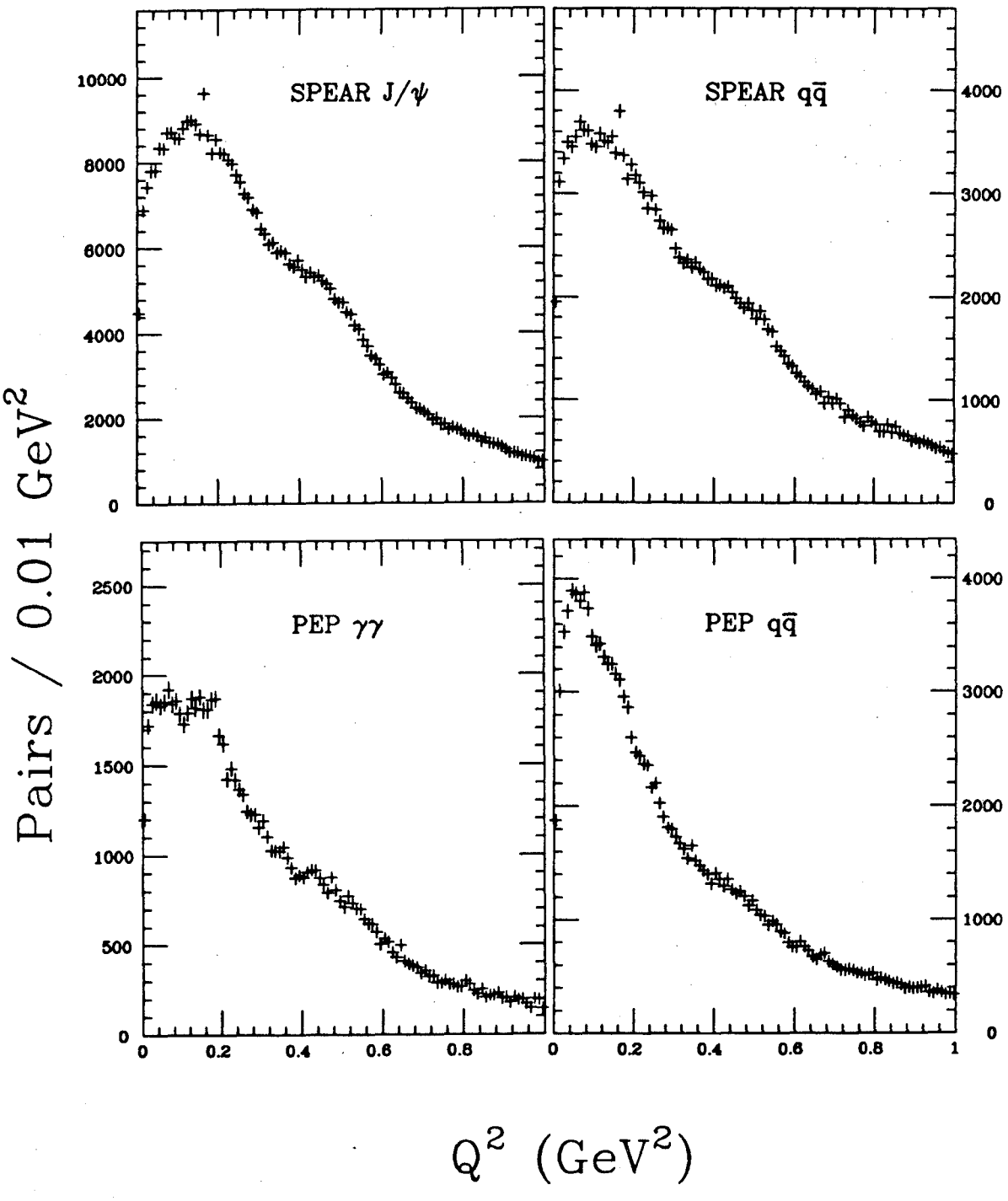

Figure 4.3 *Distributions of unlike charged pairs in Q^2 for the four data sets.*

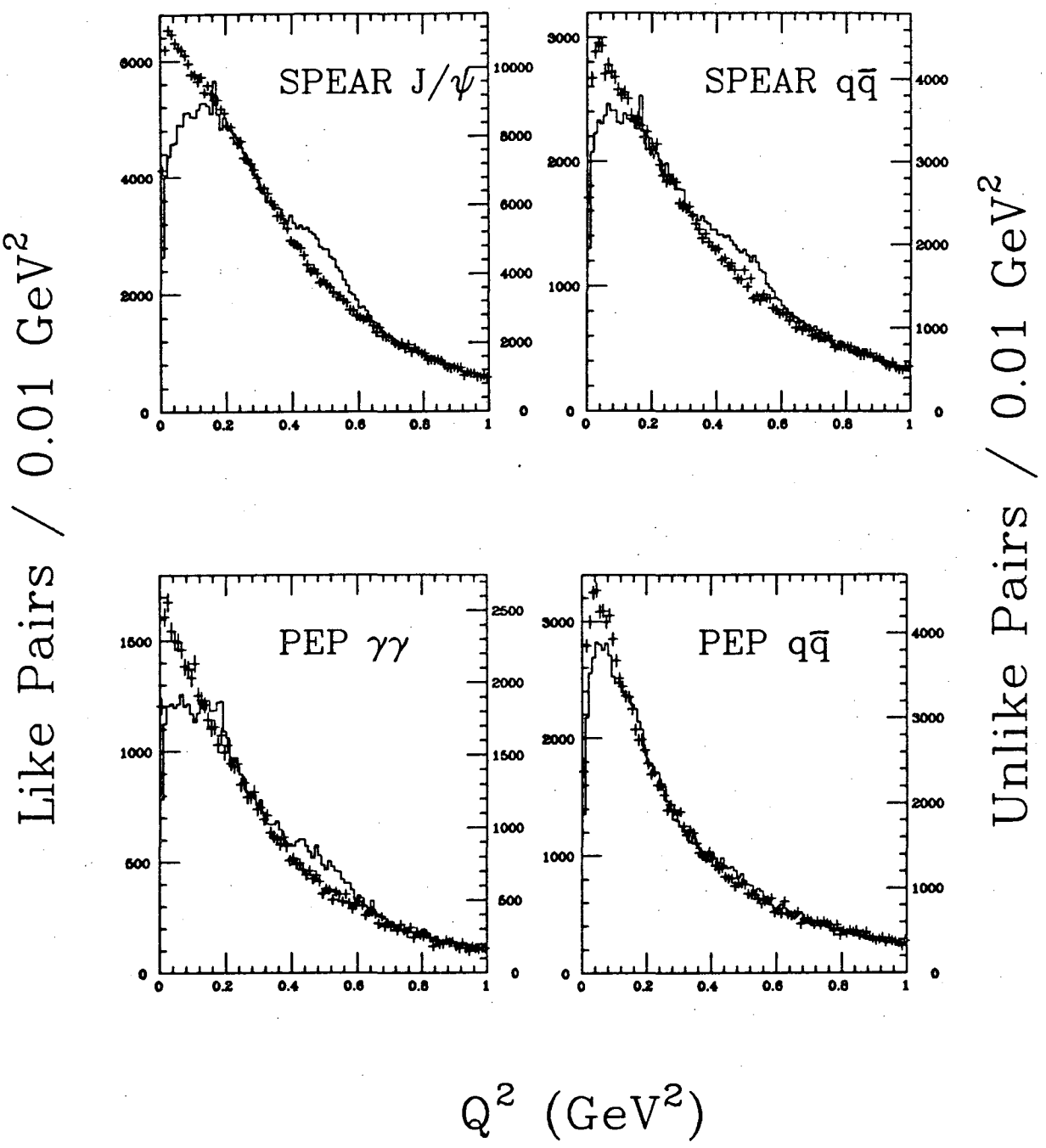

Figure 4.4 *Figure 4.2 and Fig. 4.3 normalised and superimposed, showing the phase space agreement of the like (points) and unlike (histogram) charged pairs. The two distributions are normalised to each other by rescaling the vertical axis of the unlike pair distribution so that the like and unlike distributions overlap each other in the region of* $0.68\ GeV^2 < Q^2 < 1.00\ GeV^2$. *Note the excess of like charged pairs (Bose-Einstein enhancement) in the region of small* Q^2 *and the* K^0 *and* ρ^0 *resonance signals in the unlike charged pairs.*

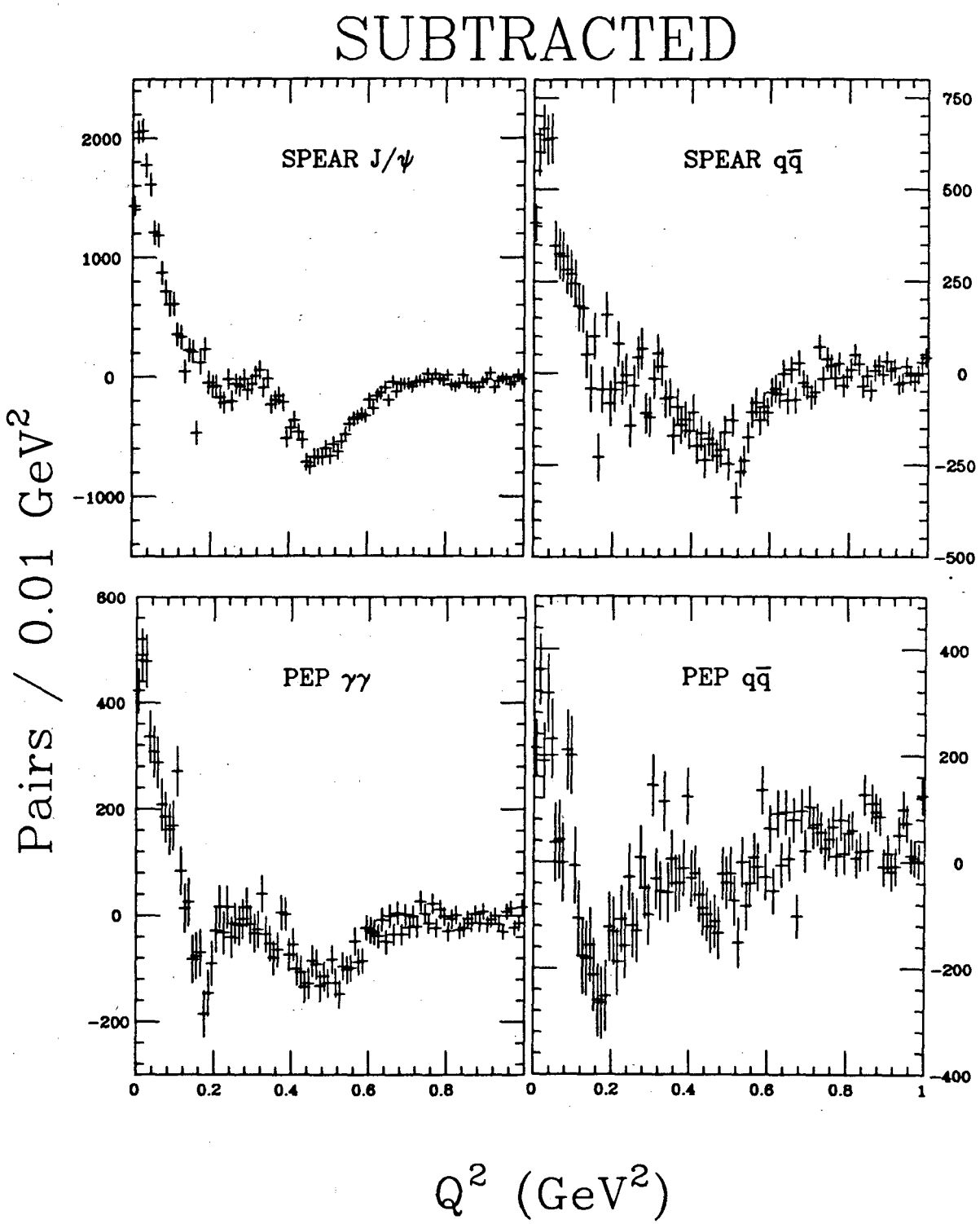

Figure 4.5 *The same features evident in Fig. 4.4 can be seen in this figure, which shows the result of subtracting the normalized unlike pair distribution from the like pair distribution. Normalization was done by rescaling the total number of unlike pairs in the region of* $0.0\ GeV^2 \leq Q^2 \leq 1.0\ GeV^2$ *to the total number of like pairs in the same region.*

strong force final state interaction deduced from $\pi\pi$ phase shift[35]. may create a net suppression in the ratio at small pair masses. In sections 4.5.2 and 4.5.3 we discuss these effects in more detail.

Finally, *residual correlations* arise because we use the same pions to make the reference sample pairs as we do to make the study sample pairs. This effect is more pronounced in nuclear collision experiments, where the reference sample is often constructed directly from the set of like charged pions[37]. In the case of our study sample, we have seen how the Bose-Einstein correlation distorts like pair phase space near small Q^2. This is reflected in the distribution of individual π^+'s and π^-'s in an event. They in turn determine the phase space of the unlike pairs in the event, resulting in a residual correlation. In appendix A we discuss how an iterative procedure can be used to estimate the magnitude of this effect. Typically first order corrections are small enough to be neglected[36].

The unlike charged pair reference sample was the first to be proposed[3] and has since been used extensively in GGLP analyses, often as a double check on alternate reference samples. It reproduces the study sample kinematical phase space well, and its complications do not seriously interfere with the measurement of the Bose-Einstein enhancement. For these reasons we use it as the standard reference sample against which all other candidate samples are tested.

4.3.2 Alternate Reference Samples

In some GGLP experiments it may not be possible to use unlike charged pairs as a reference sample. For example, the detector may be set up to detect only one sign of pion charge[12]. Experiments like these have pioneered the search for alternate reference samples.

After our experience with the unlike charged pairs, we see that a reference sample need not be ideal in order to be useful. We loosen the requirements and define a *good* reference sample as one which

a) reproduces the kinematical phase space of the study sample and

b) does not contain correlations which interfere with the measurement of the GGLP effect.

The relatively small final state effects are simply neglected.

We refer to unlike charged pairs as a *natural* reference sample because the pions have not been manipulated in any way. An *artificial* reference sample can be made by taking the detected data and randomizing some aspect of the events or the charged pions. In the following sections we discuss artificial reference samples based on event mixing and introduce the mixing algorithm that is used on triplets in chapter five.

4.3.3 Introduction to Mixing Events

Although many of the general comments about event mixing apply equally well to pairs and triplets, we will postpone a discussion of triplets until the next chapter and will refer only to pairs here. A *mixed event* reference sample consists of pairs created by combining pions from one event with pions from another event. Obviously, these pairs are not dynamically constrained and do not have to obey conservation laws, so they are free of the corresponding correlations. The event mixing process in effect constructs a hybrid event which is a superposition of two real events.

4.3.4 Mixing Events: Cluster Mixing Algorithm

The four data sets are geometrically distinct. A typical SPEAR J/ψ event is nearly spherical. The SPEAR $q\bar{q}$ continuum above the ψ consists of less spherical events, as $e^+e^- \rightarrow q\bar{q}$ begins the transition to distinguishable jets. Particles produced in a PEP $\gamma\gamma$ event are often bunched together to balance the momentum carried off by the missing e^+ or e^-. Finally, the PEP $q\bar{q}$ data is in an energy regime where two-jet events are typical and events with three jets are fairly common.

These geometries are evident in Table 4.2, which shows for each data set the fraction of events with a given number of particle clusters. Cluster finding is done the same way for all the data sets: all the good charged tracks and neutral

tracks in an event are fed into a utility cluster finding routine LCLUS, which is part of the Lund Monte Carlo package. LCLUS uses particle momenta to find groups of particles clustered together in jet-like structures, labels the groups in order of decreasing cluster momentum, returns the energy-momentum of each cluster, and assigns the input particles to clusters. In this way we can reduce the geometry of all four data sets to a common denominator, the cluster.

Table 4.2 *Fraction of events with the given number of clusters.*

	Number of Clusters in Event				
Data Set	one	two	three	four	five or more
SPEAR J/ψ	1.00	.0	.0	.0	.0
SPEAR $q\bar{q}$	0.99	0.01	.0	.0	.0
PEP $\gamma\gamma$	0.95	0.05	<0.01	.0	.0
PEP $q\bar{q}$	0.02	0.69	0.26	0.03	<0.01

Before describing the *cluster mixing algorithm*, we need to make some preliminary remarks. Each cluster, as it is found by the utility routine, consists of three sets of detected tracks: π^+'s, π^-'s, and non-charged-pions (NCP).

In order to combine pions from different events, we must have a storing mechanism. The event being analyzed is called the current event, while events analyzed before the current event are referred to as previous events. For example, in the case of whole event mixing, we store the momenta of all the charged pions from a previous event, and we pair all the charged pions in the current event with all the stored pions. For the cluster mixing algorithm, we store "one third" of each cluster from a previous event: namely, from each cluster we store all the pions of one charge. For simplicity, we will use the term *stored pions* to refer to this set of π^+'s or π^-'s taken from a cluster of a previous event.

The stored pions are sorted by two variables. The first is their multiplicity. We use clusters which have no more than ten pions of any one charge. Table 4.3.

shows that the π^+ and π^- multiplicity distributions within a cluster are well within these limits for all four data sets. The second variable is the order number of the cluster from which the stored pions were taken. Recall that the cluster finding routine labels the clusters in order of decreasing momentum. Thus the kinematics of a fourth cluster can be quite different from those of a first cluster. Keeping track of both of these variables is necessary in order to produce a hybrid event which is geometrically equivalent to a real event.

We make the following definitions for use in the cluster mixing algorithm:

a) $\vec{p}_+$ is the vector sum of the three-momenta of the π^+'s in the cluster;
b) $\vec{p}_-$ is the vector sum of the three-momenta of the π^-'s in the cluster;
c) $\vec{p}_c$ is the three-momentum of the cluster;
d) $\vec{p}_o \equiv \vec{p}_c - \vec{p}_+ - \vec{p}_-$.

Note that $\vec{p}_o$ is the net three-momentum of all the NCP ("other") tracks in the cluster.

With these comments and definitions in mind, we can now describe the cluster mixing algorithm and its hybrid event. For each cluster in the event

1. select a set of stored pions which
   a) has a multiplicity equal to the average of the π^+ and π^- multiplicities in the cluster, and
   b) was taken from a cluster of the same order number as the cluster being analyzed;
2. find the vector sum $\vec{p}_c$ of the three-momenta of these stored pions;
3. find a three-dimensional rotation U which takes the $\hat{p}_s$ direction into the $\hat{p}_o$ direction. This rotation is not unique. We define U to be the rotation by θ about the axis $\hat{r}$, where

$$\cos\theta = \hat{p}_o \cdot \hat{p}_s,$$

$$\hat{r} = \hat{p}_o \times \hat{p}_s,$$

$$\hat{p}_o = U\hat{p}_s.$$

Table 4.3 *Distributions of π^+ and π^- multiplicities within a cluster for the four data sets. The entries are percentages of clusters with the given $(N_{\pi+}, N_{\pi-})$ multiplicity.*

	$N_{\pi+}$	% clusters with $(N_{\pi+}, N_{\pi-})$				
$N_{\pi-}$		1	2	3	4	5
SPEAR J/ψ	1		27	4	< 1	
	2	27	22	5	< 1	
	3	4	5	2	< 1	
	4	< 1	< 1	< 1	< 1	
SPEAR $q\bar{q}$	1		19	6	< 1	
	2	20	21	8	1	
	3	6	8	4	< 1	
	4	< 1	1	< 1	< 1	
PEP $\gamma\gamma$	1		22	6	< 1	
	2	22	22	6	< 1	
	3	6	6	3	< 1	
	4	< 1	< 1	< 1	< 1	
PEP $q\bar{q}$	1		16	6	2	< 1
	2	16	15	8	2	< 1
	3	6	8	5	2	< 1
	4	2	2	2	1	< 1
	5	< 1	< 1	< 1	< 1	< 1

4. Apply U to all the three-momenta of the stored pions, and call these the rotated stored pions. In a sense, the effect of U is to allign the set of stored pions with the set of NCP tracks in the cluster using the net three-momenta vectors as a guide.
5. Now treat the rotated stored pions, π^{mix}, just like the π^+'s and π^-'s in

the cluster. Make pairs by combining a $\pi^{\pm}$ with a π^{mix}. Make triplets by combining a π^{+}, a π^{-}, and a π^{mix}.

In Table 4.4 we show the total number of pairs and triplets made using the mixed cluster algorithm. Figure 4.6 shows how well the cluster mixing reference sample reproduces the kinematical phase space of the unlike charged pairs. The main advantage of using the mixed cluster reference sample in pair analysis is that it is free of resonances such as the K^0 and the ρ^0, that are evident in the unlike pairs. This is helpful in fitting the ratio of like to reference pairs. Using mixed cluster pairs, the fit can include regions of Q^2 which must be avoided because of resonances when using unlike pairs. The results of fits with both reference samples are presented in chapter six.

Table 4.4 *The total number of pairs and triplets made using the mixed cluster algorithm.*

Data Set	$N_{\pi^{\pm}\pi mix}$	$N_{\pi^{\pm}\pi^{\mp}\pi mix}$
SPEAR J/ψ	1,201,000	783,000
SPEAR $q\bar{q}$	549,000	372,000
PEP $\gamma\gamma$	236,000	136,000
PEP $q\bar{q}$	742,000	1,863,000

4.4 Monte Carlo Sample

With the two requirements for a good reference sample in mind, Monte Carlo data seems like an excellent candidate for an alternate reference sample. However, the mechanics of current event generators introduce some difficulties.

Monte Carlo event generators are adjusted to reproduce detected data by way of a given set of built-in parameters. Typically, these parameters affect only single particle production, which is reflected in distributions of particle momenta, fraction of particles containing strange, charmed and bottom quarks, particle multiplicity,

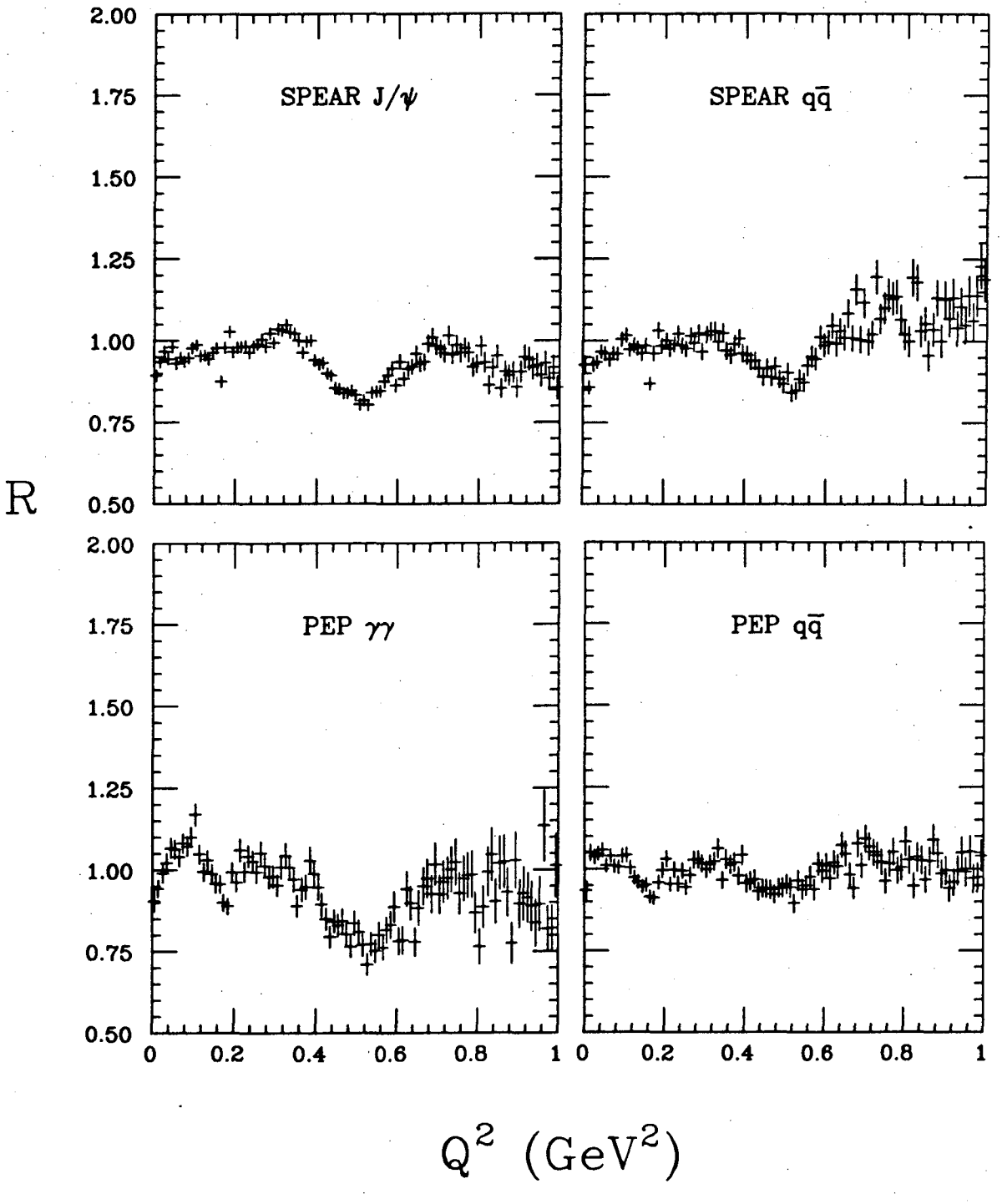

Figure 4.6 *Ratio of Q^2 distributions of two reference samples in experimental data (not Monte Carlo). The numerator is the pair reference sample created by the cluster mixing algorithm. The denominator is the reference sample of unlike charged pairs.*

and event sphericity and thrust, among others. Distributions involving two or more particles, such as the Q^2 distribution for pion pairs and the analogous distribution for pion triplets, cannot be adjusted directly to reproduce detected data. They are only affected indirectly by changes in the single particle distributions.

Since pair distributions are not adjusted in the event generator, it is more difficult to tune the kinematic phase space of Monte Carlo pairs to the one of detected pairs. Therefore we have not used a Monte Carlo generated data set as a reference sample. However, we expect that the ratio of like to unlike pairs R_{mc} in the Monte Carlo behaves the same way as the ratio R in detected data, since kinematic phase space cancels out in the ratio. Our Monte Carlo data set, MC PEP $q\bar{q}$, correctly models both the resonances and the long range energy correlations in the PEP $q\bar{q}$ data set. In section 4.5.1 we describe how the ratio R/R_{mc} is used to correct for these effects in the PEP $q\bar{q}$ data set, and in section 4.6.2 R_{mc} is used to investigate the tracking performance of the MARK II drift chamber.

4.5 Corrections: Due to Nature of Study and Reference Samples

When we described the study and reference samples, we noted that several mechanisms can result in an observed Bose-Einstein enhancement that is less than maximum. In this section we discuss the mechanisms which are inherent in our particular study and reference samples, while the next section covers mechanisms which arise from detector performance.

4.5.1 Resonances and Long Range Correlations

The two effects we discuss in this section influence the ratio R of like to unlike pairs in the region of Q^2 away from the Bose-Einstein enhancement. Although they do not distort the Bose-Einstein enhancement itself, they affect the overall fit to R.

We saw in section 4.3.1 that the unlike charged pairs show no evidence of resonances in the region of $Q^2 < 0.15\ GeV^2$. In the fit to R (section 4.7), we exclude only the regions of Q^2 near K^0 and ρ^0. This works well in SPEAR data, where the K^0 is narrow and just on the edge of the Bose-Einstein enhancement region.

However, in PEP data the K^0 is much wider and may overlap the Bose-Einstein enhancement region significantly enough to affect the fit. Figure 4.7 shows the ratio R of like to unlike charged pion pairs in the PEP $q\bar{q}$ data set, the K^0 and ρ^0 resonances, and the slow rise in R as a function of Q^2. The rise in R is due to a combination of long range correlations[38] which are the result of charge and energy conservation laws.

The MC PEP $q\bar{q}$ data set introduced in chapter three has been tuned to reproduce the resonances and jet structure present in PEP $q\bar{q}$ data. Forming the ratio R_{mc} of like to unlike charged pion pairs in the Monte Carlo, we see in Fig. 4.8 the same resonances and long range correlations observed in the PEP $q\bar{q}$ data. Dividing R by R_{mc}, as in Fig. 4.9, we remove the effects of resonances in the reference sample and of the long range correlations in Q^2. As noted in section 4.6.2, R/R_{mc} also divides out any asymmetry in the detection of like versus unlike charged pairs.

The influence of the K^0 and the ρ^0 on the fit to R is checked in all data sets by comparing the fit using the unlike pair reference sample to the fit using the mixed cluster reference sample.

Long range correlations in Q^2 are present in all four data sets. We take into account this slow variation with Q^2 by fitting the ratio R to the expression

$$R = (1 + \delta\ Q^2)\ (1 + \alpha\ e^{-r^2Q^2}),$$

where δ is a measure of the overall slope of R. As we will see in chapter six, in the region $0.0\ GeV^2 < Q^2 < 1.0\ GeV^2$ over which we fit R, δ is close to zero for all data sets except the PEP $q\bar{q}$ data.

4.5.2 Final State Strong Interaction Effects

The hadronization process is governed by the strong interaction, which continues to act between the pions immediately after production until they get far enough away from each other to be out of its range. No analytic solution exists which describes how the pion wavefunctions are modified by this interaction.

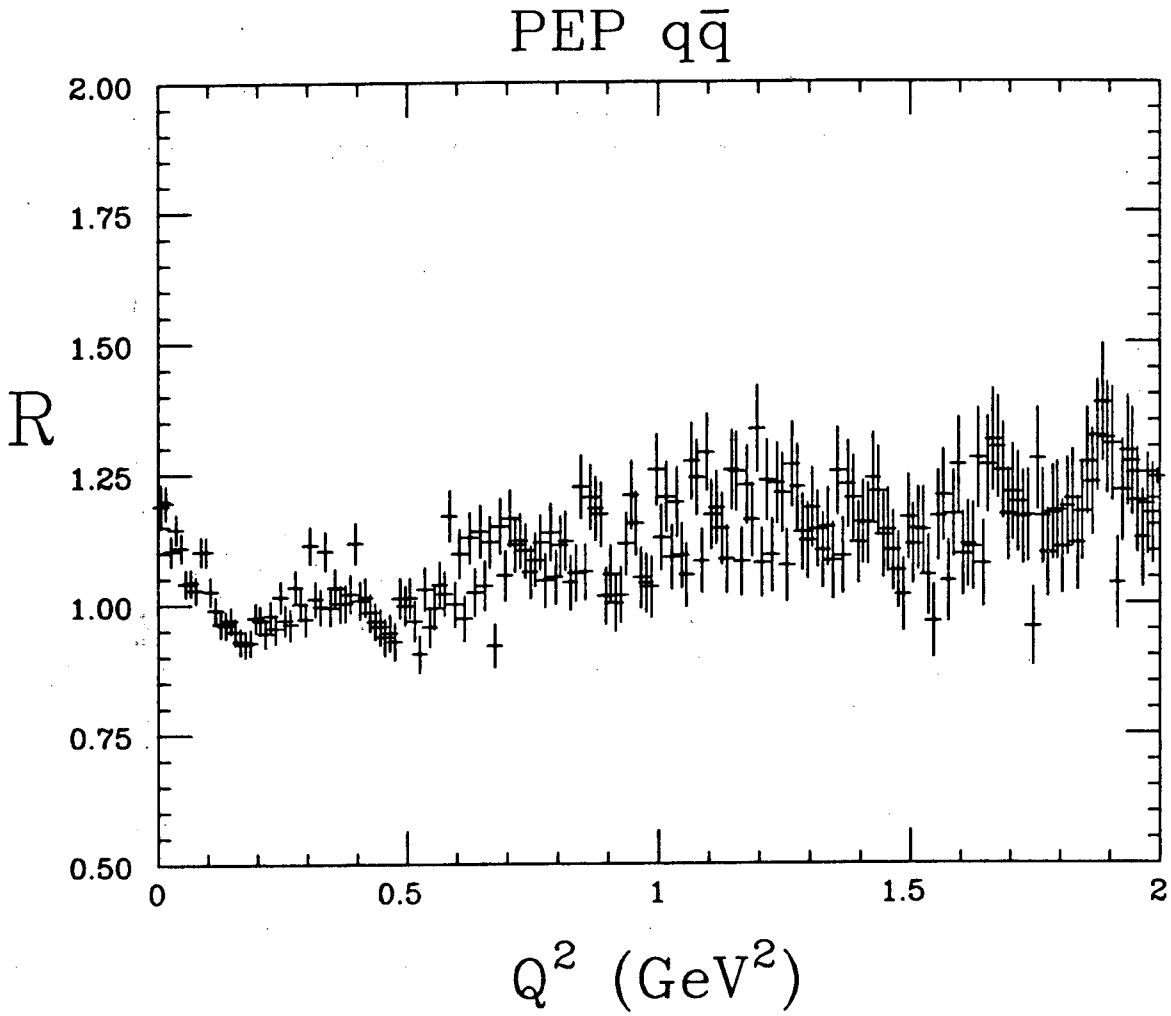

Figure 4.7 *Ratio of like to unlike charged pairs in the PEP $q\bar{q}$ data showing the Bose-Einstein enhancement at small Q^2, the K^0 and ρ^0 resonances, and the slow rise with Q^2 ascribed to long range correlations.*

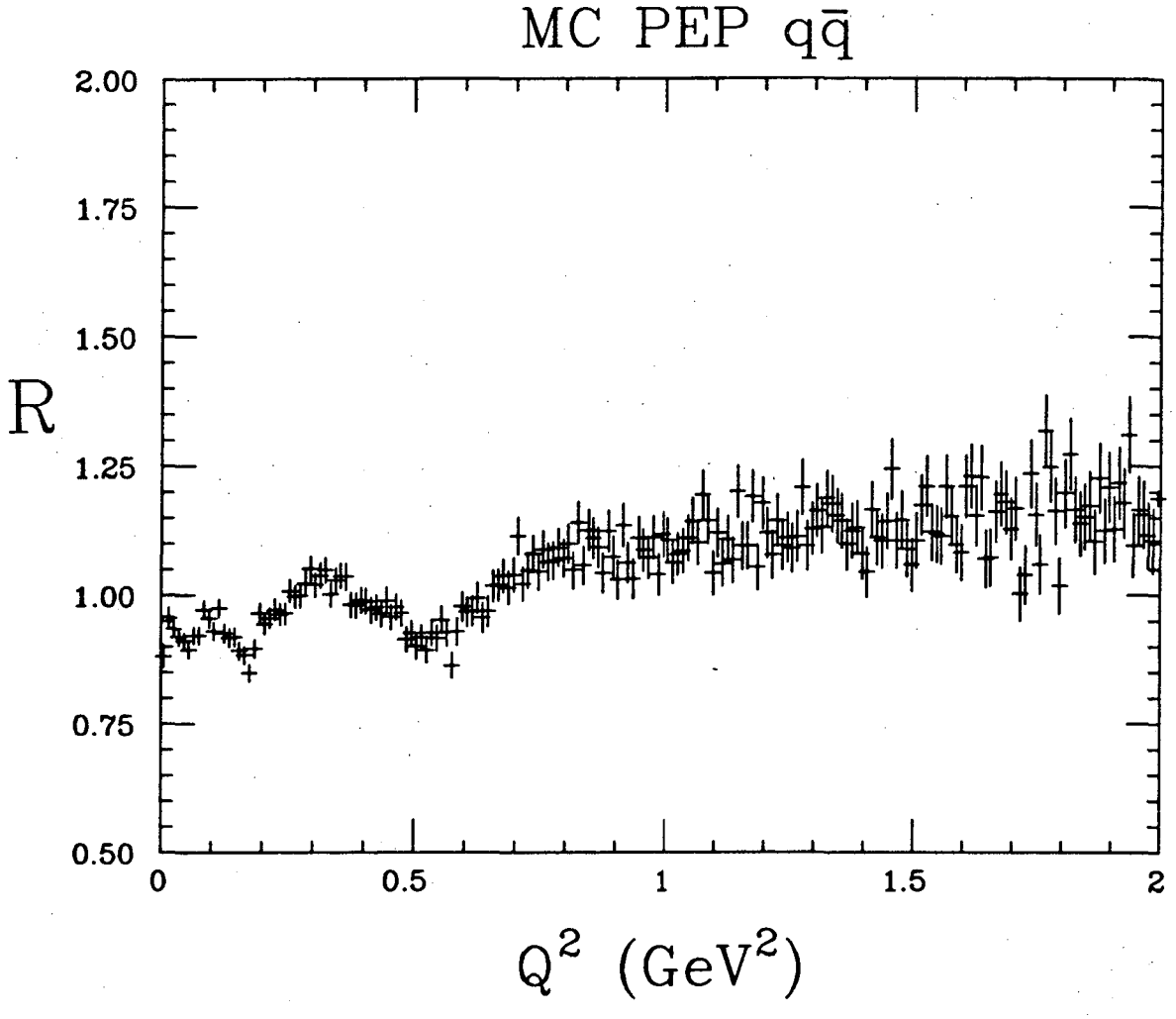

Figure 4.8 *Ratio R_{mc} of like to unlike charged pion pairs in the Monte Carlo showing the resonances and long range correlations which are also present in the PEP $q\bar{q}$ data set.*

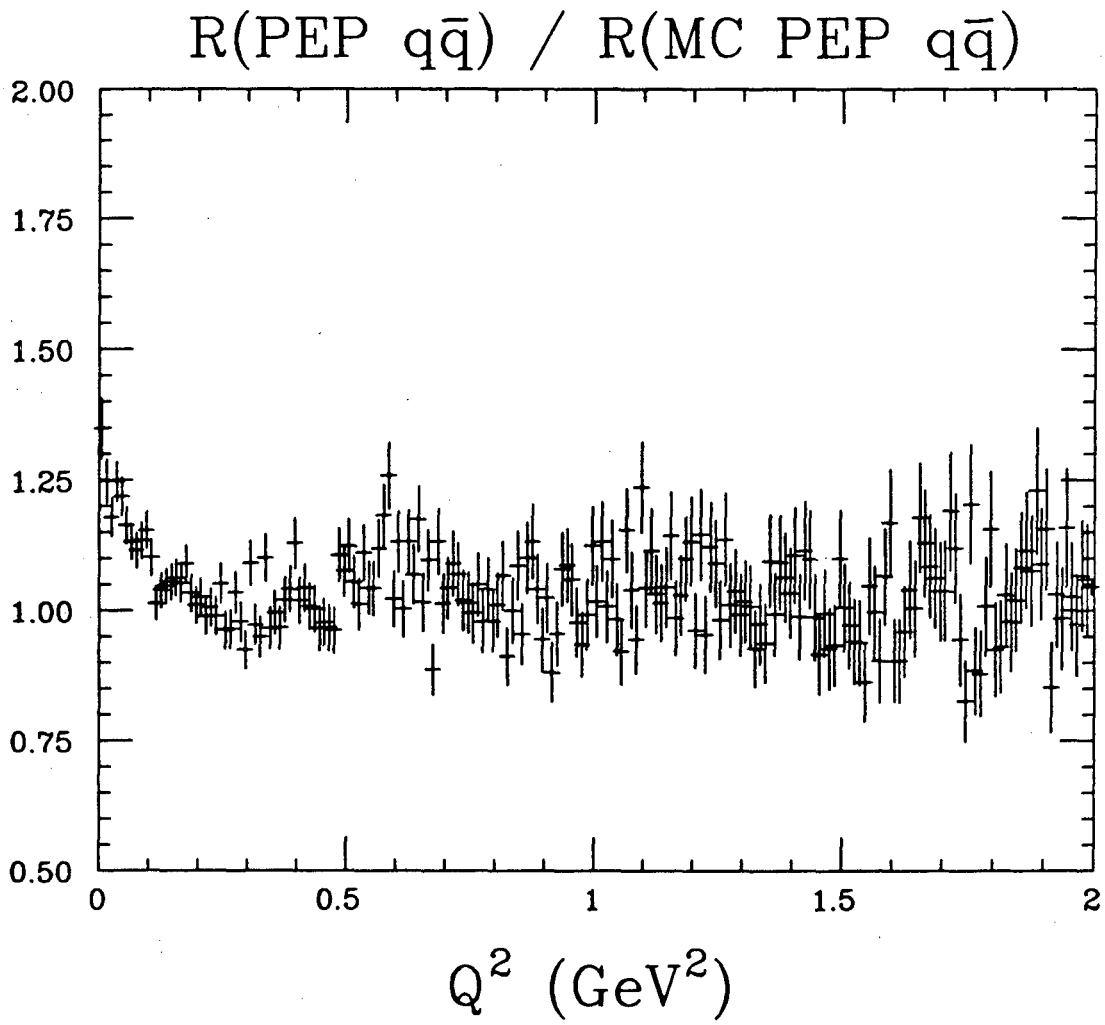

Figure 4.9 *Ratio of R for the PEP $q\bar{q}$ data set divided by R_{mc} for the Monte Carlo data. Note that there is no evidence of resonances or long range correlations in Q^2 in this ratio R/R_{mc}.*

However, an estimate has been made recently by Suzuki[35] of the effect of the final state strong interaction on the observed Bose-Einstein enhancement. In e^+e^- collisions, the Bose-Einstein enhancement is confined to the region of $Q^2 < 0.2\ GeV^2$. Making the assumption that p-wave $\pi^+\pi^0$ scattering can be neglected and s-wave scattering is dominant in this region of Q^2, and using the measured values of the s-wave scattering phase shifts in the channel of isospin 2, he estimates that the observed Bose-Einstein enhancement is suppressed $20^{+5}_{-13}\%$ by the presence of the strong interaction. The errors are calculated from the uncertainties in the parameterization of the energy dependence of the phase shifts. Suzuki also points out that the separation between production dynamics and final state strong interactions is ambiguous, and improvement of the estimate above will require a better understanding of the production process.

This calculation indicates that an uncorrected measurement underestimates the true Bose-Einstein enhancement. Since the estimate of the effect of the strong interaction in the data is less precise than the corrections for the Coulomb interaction and for pion misidentification, we do not attempt to correct systematically for the effects of the final state strong interaction as we do for the latter two.

4.5.3 Final State Coulomb Force Effects

Once produced pions are out of the range of the final state strong force, the dominant interaction is Coulomb repulsion or attraction. In heavy ion collision experiments, a produced pion is affected by the Coulomb potentials of both the other produced pions and the nuclear fragments in an event. In e^+e^- collisions, the charge of the remaining hadrons is relatively small. Therefore we expect that we can neglect the Coulomb interaction between a pion and the remaining hadrons compared to the Coulomb force between the two pions in a pair.

Two like charged pions experience Coulomb repulsion, depopulating like pair phase space at small relative momenta. The standard derivation of the correction factor for this effect for like charged pairs can be found in the work of Gyulassy and Kauffmann[34]. The like charged pion pair inclusive distribution in the presence of

the pair Coulomb interaction is given by

$$P_l(k_1,k_2) = G_l(\eta)P_n(k_1,k_2),$$

where $P_n(k_1,k_2)$ is the like pair inclusive distribution in the absence of the Coulomb final state interaction, and

$$G_l(\eta) = \frac{2\pi\eta}{\exp(2\pi\eta)-1}, \quad \eta = \frac{\alpha m_\pi}{\mid k_1 - k_2 \mid}.$$

Here, $\alpha = 1/137$, and k_1 and k_2 are pion four-momenta in the pair center of mass frame, so that

$$\eta = \frac{\alpha m_\pi}{\sqrt{Q^2}}.$$

$G_l(\eta)$ is the modulus square of the nonrelativistic Coulomb wavefunction at the origin, also known as the Gamow factor for like charged pairs. The correction is small except for small Q^2, as shown in Fig. 4.10.

Two unlike charged pions experience Coulomb attraction, producing extra unlike pairs in the phase space region of small relative momenta. The correction factor for this effect follows from the generalized Gamow factor derived by Davydov[39] (section 100, p.403):

$$G(\xi) = \frac{2\pi|\xi|}{|\exp(2\pi\xi)-1|},$$

where

$$\xi = \begin{cases} \alpha m_\pi/\sqrt{Q^2} = \eta, & \text{for repulsive forces;} \\ -\alpha m_\pi/\sqrt{Q^2} = -\eta, & \text{for attractive forces.} \end{cases}$$

The unlike charged pion pair inclusive distribution in the presence of the pair Coulomb interaction is then given by

$$P_u(k_1,k_2) = G_u(\eta)P_n(k_1,k_2),$$

where $P_n(k_1,k_2)$ is the like pair inclusive distribution in the absence of the Coulomb final state interaction, and

$$G_u(\eta) = \frac{2\pi\eta}{1-\exp(-2\pi\eta)}.$$

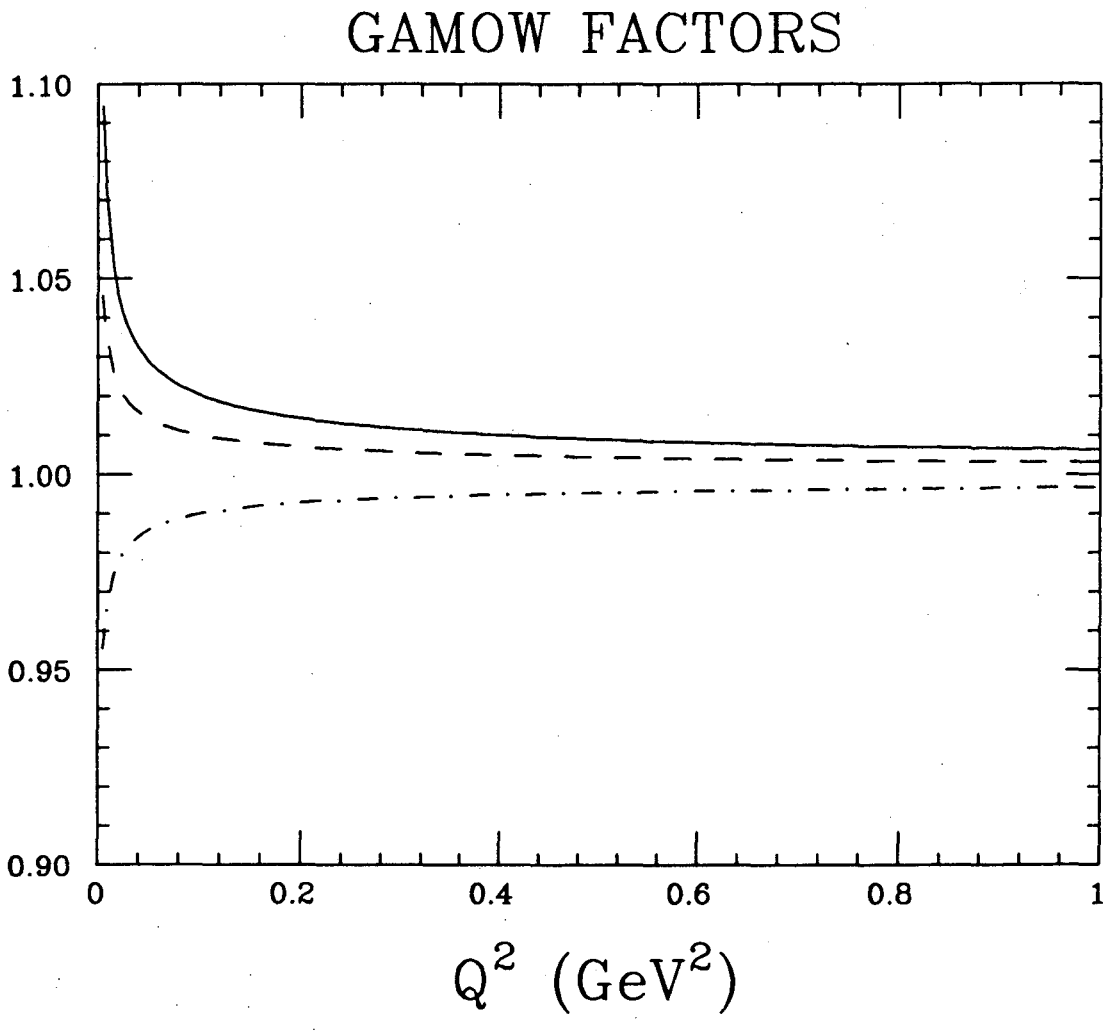

Figure 4.10 *The Gamow factors $G_l(\eta)$ (dot-dash line) and $G_u(\eta)$ (dashed line). In order to get the ratio R of like to unlike charged pairs in the absence of the Coulomb final state interaction, we in effect multiply the observed R by the factor G_u/G_l (solid line).*

$G_u(\eta)$ is shown in Fig. 4.10.

The correction for Coulomb effects is done by weighting each like pair by $1/G_l(\eta)$ and each unlike pair by $1/G_u(\eta)$. The ratio of the corrected like to corrected unlike pairs then represents R in the absence of the Coulomb interaction. There is no Coulomb interaction between the pions in a mixed cluster pair, because they are taken from different events. Thus when we form the ratio of like to mixed cluster pairs, we correct only for the Coulomb repulsion in the like pairs.

4.6 Corrections: Due to Detector Performance

In this section we discuss how non-ideal detector performance can result in the observation of a less than maximum Bose-Einstein enhancement.

4.6.1 Pion Misidentification

Recall that pions are defined as those particles which remain after all well identified electrons, muons, kaons, and protons are removed. In the Monte Carlo section of the last chapter we noted that the performance of detector components used in particle identification did not change significantly in the move from SPEAR to PEP. Hence we can use the MC PEP $q\bar{q}$ data set to measure the fraction of misidentified pions in all the data sets.

Pion misidentification is a function of momentum, so to get the correct fraction of misidentified pions in a data sample, the Monte Carlo data sample must have the same pion momentum distribution as the detected data. Figure 4.11 shows the pion momentum distributions (data points) in the four data sets. The MC PEP $q\bar{q}$ data reproduces the PEP $q\bar{q}$ data momentum distribution. In order to mimic the momentum distributions of the other data sets, we start with the MC PEP $q\bar{q}$ momentum distribution and "filter" it into the momentum distribution of the required shape. The filtering process involves first dividing the pion momentum distribution from the desired data set by the one from the PEP $q\bar{q}$ data set. Then event by event, the momenta of the pions in the MC PEP $q\bar{q}$ data set are kept or discarded by a random dice roll weighted by this ratio. Figure 4.11 shows the pion

momentum distributions (histogram) generated from the MC PEP $q\bar{q}$ data set in this way. The resulting data sets are called MC SPEAR J/ψ, MC SPEAR $q\bar{q}$, and MC PEP $\gamma\gamma$, and are used in this section to investigate the fraction of misidentified pions and pion pairs. In chapter five, we use the same Monte Carlo data sets to calculate the fraction of misidentified pion triplets.

Close inspection of Fig. 4.11 reveals a kink in the distribution at $p = 1\ GeV/c$. This is the result of the pion identification algorithm. Recall that we use TOF to separate pions from kaons below 1 GeV/c, but that above 1 GeV/c we do not attempt to identify and remove kaons. Thus above 1 GeV/c, kaon contamination of the pion sample jumps slightly and causes the observed discontinuity in the distribution of pion momenta. It turns out that this kink is small enough to be unimportant in the analysis that follows.

The fraction of Monte Carlo generated, or "true" pions π_t in the set of all particles identified as pions π is a function of momentum, as shown in Fig. 4.12. The fraction of correctly identified pions translates into a lower fraction of correctly identified pion pairs and a lower still fraction of correctly identified pion triplets. This is illustrated for like charged and unlike charged pairs in Fig. 4.13 and Fig. 4.14, respectively. These figures show the fraction of $\pi_t\pi_t$ in the set of all $\pi\pi$ as a function of Q^2.

We can see that the fraction of correctly identified pairs is not a strong function of Q^2 or of the charge of the pair. Therefore we average over these variables and use the average values, listed in Table 4.5, to correct each like charged pair distribution in Q^2.

Like charged pairs which are not $\pi_t\pi_t$ pairs exhibit no Bose-Einstein enhancement, so we use the reference sample as a model for their distribution in Q^2. Since Monte Carlo does not model the Coulomb interaction between its produced pions, the corrections listed in Table 4.5 must be applied to data distributions only after the latter have been corrected for the Coulomb interaction, if necessary. Thus the like and unlike pair distributions used in the pion misidentification correction below are distributions which have been corrected for Coulomb effects. The mixed

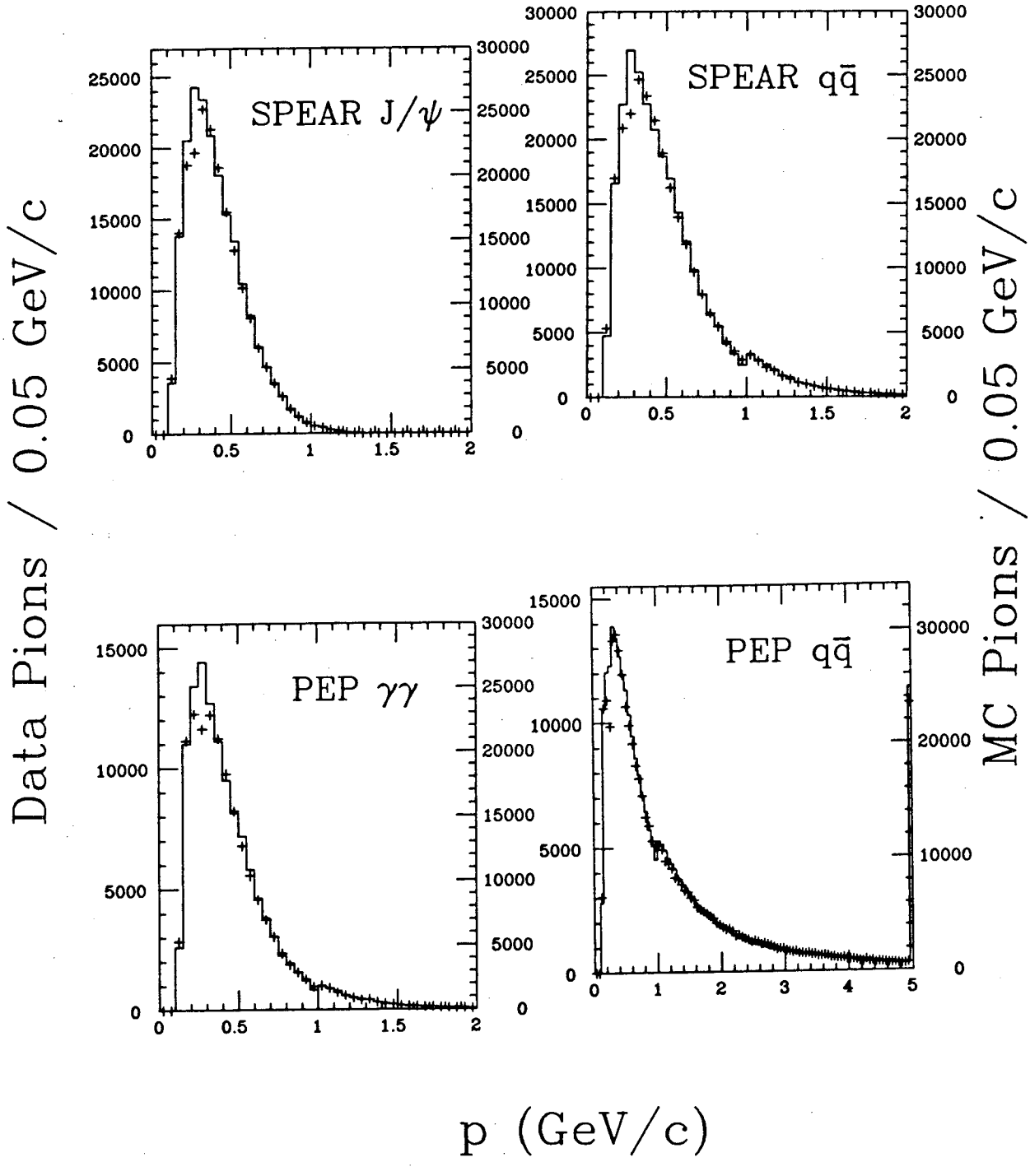

Figure 4.11 *Pion momentum distributions (data points) in the four data sets and the momentum distributions (histogram) produced by the filtering process applied to the MC PEP $q\bar{q}$ data set. The filtering process and the kink in the distributions at 1 GeV/c are discussed in the text.*

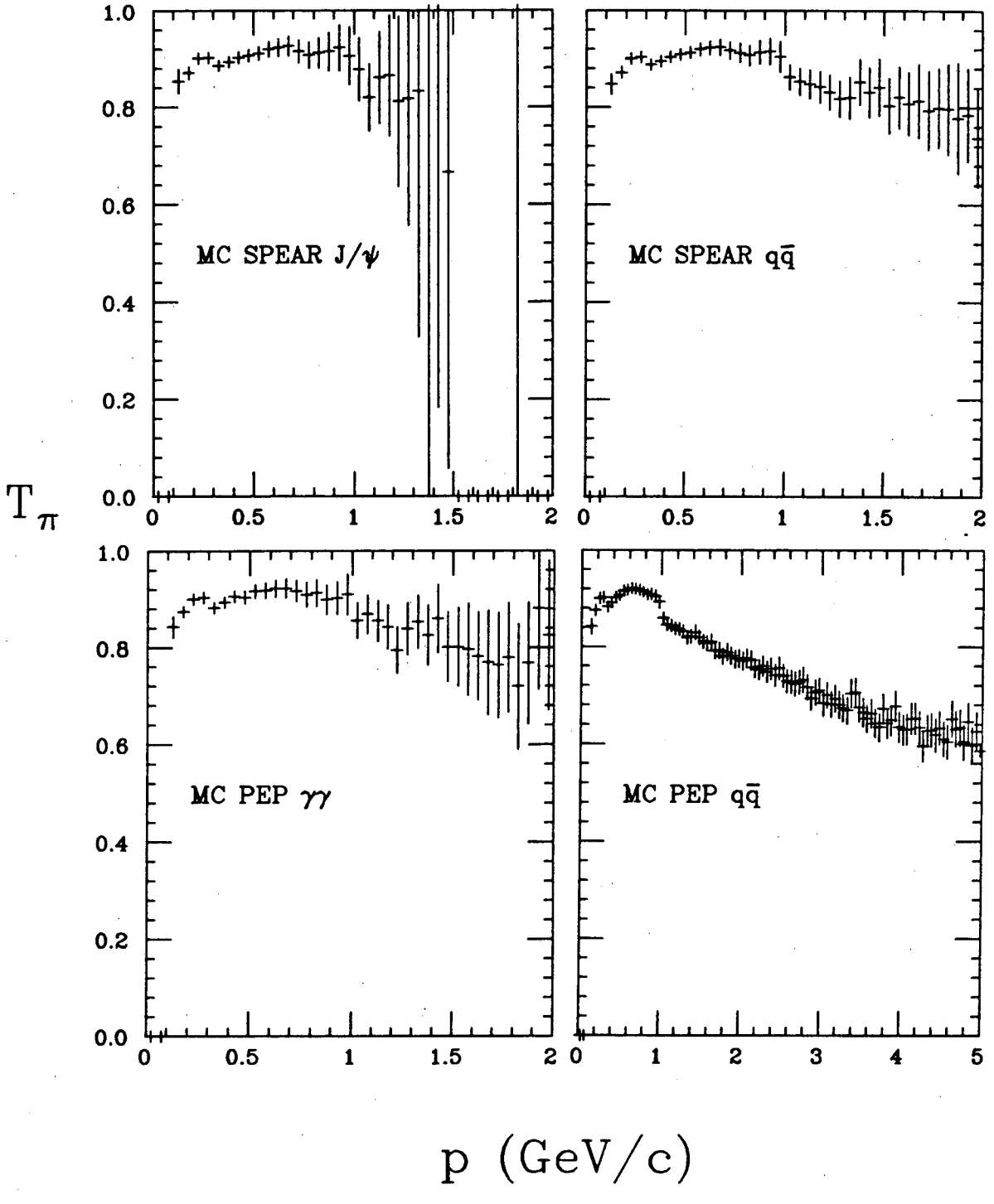

Figure 4.12 *A study done with Monte Carlo data showing the fraction T_π of correctly identified pions π_t in the set of all particles identified as pions π. The fraction is a function of pion three-momentum.*

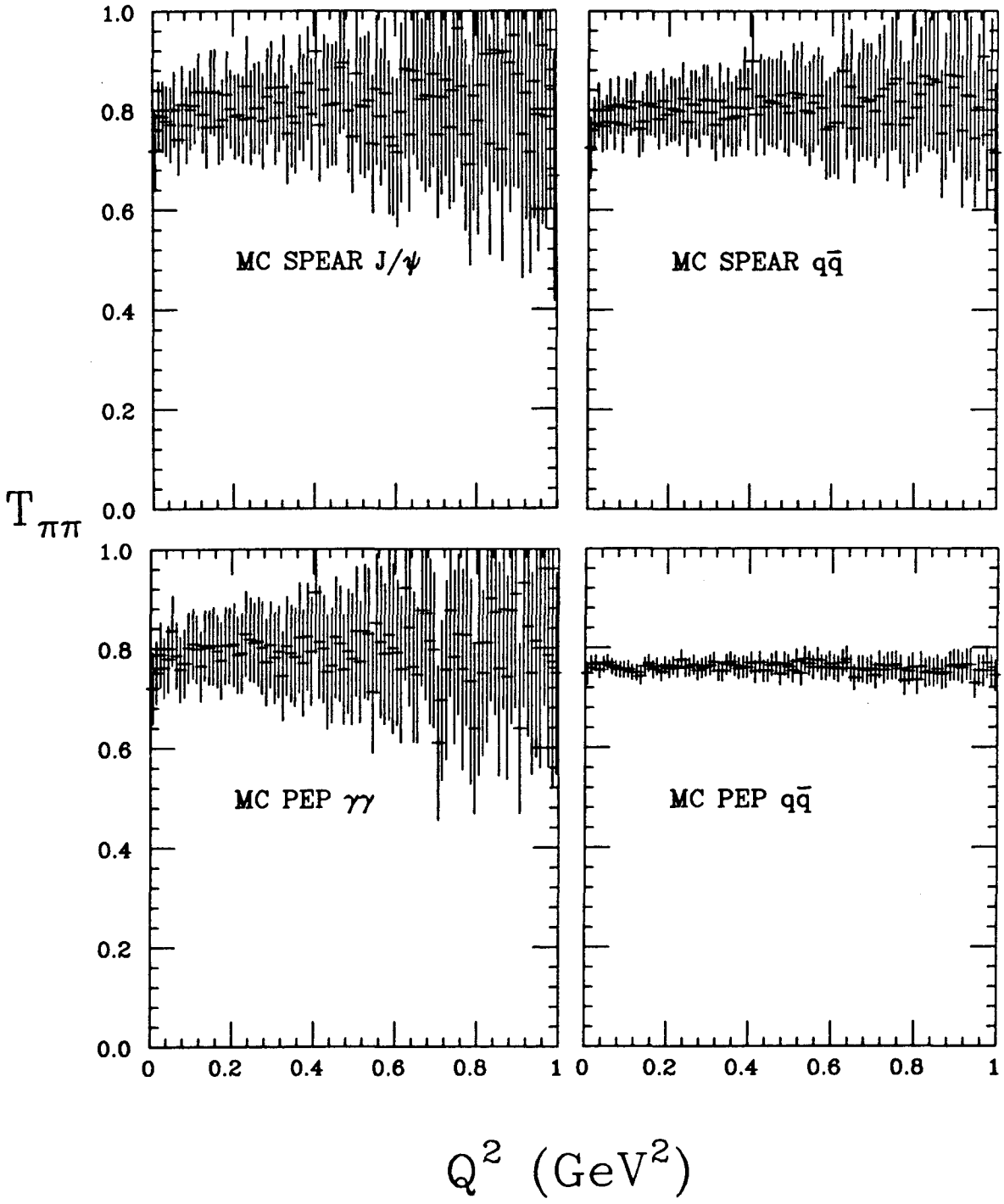

Figure 4.13 *A study done with Monte Carlo data showing the fraction $T_{\pi\pi}$ of like charged pairs of correctly identified pions $\pi_t\pi_t$ in the set of like charged pairs of particles identified as pions $\pi\pi$. The fraction is shown as a function of Q^2.*

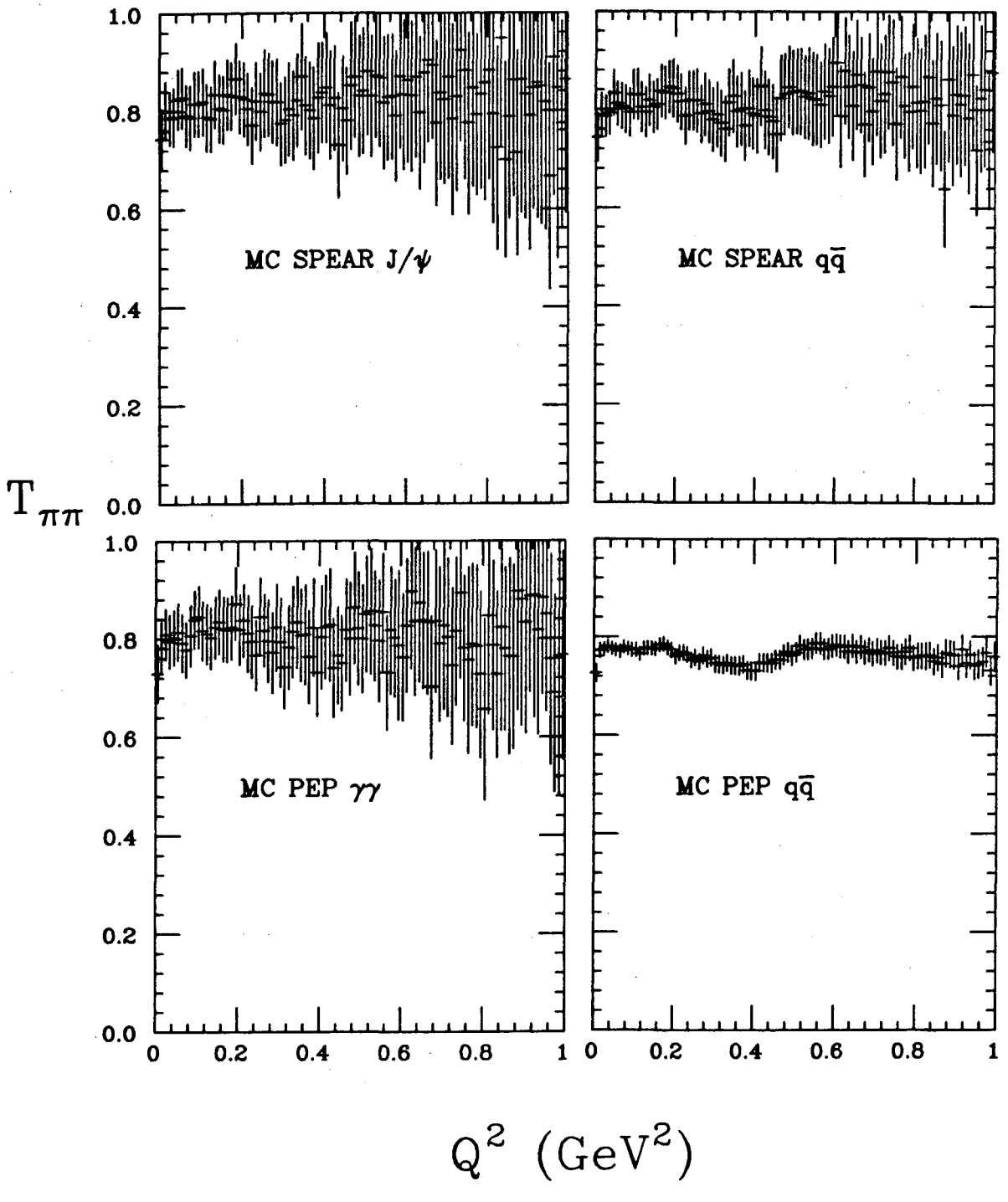

Figure 4.14 *A study done with Monte Carlo data showing the fraction $T_{\pi\pi}$ of unlike charged pairs of correctly identified pions $\pi_t\pi_t$ in the set of unlike charged pairs of particles identified as pions $\pi\pi$. The fraction is shown as a function of Q^2.*

Table 4.5 *The fractions plotted in Fig. 4.12, Fig. 4.13, and Fig. 4.14 are averaged over the charge combination and over the variable (three-momentum and Q^2, respectively), and the average values are listed here.*

Monte Carlo Data Set	$T_\pi \equiv \left\langle \frac{\pi_t}{\pi} \right\rangle$	$T_{\pi\pi} \equiv \left\langle \frac{\pi_t \pi_t}{\pi\pi} \right\rangle$
MC SPEAR J/ψ	0.90	0.81
MC SPEAR $q\bar{q}$	0.90	0.81
MC PEP $\gamma\gamma$	0.89	0.80
MC PEP $q\bar{q}$	0.84	0.72

cluster reference pairs require no Coulomb correction.

The pion misidentification correction (PMC) is done bin by bin on the like pair Q^2 distributions as follows:

$$B_{like}^{corr} = B_{like} - \frac{n_{like}}{n_{ref}} B_{ref}(1 - T_{\pi\pi}),$$

where

- B_{like}^{corr} is the content of the bin in the PMC-corrected like pair Q^2 distribution;
- B_{like} is the content of the bin in the PMC-uncorrected like pair Q^2 distribution;
- B_{ref} is the content of the bin in the (PMC-uncorrected) reference pair Q^2 distribution;
- n_{like} is the sum of the bins in the *normalizing region* of the like pair Q^2 distribution;
- n_{ref} is the sum of the bins in the *normalizing region* of the reference pair Q^2 distribution;
- $T_{\pi\pi}$ is the fraction of $\pi_t\pi_t$ pairs in the set of all $\pi\pi$ pairs, listed in Table 4.5.

The *normalizing region* referred to in the definition of n_{like} and n_{ref} is a region of Q^2

where the like pair distribution and the unlike pair distribution follow each other's shape, namely the like and reference pairs exhibit the same phase space. This allows us to normalize the like distribution to the unlike one, and to subtract the correct absolute number of pairs from the like pair distribution. The normalizing region for the pair Q^2 distribution is taken as 0.68 GeV^2 to 0.98 GeV^2. Figure 4.4 shows how closely the like and unlike pair distributions follow each other in this region.

The corresponding pion misidentification correction for the unlike pair Q^2 distribution is given by

$$B_{ref}^{corr} = B_{ref} - \frac{n_{ref}}{n_{ref}} B_{ref}(1 - T_{\pi\pi}) = B_{ref} T_{\pi\pi},$$

where all the quantities are defined above except

- B_{ref}^{corr} is the content of the bin in the PMC-corrected reference pair Q^2 distribution.

Because the correction only multiplies the reference sample distribution by a constant factor, we do not apply it to the reference pairs. As we will see later, the fitting procedure takes into account any correction to the normalization of the study sample to the reference sample.

4.6.2 Tracking

The drift chamber tracking performance affects this analysis in three ways. First, the two track resolution limit dictates how small a Q^2 and thus how large a parameter r (Eqn. 1.3) we can resolve. Second, there is the question of how much the Bose-Einstein enhancement is broadened by the finite momentum resolution of the drift chamber. Finally, any asymmetry in the detection of like versus unlike pairs with small pair angles could influence the ratio R in the region of small Q^2 and hence the measurement of the Bose-Einstein enhancement.

Recall that we have no Monte Carlo data which simulates drift chamber tracking at SPEAR. The following discussion is based on studies done with the MC PEP $q\bar{q}$ data set, namely Monte Carlo simulation of the detector at PEP. We have

seen in Fig. 4.11 that the distribution of pion momenta in the MC PEP $q\bar{q}$ data set follows closely the distribution found in PEP $q\bar{q}$ data. In Fig. 4.15 we show that the the MC PEP $q\bar{q}$ data also reproduces the distribution of the angle between pions in an unlike charged pair. Since the quantity of interest, Q^2, is basically a function of pion three momenta and of the angle between the pions in a pair, the MC PEP $q\bar{q}$ data set is therefore a useful model of the systematic tracking effects in the PEP $q\bar{q}$ data.

Figure 4.16 is a plot of the difference between $\sqrt{Q^2}$ calculated using the Monte Carlo generated momenta and $\sqrt{Q^2}$ calculated using the reconstructed Monte Carlo tracks (see section 3.4), referred to as Q_{gen} and Q_{det}, respectively. This distribution has a full width at half maximum of $\triangle Q = 0.028\ GeV$. We estimate the maximum parameter r that can be observed as

$$r_{max} = \hbar c \sqrt{\frac{\ln 2}{(\triangle Q)^2}} = 5.9\ fm.$$

This is well outside the range of 1 fm, which is the outer limit of the published values found in e^+e^- collision experiments. In order to estimate r_{max} in the SPEAR data, we note that average event multiplicity at SPEAR was less than at PEP, making it easier for the tracking routine to find a pair at SPEAR than in the crowded jet environment at PEP. However, the tracking routine at SPEAR was less efficient than the one used at PEP. The two effects compete, so we make a rough estimate that the value of r_{max} for the SPEAR data is nearly the same as that found for the PEP data.

One of the major systematic errors in this analysis is the broadening of the Bose-Einstein enhancement due to the momentum resolution. To study this effect alone, without introducing complications due to pion misidentification, we consider particles which are both generated and detected pions. The Bose-Einstein enhancement is simulated in the Monte Carlo data by weighting each like charged pion pair by Eqn. 1.3 with given values for parameters α and r. We use $\alpha = 1.00$ and $r = 1.00\ fm$. Distributions in Q^2_{gen} and Q^2_{det} are made for like, weighted like,

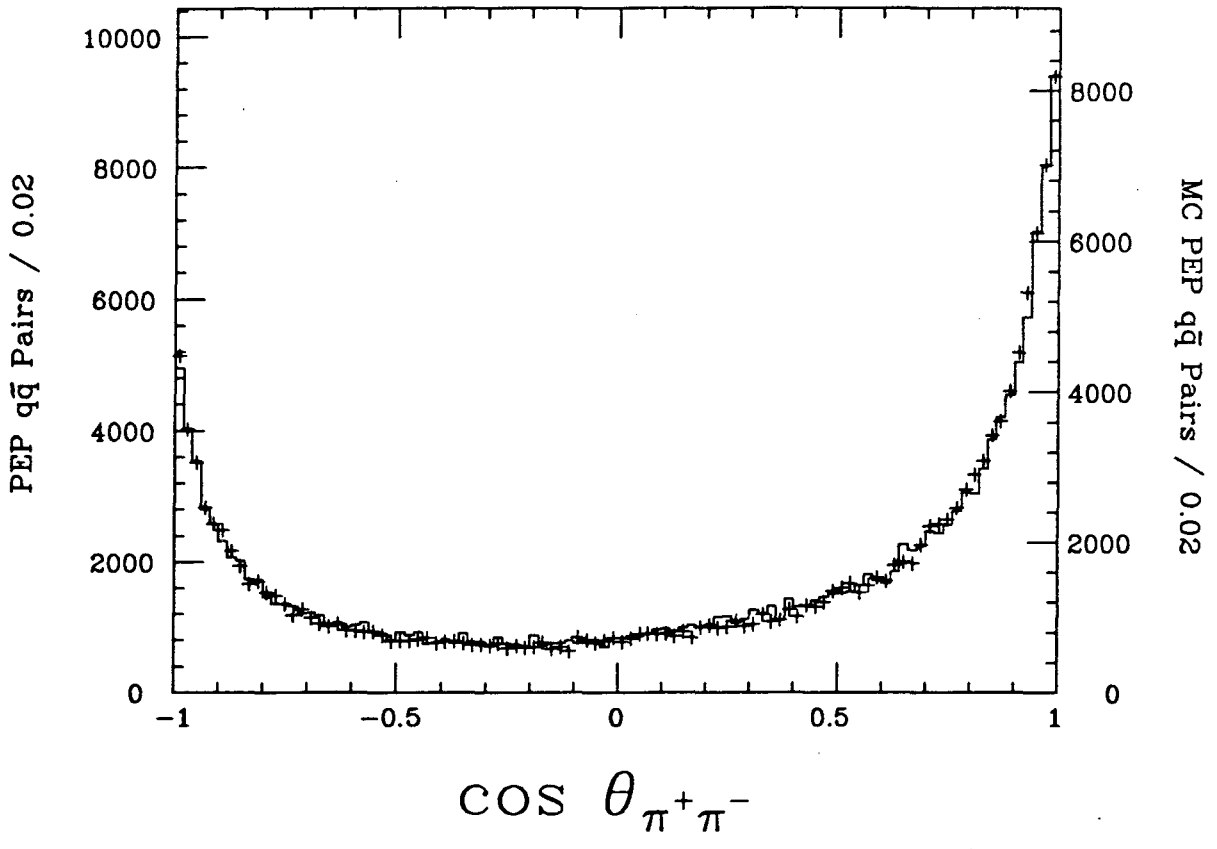

Figure 4.15 *Distribution of the angle between pions in an unlike charged pair in the PEP $q\bar{q}$ data (points) and in the MC PEP $q\bar{q}$ data set (histogram).*

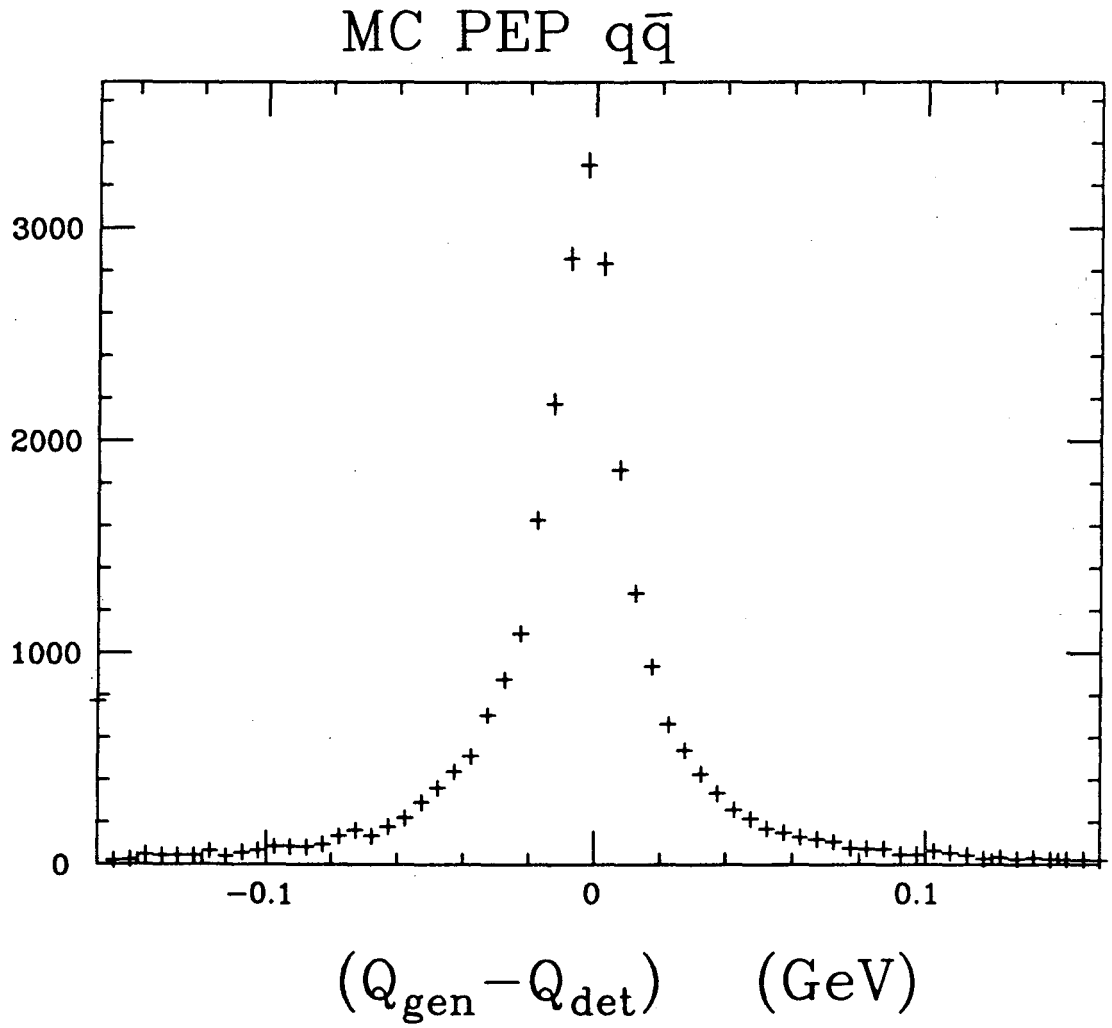

Figure 4.16 *Distribution of $(Q_{gen} - Q_{det})$ for the MC PEP $q\bar{q}$ data set.*

and unlike pion pairs. Two ratios are formed for both Q^2_{gen} and Q^2_{det}: R_{mc} of like to unlike pairs and R_{wt} of weighted like to unlike pairs. As discussed in section 4.5.1, taking the ratio of R_{wt}/R_{mc} removes the evidence of resonances in the reference sample as well as the long range correlations evident in PEP $q\bar{q}$ and MC PEP $q\bar{q}$ data. The ratio R_{wt}/R_{mc} is then fitted to Eqn. 1.3, for both Q^2_{gen} and Q^2_{det}, and the results of the fit are shown in Table 4.6. Based on these numbers, we assign a systematic error of 5% in α and 3% in r due to the momentum resolution. These values apply to the PEP data, since the Monte Carlo uses PEP detector simulation. From chapter two we recall that the momentum resolution at SPEAR was slightly better than at PEP, so we take the PEP systematic errors as upper limits for the data at SPEAR.

Table 4.6 *This table shows how much the Bose-Einstein enhancement is broadened by the momentum resolution of the drift chamber. The first row shows the input values of α and r used to simulate the Bose-Einstein enhancement in the Monte Carlo (see text). The second row is the result of the fit to Eqn. 1.3 in Q^2_{gen}, while the third row is the result of the fit in Q^2_{det}.*

	α	$r\ (fm)$
input values	1.00	1.00
fit to $(1+\alpha\exp(-r^2Q^2_{gen}))$	0.99	0.99
fit to $(1+\alpha\exp(-r^2Q^2_{det}))$	0.95	0.97

The asymmetry in the detection of like versus unlike charged pairs at small angles can be the result of an underpopulation of like charged pairs, or an overpopulation of unlike charged pairs, or a combination of the two effects. The underpopulation of like charged pairs is due to the fact that the drift chamber resolves like charged pairs with small pair angles with less efficiency than unlike charged pairs with small pair angles. Two like charged tracks will curl in the same direction under the influence of the magnetic field in the drift chamber. If their momenta are close to each other, and the pair angle is small, the two tracks will overlap. Two

unlike charged tracks will curl in opposite directions, and even if their momenta are nearly the same the tracking program will still be able to separate them. The overpopulation of unlike charged pairs at small angles is the result of γ conversion products: e^+e^- misidentified as an unlike charged pion pair. Most of these conversion pairs are removed by a cut on very small pair angles (see section 3.6), but a residual contamination remains. The combination of these effects can be seen in Fig. 4.8, which shows the ratio R_{mc} of like to unlike pion pairs in the MC PEP $q\bar{q}$ data set. Note that the asymmetry seems to be confined to a dip in the first bin.

Chapter 5. PION TRIPLETS

5.1 GGLP Effect in Pion Triplets

We began chapter one by stating that the wave function of a set of N indistinguishable pions must be symmetric on the interchange of any two of those pions. It follows that the wave function is always symmetric on the interchange of any three pions, so that like charged pion triplets are expected to exhibit a Bose-Einstein enhancement analogous to the GGLP effect in pairs.

What can we learn from the Bose-Einstein correlation in triplets? In order to answer this question, we first consider an elementary derivation and a common parameterization of the GGLP effect in triplets.

5.1.1 Elementary Derivation

Let us consider a simple derivation analogous to the one given for pairs in section 1.2.1. Given N point sources, the probability of producing three pions, of momenta k_1, k_2, and k_3, is given by

$$P(k_1,k_2,k_3) \propto \sum_{\substack{i,j,k \\ l,m,n}}^{N} a_i a_j a_k a_l^* a_m^* a_n^* e^{(ik_1\cdot(r_i-r_l))} e^{(ik_2\cdot(r_j-r_m))} e^{(ik_3\cdot(r_k-r_n))},$$

and the correlation function for pion triplets is given by the ratio

$$R_{3\pi} = \frac{\left\langle \sum_{\substack{i,j,k \\ l,m,n}}^{N} a_i a_j a_k a_l^* a_m^* a_n^* e^{(ik_1\cdot(r_i-r_l))} e^{(ik_2\cdot(r_j-r_m))} e^{(ik_3\cdot(r_k-r_n))} \right\rangle}{\left\langle \sum_{i,l}^{N} a_i a_l^* e^{(ik_1\cdot(r_i-r_l))} \right\rangle \left\langle \sum_{j,m}^{N} a_j a_m^* e^{(ik_2\cdot(r_j-r_m))} \right\rangle \left\langle \sum_{k,n}^{N} a_k a_n^* e^{(ik_3\cdot(r_k-r_n))} \right\rangle}.$$

The analogous quantity in optics is referred to as a third order correlation function.

If the N source amplitudes are chaotic with respect to each other, terms in the numerator with $(i \neq l,m,n;\ j \neq l,m,n;\ k \neq l,m,n)$ average out to zero.

Terms in the denominator with $(i \neq l;\ j \neq m;\ k \neq n)$ also average out to zero. The numerator reduces to three sets of terms:

1. $i = l,\ j = m,\ k = n$

   All possible single pion production probabilities:

$$\left\langle \sum_i^N |a_i|^2 \right\rangle \left\langle \sum_j^N |a_j|^2 \right\rangle \left\langle \sum_k^N |a_k|^2 \right\rangle .$$

   Since the denominator also reduces to this expression, the ratio of this numerator term to the denominator is equal to one.

2. $(i = l, j = n, k = m)\ +\ (i = n, j = m, k = l)\ +\ (i = m, j = l, k = n)$

   The sum of all possible production probabilities for one pion plus one pair of pions:

$$\left\langle \sum_i^N |a_i|^2 \right\rangle \left\langle \sum_{\substack{j=n \\ k=m}}^N |a_j|^2 |a_k|^2 e^{(i(k_2-k_3)\cdot(r_j-r_k))} \right\rangle$$

$$+ \left\langle \sum_j^N |a_j|^2 \right\rangle \left\langle \sum_{\substack{i=n \\ k=l}}^N |a_i|^2 |a_k|^2 e^{(i(k_3-k_1)\cdot(r_k-r_i))} \right\rangle$$

$$+ \left\langle \sum_k^N |a_k|^2 \right\rangle \left\langle \sum_{\substack{i=m \\ j=l}}^N |a_i|^2 |a_j|^2 e^{(i(k_1-k_2)\cdot(r_i-r_j))} \right\rangle .$$

   Divided by the denominator, this term becomes a sum of the familiar pair Bose-Einstein enhancements for the three pairs in the triplet.

3. $(i = m, j = n, k = l)\ +\ (i = n, j = l, k = m)$

   The sum of all possible production probabilities for a triplet of pions:

$$\left\langle \sum_{\substack{i=m \\ j=n \\ k=l}}^N |a_i|^2 |a_j|^2 |a_k|^2 e^{(i(k_1-k_2)\cdot r_i)} e^{(i(k_2-k_3)\cdot r_j)} e^{(i(k_3-k_1)\cdot r_k)}$$

$$+\sum_{\substack{i=n\\j=l\\k=m}}^{N}|a_i|^2|a_j|^2|a_k|^2 e^{(-i(k_1-k_3)\cdot r_i)}e^{(-i(k_3-k_2)\cdot r_k)}e^{(-i(k_2-k_1)\cdot r_j)}\Big\rangle.$$

If we relabel the indices in the second term as $i \to j$, $j \to k$, and $k \to i$, then the sum becomes

$$\left\langle 2\mathrm{Re}\Big(\sum_{i,j,k}^{N}|a_i|^2|a_j|^2|a_k|^2 e^{(i(k_1-k_2)\cdot r_i)}e^{(i(k_2-k_3)\cdot r_j)}e^{(i(k_3-k_1)\cdot r_k)}\Big)\right\rangle.$$

This term is the pure triplet Bose-Einstein enhancement.

In the limit of a continuous source distribution, $N \to \infty$, the triplet correlation function becomes Eqn. 5.1

$$R_{3\pi} = 1 + \alpha|\rho(k_1-k_2)|^2 + \alpha|\rho(k_2-k_3)|^2 + \alpha|\rho(k_3-k_1)|^2 \qquad (5.1)$$

$$+2\mu\mathrm{Re}\Big(\rho(k_1-k_2)\rho(k_2-k_3)\rho(k_3-k_1)\Big),$$

where ρ is the Fourier transform of the source distribution, and α and μ account for a partially coherent source as in section 1.2.3:

$$\text{fully chaotic source : } \alpha = 1, \quad \mu = 1$$

$$\text{fully coherent source : } \alpha = 0, \quad \mu = 0$$

$$\text{partially coherent source : } 0 < \alpha < 1, \quad 0 < \mu < 1.$$

We can see from Eqn. 5.1 that the Bose-Einstein enhancement in pion triplets consists of contributions from each of the three pairs in the triplet plus a purely triplet enhancement term.

5.1.2 Parameterization

To get an idea of what the triplet enhancement looks like, we substitute the parameterization for ρ used in pair analysis

$$|\rho(k_i-k_j)|^2 \approx e^{-r^2Q_{ij}^2}$$

and

$$|\rho(k_i - k_j)| \approx e^{-\frac{1}{2}r^2Q_{ij}^2},$$

where

$$Q_{ij}^2 \equiv -(k_i - k_j).$$

We cannot calculate the product $(\rho(k_1 - k_2)\rho(k_2 - k_3)\rho(k_3 - k_1))$ in general, but to the extent that phase factors can be neglected, $R_{3\pi}$ becomes

$$R_{3\pi} = 1 + \alpha e^{-r^2Q_{12}^2} + \alpha e^{-r^2Q_{23}^2} + \alpha e^{-r^2Q_{31}^2} + 2\mu e^{-\frac{1}{2}r^2Q_{3\pi}^2},$$

where

$$Q_{3\pi}^2 \equiv Q_{12}^2 + Q_{23}^2 + Q_{31}^2.$$

Note that the r in this equation is the same r as in the pair parameterization, and that $Q_{3\pi}^2$ is analogous to Q_{ij}^2 in the sense that

$$Q_{3\pi}^2 = M_{3\pi}^2 - 9m_\pi^2,$$

where $M_{3\pi}$ is the invariant mass of the three pions.

This triplet parameterization implies that the proper way to observe the Bose-Einstein enhancement in triplets is to consider the three-dimensional manifold $(Q_{12}^2, Q_{23}^2, Q_{31}^2)$. In analogy to the pair analysis, we should cumulate a three dimensional histogram in these variables for both the study sample and the reference sample, and then fit the ratio to the parameterization above. In practice, however, low statistics make this method impractical.

In analogy to the pion pair analysis, the GGLP effect in triplets is parameterized[40] as Eqn. 5.2

$$R_{3\pi} = 1 + \alpha_{3\pi} e^{-r_{3\pi}^2 Q_{3\pi}^2}. \tag{5.2}$$

In this case we need to cumulate one-dimensional histograms in $Q_{3\pi}^2$ for the study and reference samples. The strength of the purely triplet enhancement μ can be extracted in the limit of small pair Q_{ij}^2's,

$$\alpha_{3\pi} \approx 3\alpha + 2\mu.$$

The triplet variable $r_{3\pi}$ is related to the pair variable r in a complicated way, but we can put limits on it if we assume that $Q_{3\pi}^2 \approx 3Q_{ij}^2$ in the region of interest (small Q_{ij}^2). In such a case,

$$1 + \alpha_{3\pi} e^{-3r_{3\pi}^2 Q_{ij}^2} \approx 1 + 3\alpha e^{-r^2 Q_{ij}^2} + 2\mu e^{-\frac{3}{2}r^2 Q_{ij}^2}.$$

Substituting the expression for $\alpha_{3\pi}$ in the limit of small Q_{ij}^2, we get

$$e^{-3r_{3\pi}^2 Q_{ij}^2} \approx \begin{cases} e^{-r^2 Q_{ij}^2} \\ \text{to} \\ e^{-\frac{3}{2}r^2 Q_{ij}^2} \end{cases},$$

so that

$$r_{3\pi}^2 \approx \begin{cases} r^2/3 \\ \text{to} \\ r^2/2 \end{cases}.$$

With these relationships in mind, there are two things we can learn from the GGLP effect in triplets. First, we must check whether it makes sense to use the pair parameterization for ρ in triplet analysis. To do this, we compare the measured values of $\alpha_{3\pi}$ and $r_{3\pi}$ with the measured values of α and r to see if the measurements are consistent within the relationships given above. If they are consistent, we can derive the purely triplet enhancement μ from the measured values of α and $\alpha_{3\pi}$.

5.2 Data Analysis for Pion Triplets

This section contains details specific to the analysis of pion triplets. It follows closely the analysis for pairs described in chapter four.

5.2.1 Study and Reference Samples

The general comments made for the pair study sample in section 4.2 and the pair reference sample in section 4.3 apply equally well to triplets. As in the case of pairs, both the triplet study sample and the triplet reference sample are subject to

the effects of kinematical phase space restrictions, final state dynamics, and detector performance. These are discussed in more detail in section 5.2. Figure 5.1 shows the distribution of like charged triplets in $Q^2_{3\pi}$.

The selection of a triplet reference sample poses a problem, since we have no way of creating a triplet of unlike charged pions out of π^+'s and π^-'s alone. The only natural reference sample available consists of $\pi^\pm\pi^\pm\pi^\mp$ triplets, which contain one like charged and therefore Bose-Einstein correlated pair. We will refer to this as the $\pm\pm\mp$ reference sample. The ratio of the triplet study sample to the $\pm\pm\mp$ reference sample would not exhibit the full Bose-Einstein enhancement for triplets. Instead, we expect to see an enhancement on the order of

$$\lim_{Q^2_{ij}\to 0} \frac{R_{3\pi}}{R} \approx \frac{1+3\alpha+2\mu}{1+\alpha}.$$

Figure 5.2 shows the distribution of $\pi^\pm\pi^\pm\pi^\mp$ triplets in $Q^2_{3\pi}$.

An alternative reference sample can be created using the cluster mixing routine. We have shown in section 4.3.4 (Fig. 4.6) that pairs made of one pion from the analysis event and one pion from a stored cluster have the same kinematical phase space as unlike charged pairs from a single event. Thus if we make a triplet consisting of one pion from a stored cluster and an unlike charged pair from the analysis event, we have in effect a triplet of unlike charged pions. We will call this the mixed cluster reference sample. The ratio of the triplet study sample to the cluster mixed reference sample is therefore expected to exhibit the full triplet Bose-Einstein enhancement.

5.2.2 Final State Coulomb Force Effects

In section 4.5.3 we discussed the Gamow factor, which corrects for the final state Coulomb interaction between the two charged pions in a pair. The extension of this correction to charged pion triplets was derived by Liu[41]. If we label the three pions in a triplet as 1, 2, and 3, then the charged triplet distribution $P_c(k_1,k_2,k_3)$ is related to the same distribution in the absence of the Coulomb

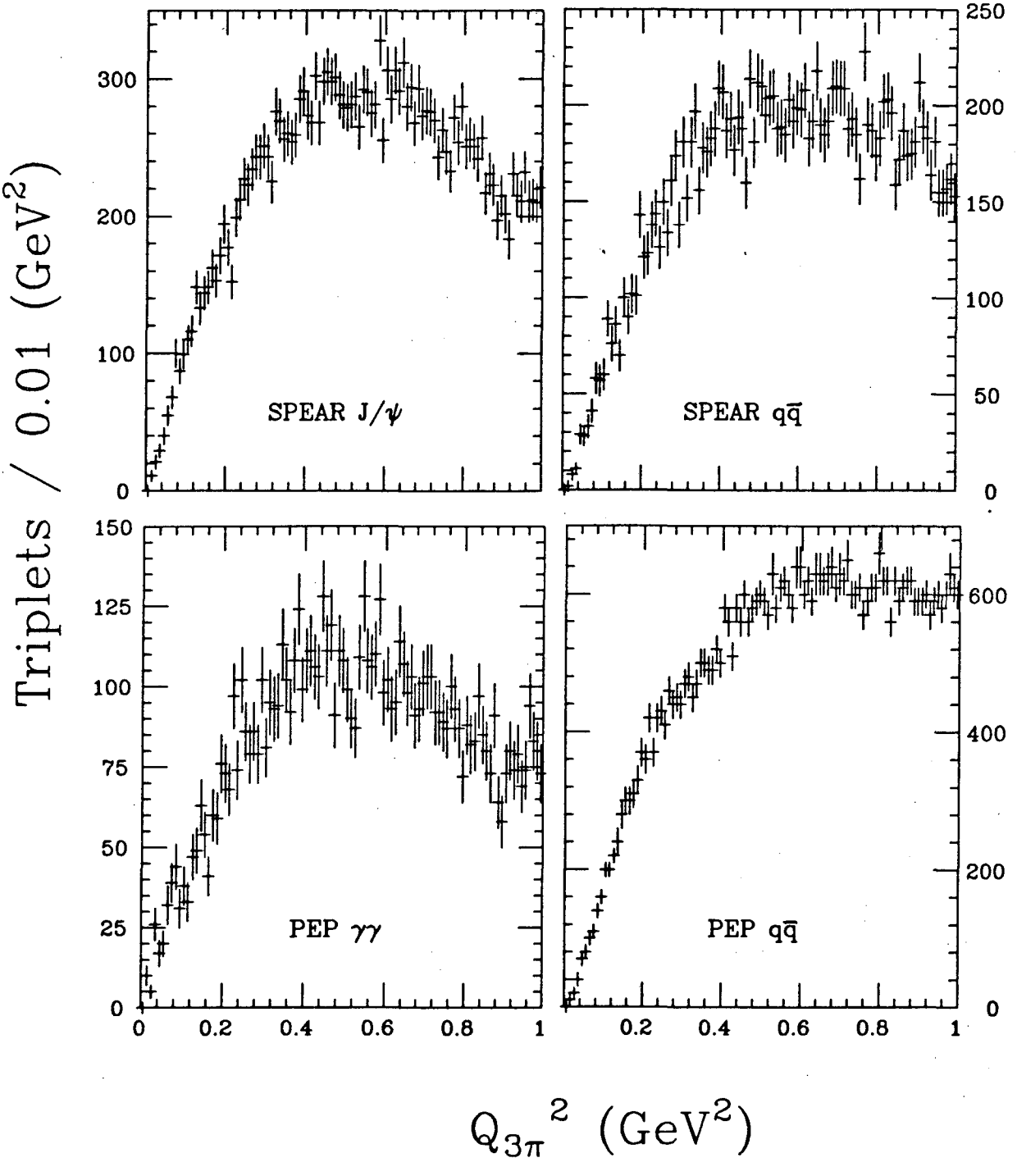

Figure 5.1 *Distributions of like charged triplets in $Q^2_{3\pi}$ for the four data sets.*

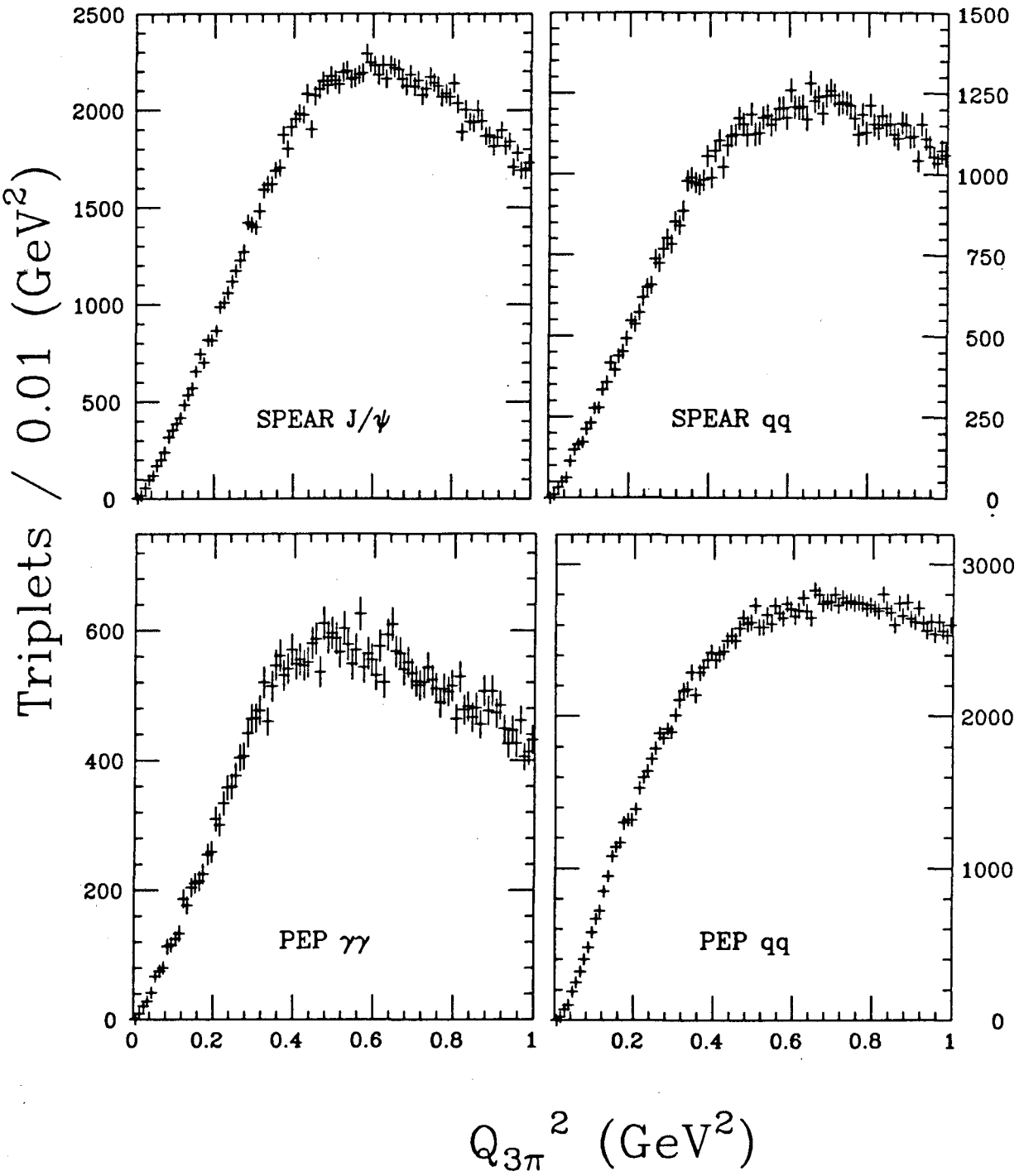

Figure 5.2 *Distributions of $\pm\pm\mp$ reference triplets in $Q^2_{3\pi}$ for the four data sets.*

interaction $P_n(k_1, k_2, k_3)$ as follows:

$$P_c(k_1, k_2, k_3) = G(\xi_{12})G(\xi_{23})G(\xi_{31})P_n(k_1, k_2, k_3),$$

where

$$G(\xi_{ij}) = \begin{cases} G_l(\eta_{ij}), & \text{for a like charged pair;} \\ G_u(\eta_{ij}), & \text{for an unlike charged pair.} \end{cases}$$

This result describes to first order in α the Coulomb interaction within the three pairs of the pion triplet.

Let us consider the specific categories of charged triplets which we deal with. The like charged triplet contains three like charged pairs, so the Gamow correction is given by

$$C_1 \equiv G_l(\eta_{12})G_l(\eta_{23})G_l(\eta_{31}).$$

The $\pm\pm\mp$ reference sample triplet contains one like charged pair and two unlike charged pairs, so this reference sample is corrected using

$$C_2 \equiv G_l(\eta_{12})G_u(\eta_{23})G_u(\eta_{31}).$$

Finally, the mixed cluster reference sample triplet contains one unlike charged pair and two effectively neutral pairs, so this reference sample is corrected with

$$C_3 \equiv G_u(\eta_{12}).$$

In analogy to the procedure in pairs, the Coulomb correction for triplets is done by weighting each like charged triplet with $1/C_1$, each $\pm\pm\mp$ triplet with $1/C_2$, and each mixed cluster reference triplet with $1/C_3$.

5.2.3 Pion Misidentification

Using the MC SPEAR J/ψ, MC SPEAR $q\bar{q}$, MC PEP $\gamma\gamma$, and MC PEP $q\bar{q}$ data sets described in section 4.6.1, we calculate the fraction of triplets which contain one or more misidentified pions. Figure 5.3 and Fig. 5.4 show the fraction

of $\pi_t\pi_t\pi_t$ in the set of all $\pi\pi\pi$ as a function of $Q^2_{3\pi}$ for like charged triplets and for $\pm\pm\mp$ triplets, respectively. Within statistics, there is no significant variation of this fraction with the charge of the triplet or with $Q^2_{3\pi}$, so we average the fraction over the charge of the triplet and over $Q^2_{3\pi}$. The average values are listed in Table 5.1. However, these averages alone are not enough to correct for pion misidentification in triplets.

Recall from the example of pair analysis that correcting for pion misidentification requires us to model the behavior of the contaminating triplets in $Q^2_{3\pi}$. Let us use π_f to denote a particle identified as a pion but which is not a true pion. One part of the contaminating set $(\pi\pi\pi - \pi_t\pi_t\pi_t)$ consists of $\pi_t\pi_t\pi_f$, which behaves like the $\pm\pm\mp$ reference sample. The other part of the contaminating set consists of $\pi_t\pi_f\pi_f$ and $\pi_f\pi_f\pi_f$, both of which behave like the mixed cluster reference sample. The relative contributions of all these contaminants are listed in Table 5.1.

We can now proceed to correct for pion misidentification in like charged triplets by using these fractions and both $\pm\pm\mp$ and mixed cluster reference sample distributions. Note that the $\pm\pm\mp$ reference sample we use below is also subject to contamination by $\pi_t\pi_f\pi_f$ and $\pi_f\pi_f\pi_f$, which lowers the observed Bose-Einstein enhancement from the like pair in the reference triplet. However, this is a second order effect in our correction, and we neglect it. Also, as in the case of pairs, all the distributions used in the pion misidentification correction for triplets have been first corrected for appropriate Coulomb interactions.

Analogous to pairs, the pion misidentification correction (PMC) is done bin by bin on like triplet $Q^2_{3\pi}$ distributions as follows:

$$B^{corr}_{like} = B_{like} - \frac{n_{like}}{n_{\pm\pm\mp}} B_{\pm\pm\mp} F_1 - \frac{n_{like}}{n_{mix}} B_{mix}(F_2 + F_3),$$

where

- B^{corr}_{like} is the content of the bin in the PMC-corrected like triplet $Q^2_{3\pi}$ distribution;
- B_{like} is the content of the bin in the PMC-uncorrected like triplet

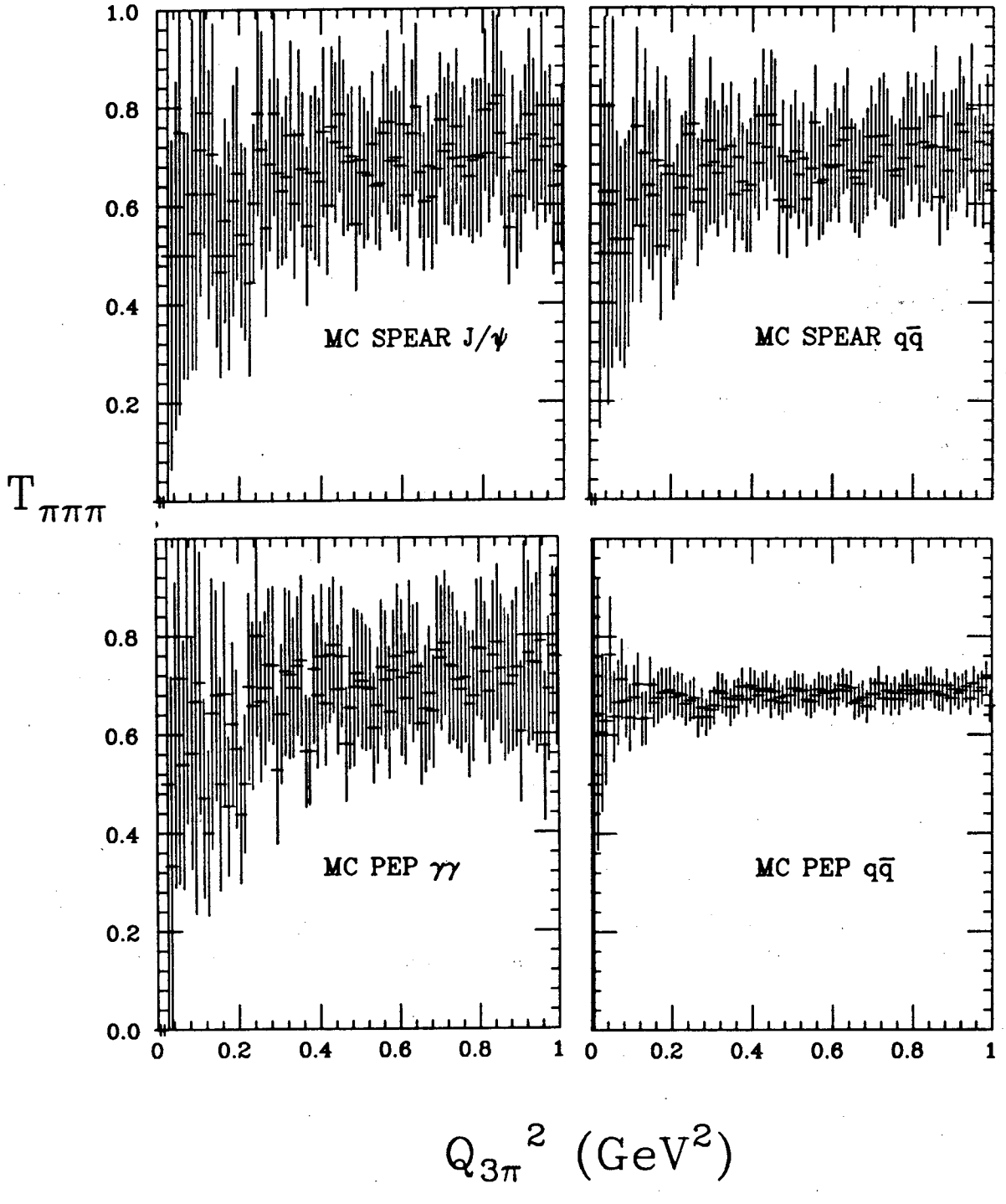

Figure 5.3 *A study done with Monte Carlo data showing the fraction $T_{\pi\pi\pi}$ of like charged triplets of correctly identified pions $\pi_t\pi_t\pi_t$ in the set of like charged triplets of particles identified as pions $\pi\pi\pi$. The fraction is shown as a function of $Q^2_{3\pi}$.*

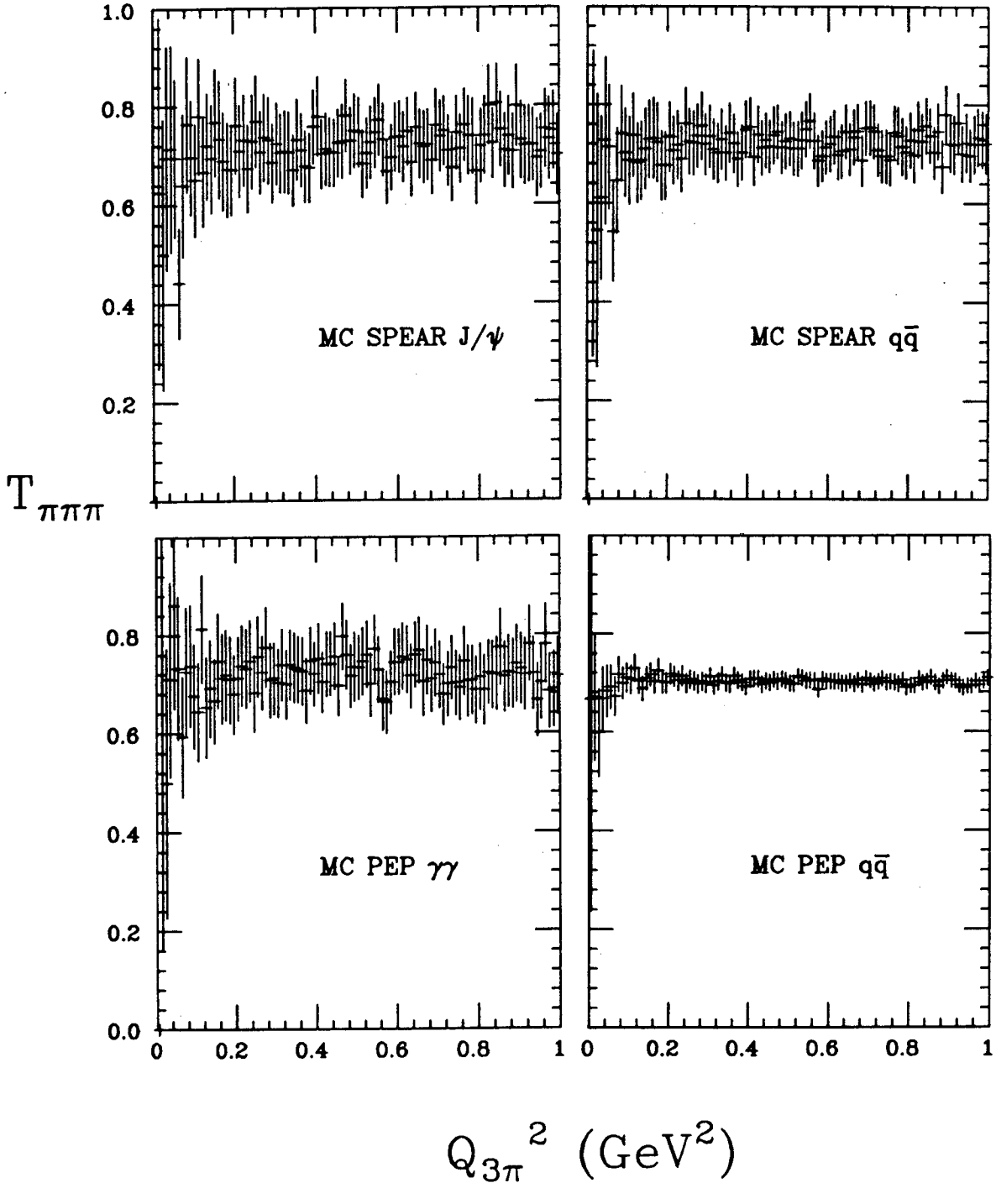

Figure 5.4 *A study done with Monte Carlo data showing the fraction $T_{\pi\pi\pi}$ of $\pm\pm\mp$ triplets of correctly identified pions $\pi_t\pi_t\pi_t$ in the set of $\pm\pm\mp$ triplets of particles identified as pions $\pi\pi\pi$. The fraction is shown as a function of $Q^2_{3\pi}$.*

Table 5.1 *The fractions plotted in Fig. 5.3 and Fig. 5.4 are averaged over the charge combination and over $Q^2_{3\pi}$, and the average values are listed in the first column. The second, third, and fourth columns contain the same averages for three kinds of contaminating triplets: $\pi_t\pi_t\pi_f$, $\pi_t\pi_f\pi_f$, and $\pi_f\pi_f\pi_f$, respectively.*

Monte Carlo Data Set	$T_{\pi\pi\pi} \equiv \left\langle \frac{\pi_t\pi_t\pi_t}{\pi\pi\pi} \right\rangle$	$F_1 \equiv \left\langle \frac{\pi_t\pi_t\pi_f}{\pi\pi\pi} \right\rangle$	$F_2 \equiv \left\langle \frac{\pi_t\pi_f\pi_f}{\pi\pi\pi} \right\rangle$	$F_3 \equiv \left\langle \frac{\pi_f\pi_f\pi_f}{\pi\pi\pi} \right\rangle$
MC SPEAR J/ψ	0.73	0.24	0.02	< 0.01
MC SPEAR $q\bar{q}$	0.72	0.25	0.02	< 0.01
MC PEP $\gamma\gamma$	0.71	0.26	0.02	< 0.01
MC PEP $q\bar{q}$	0.64	0.30	0.05	< 0.01

$Q^2_{3\pi}$ distribution;

- $B_{\pm\pm\mp}$ is the content of the bin in the (PMC-uncorrected) $\pm\pm\mp$ reference triplet $Q^2_{3\pi}$ distribution;
- B_{mix} is the content of the bin in the (PMC-uncorrected) mixed cluster reference triplet $Q^2_{3\pi}$ distribution;
- n_{like} is the sum of the content of the bins in the *normalizing region* of the like triplet $Q^2_{3\pi}$ distribution;
- $n_{\pm\pm\mp}$ is the sum of the content of the bins in the normalizing region of the $\pm\pm\mp$ reference triplet $Q^2_{3\pi}$ distribution;
- n_{mix} is the sum of the content of the bins in the normalizing region of the mixed cluster reference triplet $Q^2_{3\pi}$ distribution;
- F_1 is the fraction of $\pi_t\pi_t\pi_f$ triplets in the set of all $\pi\pi\pi$ triplets, listed in Table 5.1;
- F_2 is the fraction of $\pi_t\pi_f\pi_f$ triplets in the set of all $\pi\pi\pi$ triplets, listed in Table 5.1;
- F_3 is the fraction of $\pi_f\pi_f\pi_f$ triplets in the set of all $\pi\pi\pi$ triplets, listed in Table 5.1.

The normalizing region referred to above is used here the same way as it

was used in section 4.6.1 for the PMC-correction in pairs. We take 0.50 GeV^2 to 1.00 GeV^2 as the normalizing region for the triplet $Q^2_{3\pi}$ distribution.

5.2.4 *Tracking*

Drift chamber tracking performance affects triplet analysis much the same way as it affects pair analysis. We follow section 4.6.2 and first consider the maximum value of the parameter $r_{3\pi}$ that the detector can resolve. Figure 5.5 is a plot of the difference between $\sqrt{Q^2_{3\pi}}$ calculated using Monte Carlo generated momenta and the same quantity calculated using the reconstructed tracks, referred to as $Q_{3\pi\ gen}$ and $Q_{3\pi\ det}$, respectively. Then we estimate $r_{3\pi\ max}$ as

$$r_{3\pi\ max} = \hbar c \sqrt{\frac{\ln 2}{(\triangle Q_{3\pi})^2}} = 3.8\ fm,$$

where $\triangle Q_{3\pi} = 0.05\ GeV$ is the full width at half maximum of the distribution in Fig. 5.5. As in the case of pair analysis, $r_{3\pi\ max}$ is well outside the typical values of $r_{3\pi}$.

As we did for pairs, we use Monte Carlo data to study the broadening of the observed Bose-Einstein enhancement in triplets due to the momentum resolution. Again, we look only at particles which are both generated and detected as pions. The Bose-Einstein enhancement in triplets is simulated in Monte Carlo data by weighting each like charged pion triplet by Eqn. 5.2 with given values of $\alpha_{3\pi}$ and $r_{3\pi}$. Although the maximum value of $\alpha_{3\pi}$ is expected to be close to 5.00, we use $\alpha_{3\pi} = 2.00$ and $r_{3\pi} = 1.00\ fm$ because these values are closer to the uncorrected values measured in our data. Distributions in $Q^2_{3\pi\ gen}$ and $Q^2_{3\pi\ det}$ are made for like, weighted like, and $\pm\pm\mp$ triplets. Two ratios are then made for both $Q^2_{3\pi\ gen}$ and $Q^2_{3\pi\ det}$: $R_{3\pi\ mc}$ of like to $\pm\pm\mp$ triplets, and $R_{3\pi\ wt}$ of weighted like to $\pm\pm\mp$ triplets. The ratio $R_{3\pi\ wt}/R_{3\pi\ mc}$ is then fitted to Eqn. 5.2, for both $Q^2_{3\pi\ gen}$ and $Q^2_{3\pi\ det}$, and the results of the fit are shown in Table 5.2. Based on these numbers, we assign a systematic error of 13% in $\alpha_{3\pi}$ and 3% in $r_{3\pi}$ due to the momentum resolution.

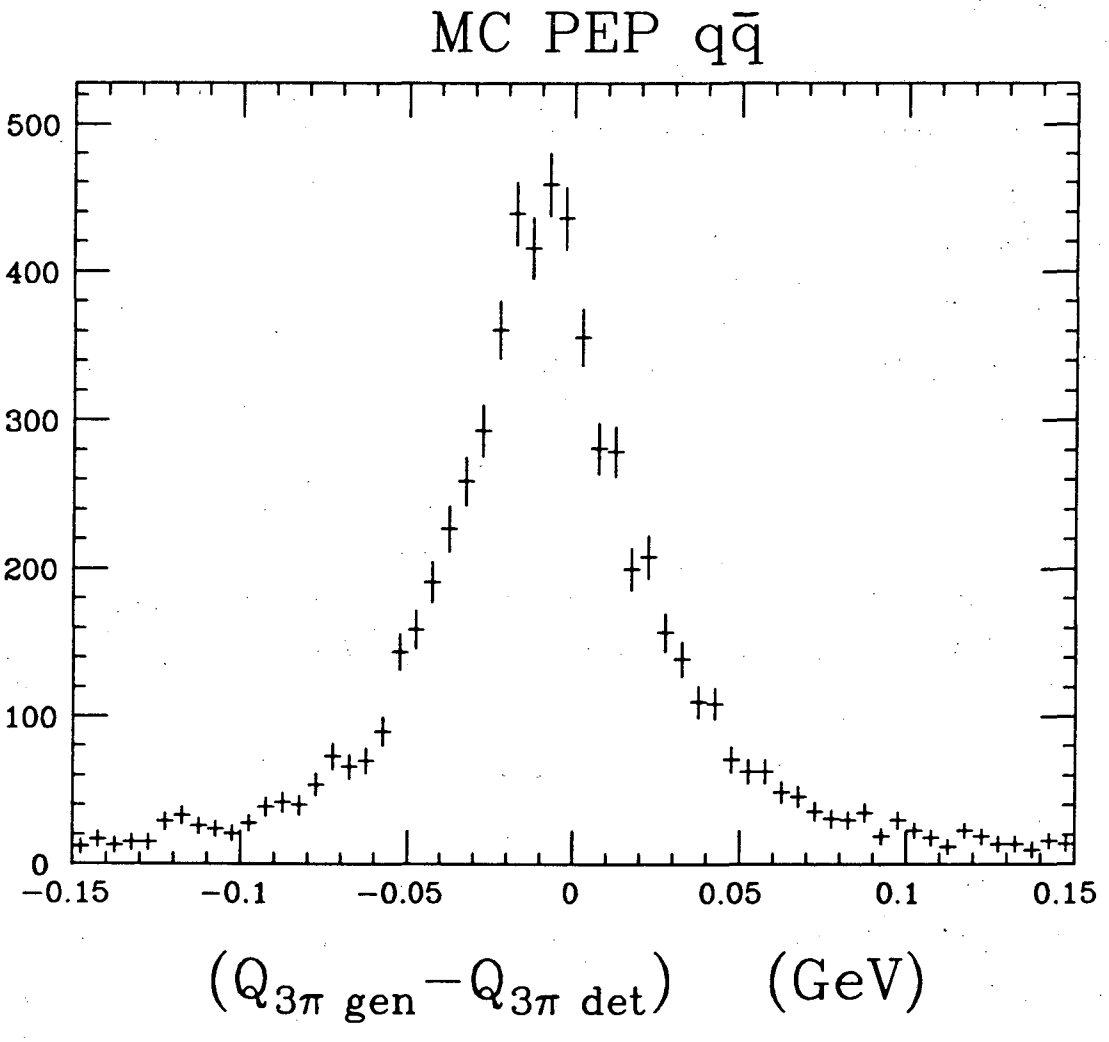

Figure 5.5 *Distribution of* $(Q_{3\pi\ gen} - Q_{3\pi\ det})$ *for the MC PEP* $q\bar{q}$ *data set.*

Table 5.2 *This table shows how much the Bose-Einstein enhancement in triplets is broadened by the momentum resolution of the drift chamber. The first row shows the input values of $\alpha_{3\pi}$ and $r_{3\pi}$ used to simulate the Bose-Einstein enhancement in the Monte Carlo (see text). The second row is the result of the fit to Eqn. 5.2 in $Q^2_{3\pi\ gen}$, while the third row is the result of the fit in $Q^2_{3\pi\ det}$.*

	$\alpha_{3\pi}$	$r_{3\pi}$ (fm)
input values	2.00	1.00
fit to $(1+\alpha_{3\pi}\exp(-r^2_{3\pi}Q^2_{3\pi\ gen}))$	1.95	0.99
fit to $(1+\alpha_{3\pi}\exp(-r^2_{3\pi}Q^2_{3\pi\ det}))$	1.77	0.97

Chapter 6. RESULTS AND DISCUSSION

6.1 GGLP Effect in Pion Pairs

6.1.1 Calculation and Fitting of the Pair Correlation Function

We make two corrections before taking any ratios: the Coulomb correction to the like charged pair distribution and to the unlike charged pair distribution (section 4.5.3), and the pion misidentification correction to the like charged pair distribution (section 4.6.1). Data that has been corrected using both of these is referred to as fully corrected data.

Recall that the ratio R of study sample to reference sample is parameterized in chapter one as

$$R = (1 + \alpha\, e^{-r^2Q^2}).$$

In section 4.5.1, we discussed how the modification

$$R = (1 + \delta\, Q^2)\, (1 + \alpha\, e^{-r^2Q^2})$$

takes into account the presence of long range correlations in the data. We introduce one more parameter, γ, to reflect the overall normalization of the number of like charged pairs to the number of reference pairs. Then the complete expression we use in fitting R is

$$R = \gamma\, (1 + \delta\, Q^2)\, (1 + \alpha\, e^{-r^2Q^2}).$$

All the fits are done by minimizing the χ^2 with the utility minimization routine MINUIT[42]. For the ratio of like to unlike charged pairs, fitting R to the last expression above is done over the following regions of Q^2:

$$0.00\ GeV^2 < Q^2 < 0.12\ GeV^2,$$
$$0.20\ GeV^2 < Q^2 < 0.36\ GeV^2,$$
$$0.68\ GeV^2 < Q^2 < 1.00\ GeV^2.$$

These regions avoid the K^0 and ρ^0 resonances, and since they cover 57 bins with four parameters they constitute $(57 - 4 = 53)$ degrees of freedom. For the ratio of like charged pairs to mixed cluster pairs, fitting R is done over

$$0.00\ GeV^2 < Q^2 < 1.00\ GeV^2.$$

In this case, there is no need to avoid any regions in Q^2, and the number of degrees of freedom is $(99 - 4 = 95)$.

Recall that we make a cut on small pair angles ($\cos\theta_{pair} \leq 0.997$) in both the study sample and the reference sample in order to remove products of $\gamma \rightarrow e^+e^-$ which can be misidentified as an unlike charged pair. This cut falls well within the first bin of the Q^2 distribution. We test its effect on the fitted parameters by comparing the results with and without the first bin included in the fitting region. The two results are the same within a fraction of the statistical error for all four data sets, so we keep the first bin in the fitting region.

Some groups have tried other fitting expressions for R. A comparison of several fitting expressions is shown in Table 6.1 for the case of the uncorrected SPEAR J/ψ data. We find that the expression we have chosen ((3) in the table) describes the data as well if not better than the others listed. Expression (5), which involves two Gaussians, has recently[4] been put forward as a better description of R in the region of small Q^2. In our fit to the SPEAR J/ψ data, which has the highest statistics of the four data sets, the values of r_1 and r_2 come out the same regardless of the initial values given to MINUIT. Similarly, regardless of the initial values of α_1 and α_2, the sum of their fitted values always comes out to be the same as the value for α in expression (3). Thus we conclude that expression (5) gives the same information as expression (3).

The results of the fits for the pair study sample are shown in Table 6.2 and Table 6.3 for no corrections and all corrections, respectively. The corresponding distributions and fitted curves are shown in Fig. 6.1, Fig. 6.2, Fig. 6.3, and Fig. 6.4.

In the sections that follow, we discuss the results found using the unlike charged pair reference sample. The mixed cluster reference sample results are discussed in detail in section 6.1.6.

Table 6.1 *The results of fitting to various expressions for R for uncorrected SPEAR J/ψ data. The errors shown are statistical.*

FITTING EXPRESSION	FIT VALUES
(1) $\gamma(1+\alpha e^{-r^2Q^2})$ no pre-normalization (see section 6.1.2)	$\alpha = 0.70 \pm 0.02$ $r = 0.76 \pm 0.02\ fm$ $\gamma = 0.58 \pm 0.01$ $\chi^2/DOF = 58/54$
(2) $\gamma(1+\alpha e^{-r^2Q^2})$	$\alpha = 0.70 \pm 0.02$ $r = 0.76 \pm 0.02\ fm$ $\gamma = 0.98 \pm 0.01$ $\chi^2/DOF = 58/54$
(3) $\gamma(1+\delta Q^2)(1+\alpha e^{-r^2Q^2})$	$\alpha = 0.69 \pm 0.03$ $r = 0.77 \pm 0.02\ fm$ $\gamma = 0.99 \pm 0.01$ $\delta = -0.01 \pm 0.02$ $\chi^2/DOF = 57/53$
(4) $\gamma(1+\alpha e^{-rQ})$	$\alpha = 1.19 \pm 0.03$ $r = 1.11 \pm 0.05\ fm$ $\gamma = 0.95 \pm 0.01$ $\chi^2/DOF = 119/54$
(5) $\gamma(1+\alpha_1 e^{-r_1^2Q^2}+\alpha_2 e^{-r_2^2Q^2})$	$\alpha_1 = 0.51 \pm 0.02$ $\alpha_2 = 0.18 \pm 0.01$ $r_1 = 0.76 \pm 0.05\ fm$ $r_2 = 0.76 \pm 0.13\ fm$ $\gamma = 0.98 \pm 0.01$ $\delta = -0.01 \pm 0.02$ $\chi^2/DOF = 58/51$

Table 6.2 *Fit results for the pion pair study sample with no corrections. The first error shown is statistical while the second is systematic.*

PION PAIRS IN PAIR ANALYSIS EVENTS ($N_\pi \geq 3$) NO CORRECTIONS FIT TO: $R = \gamma(1+\delta Q^2)(1+\alpha\exp(-r^2Q^2))$				
parameter	SPEAR J/ψ	SPEAR $q\bar{q}$	PEP $\gamma\gamma$	PEP $q\bar{q}$
REFERENCE SAMPLE: UNLIKE CHARGED PAIRS				
α	$0.69 \pm 0.03 \pm 0.04$	$0.46 \pm 0.04 \pm 0.03$	$0.56 \pm 0.05 \pm 0.03$	$0.28 \pm 0.02 \pm 0.02$
r (fm)	$0.77 \pm 0.02 \pm 0.03$	$0.63 \pm 0.06 \pm 0.03$	$0.74 \pm 0.07 \pm 0.03$	$0.75 \pm 0.03 \pm 0.03$
δ (GeV^{-2})	$-0.01 \pm 0.02 \pm 0.01$	$0.07 \pm 0.04 \pm 0.01$	$-0.06 \pm 0.04 \pm 0.01$	$0.18 \pm 0.01 \pm 0.02$
γ	$0.99 \pm 0.01 \pm 0.01$	$0.95 \pm 0.03 \pm 0.01$	$1.00 \pm 0.03 \pm 0.01$	$0.95 \pm 0.01 \pm 0.01$
χ^2/DOF	57/53	65/53	48/53	89/53
REFERENCE SAMPLE: MIXED CLUSTER PAIRS				
α	$0.69 \pm 0.02 \pm 0.04$	$0.55 \pm 0.03 \pm 0.03$	$0.89 \pm 0.06 \pm 0.05$	$0.27 \pm 0.04 \pm 0.02$
r (fm)	$0.70 \pm 0.02 \pm 0.03$	$0.72 \pm 0.03 \pm 0.03$	$0.99 \pm 0.05 \pm 0.04$	$0.99 \pm 0.12 \pm 0.04$
δ (GeV^{-2})	$0.26 \pm 0.03 \pm 0.02$	$-0.01 \pm 0.02 \pm 0.01$	$0.09 \pm 0.03 \pm 0.01$	$0.13 \pm 0.02 \pm 0.01$
γ	$0.90 \pm 0.01 \pm 0.01$	$0.98 \pm 0.01 \pm 0.01$	$0.97 \pm 0.01 \pm 0.01$	$0.97 \pm 0.01 \pm 0.01$
χ^2/DOF	139/95	87/95	99/95	137/95

Table 6.3 *Fit results for the pion pair study sample with both Coulomb and pion misidentification corrections. The first error shown is statistical while the second is systematic.*

PION PAIRS IN PAIR ANALYSIS EVENTS ($N_\pi \geq 3$) COULOMB AND PION MISIDENTIFICATION CORRECTIONS FIT TO: $R = \gamma(1+\delta Q^2)(1+\alpha\exp(-r^2Q^2))$				
parameter	SPEAR J/ψ	SPEAR $q\bar{q}$	PEP $\gamma\gamma$	PEP $q\bar{q}$
REFERENCE SAMPLE: UNLIKE CHARGED PAIRS				
α	$1.00 \pm 0.03 \pm 0.05$	$0.66 \pm 0.04 \pm 0.04$	$0.87 \pm 0.07 \pm 0.05$	$0.50 \pm 0.04 \pm 0.03$
r (fm)	$0.81 \pm 0.02 \pm 0.03$	$0.71 \pm 0.04 \pm 0.03$	$0.84 \pm 0.05 \pm 0.03$	$0.84 \pm 0.06 \pm 0.03$
δ (GeV^{-2})	$0.02 \pm 0.02 \pm 0.01$	$0.03 \pm 0.03 \pm 0.01$	$-0.07 \pm 0.04 \pm 0.01$	$0.23 \pm 0.03 \pm 0.02$
γ	$0.98 \pm 0.01 \pm 0.01$	$0.97 \pm 0.02 \pm 0.01$	$1.02 \pm 0.03 \pm 0.02$	$0.94 \pm 0.02 \pm 0.01$
χ^2/DOF	55/53	69/53	57/53	118/53
REFERENCE SAMPLE: MIXED CLUSTER PAIRS				
α	$0.94 \pm 0.03 \pm 0.05$	$0.72 \pm 0.03 \pm 0.04$	$1.21 \pm 0.07 \pm 0.07$	$0.45 \pm 0.05 \pm 0.03$
r (fm)	$0.72 \pm 0.02 \pm 0.03$	$0.74 \pm 0.03 \pm 0.03$	$1.01 \pm 0.04 \pm 0.04$	$1.02 \pm 0.09 \pm 0.04$
δ (GeV^{-2})	$0.31 \pm 0.03 \pm 0.02$	$-0.03 \pm 0.03 \pm 0.01$	$0.09 \pm 0.04 \pm 0.01$	$0.18 \pm 0.02 \pm 0.01$
γ	$0.89 \pm 0.01 \pm 0.01$	$0.98 \pm 0.01 \pm 0.01$	$0.97 \pm 0.02 \pm 0.01$	$0.96 \pm 0.01 \pm 0.01$
χ^2/DOF	192/95	110/95	132/95	213/95

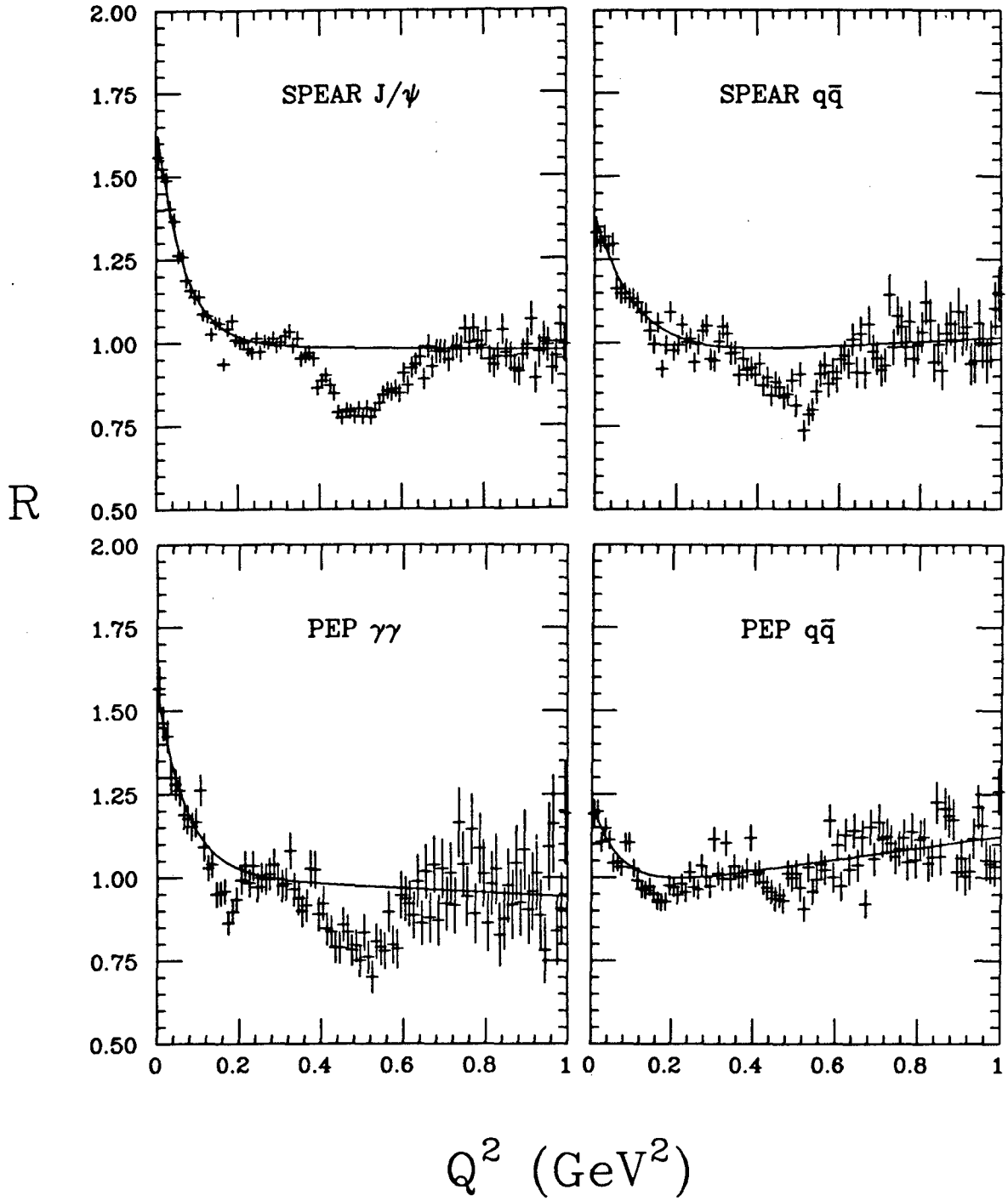

Figure 6.1 PION PAIRS IN PAIR EVENTS (N_π>3)
NO CORRECTIONS
REFERENCE SAMPLE: UNLIKE CHARGED PAIRS

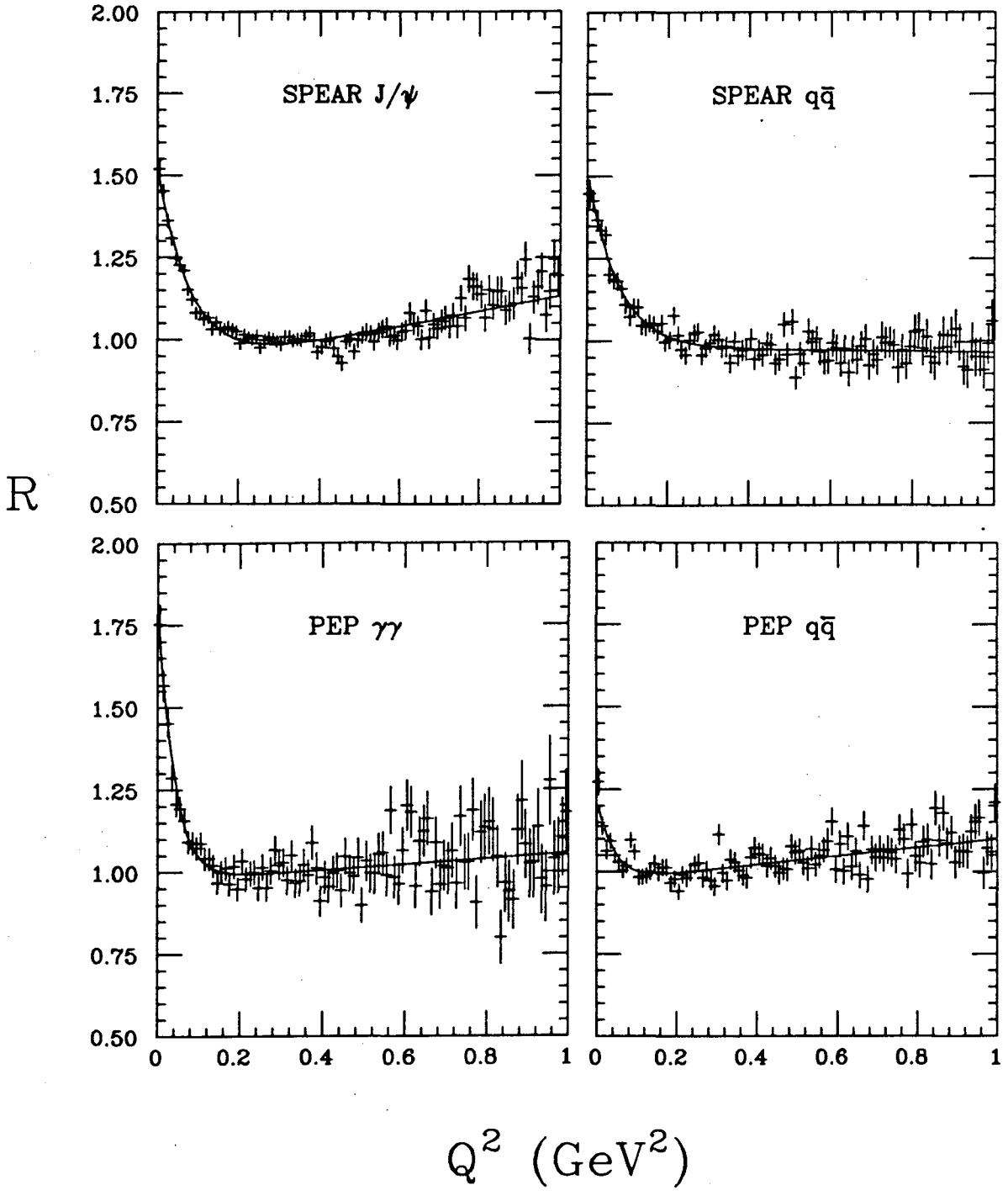

Figure 6.2 PION PAIRS IN PAIR EVENTS (N_π>3)
NO CORRECTIONS
REFERENCE SAMPLE: MIXED CLUSTER PAIRS

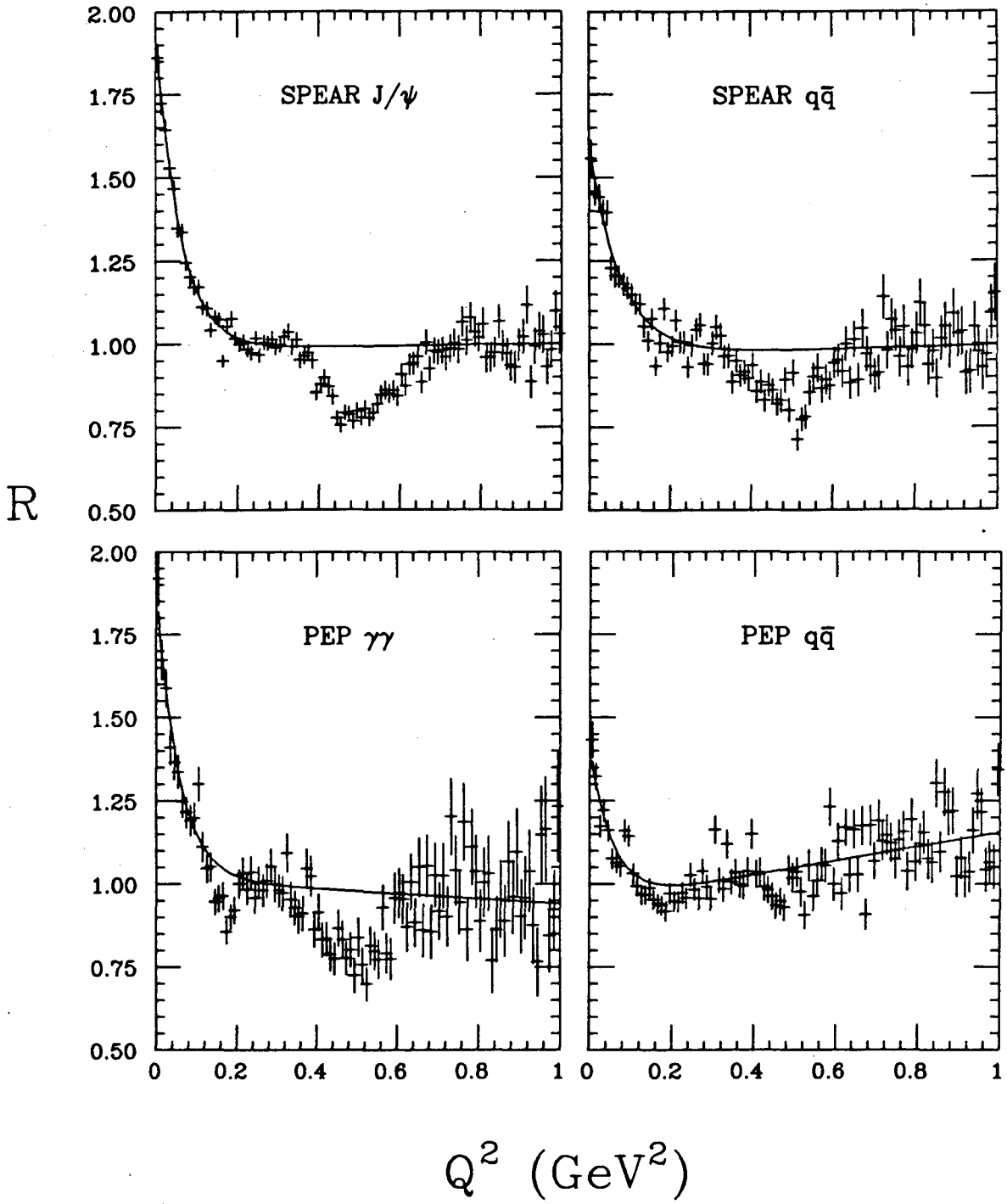

Figure 6.3 PION PAIRS IN PAIR EVENTS (N_π>3)
COULOMB AND PION MISIDENTIFICATION CORRECTIONS
REFERENCE SAMPLE: UNLIKE CHARGED PAIRS

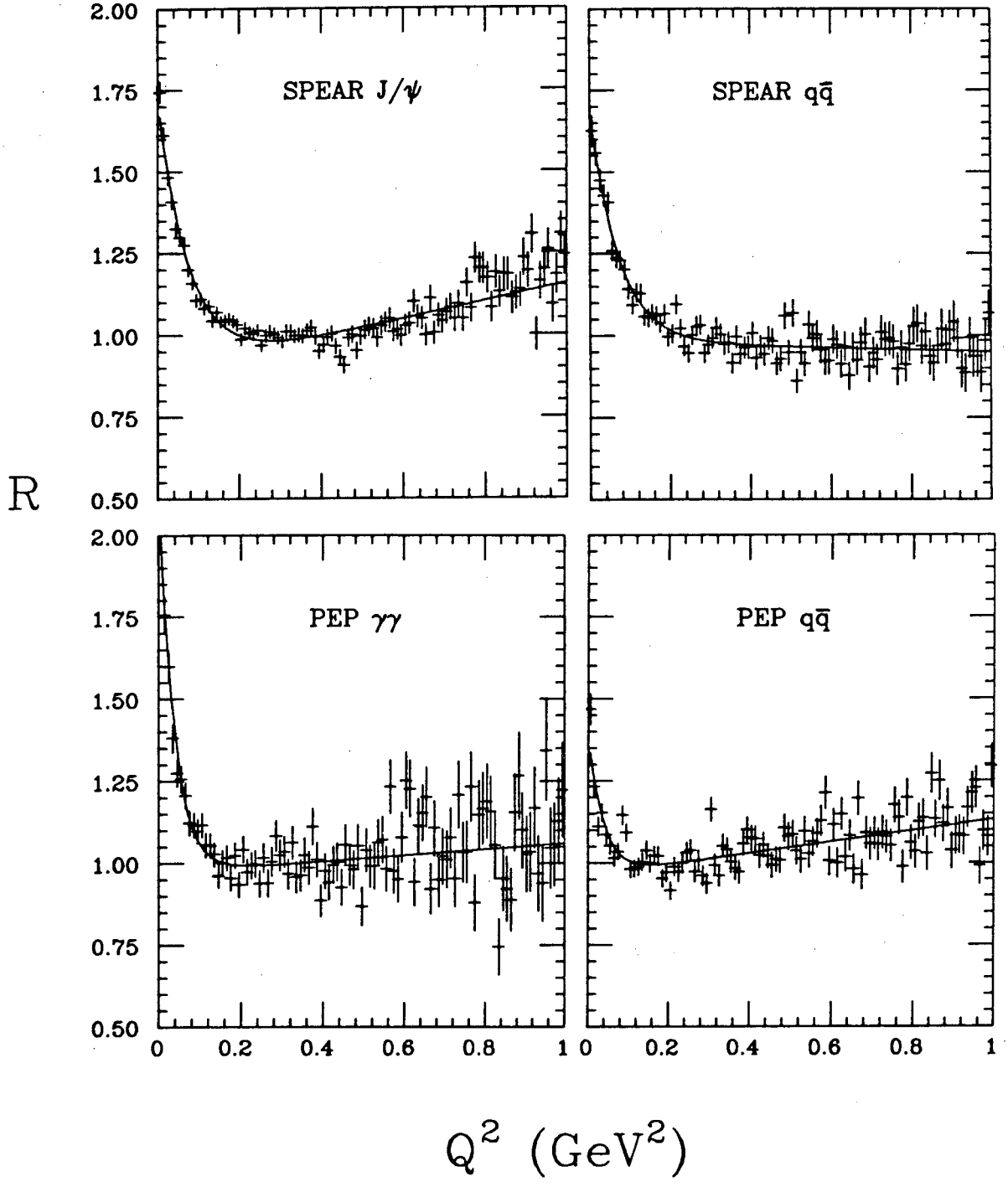

Figure 6.4 PION PAIRS IN PAIR EVENTS (N_π>3)
COULOMB AND PION MISIDENTIFICATION CORRECTIONS
REFERENCE SAMPLE: MIXED CLUSTER PAIRS

6.1.2 *Parameter γ Using Unlike Charged Pairs*

The number of like charged pairs is typically about two thirds to three quarters of the number of unlike charged pairs. This ratio, measured by γ, is a combinatorial function of the charged pion multiplicity distributions in the four data sets. In the tables of results and in the figures shown here, γ is close to 1.00 because we have chosen to insert a pre-normalization factor for each ratio before fitting. This is done in order to make it easier to compare visually the R distributions of various data sets. The pre-normalization factor is calculated using the normalization regions described in sections 4.6.1 and 5.2.3 for pairs and triplets, respectively. The fit to R was done with and without this pre-normalization (expressions (2) and (1) in Table 6.1, respectively), and only the value of γ was affected, as expected.

6.1.3 *Parameter α Using Unlike Charged Pairs*

The major result of this analysis is that the SPEAR J/ψ and PEP $\gamma\gamma$ data sets show a significantly higher value of α than the SPEAR $q\bar{q}$ and PEP $q\bar{q}$ data sets. In section 1.4.1 we discussed how the comparison of the hadronization processes in the four data sets leads us to expect this result.

With or without corrections, the values of α for the SPEAR J/ψ and PEP $\gamma\gamma$ data sets are nearly equal to each other within errors. Once the pion misidentification correction is applied, the values of α for the SPEAR $q\bar{q}$ and PEP $q\bar{q}$ data sets are also nearly equal to each other within errors. The pion misidentification correction is important in the latter case, because the pion misidentification in the PEP $q\bar{q}$ data set is significantly worse than the ones for the SPEAR J/ψ, SPEAR $q\bar{q}$, and PEP $\gamma\gamma$ data sets.

Recall that for the PEP $q\bar{q}$ data set we can form the ratio R/R_{mc}, using the MC PEP $q\bar{q}$ data in the denominator. As we saw in Fig. 4.9, taking this ratio removes evidence of resonances introduced by the unlike charged pion pairs. If we take the uncorrected R distribution from the PEP $q\bar{q}$ data, divide it by R_{mc}, and fit R/R_{mc}, we get $\alpha = 0.28 \pm 0.07 \pm 0.02$ and $r = (0.84 \pm 0.17 \pm 0.03)\ fm$. These values are within error of the fit results of R alone, listed in Table 6.2. R_{mc} is not a corrected ratio, since neither correction we apply to PEP $q\bar{q}$ data is necessary in Monte Carlo data: Coulomb final state effects are not simulated in the Monte

Carlo, and the pion misidentification correction is a multiplicative factor for both the like and unlike charged pairs.

After all corrections, the values of α for the SPEAR J/ψ and PEP $\gamma\gamma$ data sets are close to the maximum expected value of α, indicating nearly full chaoticity. The fully corrected values of α for the SPEAR $q\bar{q}$ and PEP $q\bar{q}$ data sets indicate only about half of the maximum expected value.

6.1.4 Parameter r Using Unlike Charged Pairs

For the pair analysis done using the unlike charged pair reference sample, two trends stand out clearly in the behavior of the parameter r. First, the value of r is the same within errors for all four data sets. Second, the value of r is the same within errors before and after all corrections. Thus we measure a fairly constant value for r of about 0.75 fm to 0.85 fm for all data sets.

6.1.5 Parameter δ Using Unlike Charged Pairs

Using the unlike charged pair reference sample, the value of the parameter δ is within error of zero in the SPEAR J/ψ, SPEAR $q\bar{q}$, and PEP $\gamma\gamma$ data. Thus we see no strong long range correlations within the fitting region in these data sets. The same measurement of δ in the PEP $q\bar{q}$ data set reflects the non-negligible long range correlations in this data discussed in section 4.5.1.

Note that the values of δ are nearly independent of the corrections applied.

6.1.6 Results Using the Mixed Cluster Reference Sample

We begin this section by discussing some performance tests of the mixed cluster reference sample. The goal is to ensure that the cluster mixing algorithm does not introduce any artificial correlations into the reference sample. In order to test this, we take the MC PEP $q\bar{q}$ data set and form ratios of like to unlike charged pairs, mixed cluster to unlike pairs, and like to mixed cluster pairs. Since Monte Carlo does not simulate the Bose-Einstein enhancement, we expect these ratios to be alike and flat near $Q^2 = 0$. Indeed, we find the fit values to be (statistical errors only):

1. for the ratio of like to unlike charged pairs in the MC PEP $q\bar{q}$ data set,

$$\alpha = -0.12 \pm 0.13, \quad r = 0.38 \pm 0.31, \quad \delta = 0.07 \pm 0.16;$$

2. for the ratio of mixed cluster to unlike charged pairs in the MC PEP $q\bar{q}$ data set,

$$\alpha = -0.12 \pm 0.03, \quad r = 0.82 \pm 1.00, \quad \delta = 0.02 \pm 0.01;$$

2. and for the ratio of like to mixed cluster pairs in the MC PEP $q\bar{q}$ data set,

$$\alpha = -0.01 \pm 0.14, \quad r = 0.30 \pm 1.16, \quad \delta = 0.10 \pm 0.16.$$

These numbers show that, aside from some difficulty in fitting a nearly flat ratio to an exponential, the fitting routine finds the ratios to be very much alike and close to flat within errors. A visual inspection of the three distributions confirms this result. This test indicates that, overall, the mixed cluster reference sample is a good reference sample, because it reproduces the unlike charged pair kinematical phase space without the presence of the K^0 and ρ^0 resonances. This leads us to expect that the mixed cluster reference sample will give us approximately the same results in pair analysis as the unlike charged pair reference sample. Note that this is merely a test of the mixed cluster algorithm, whose full usefulness becomes apparent in the analysis of pion triplets.

To see qualitatively how well the mixed reference sample reproduces the results obtained with unlike pairs in the actual data, we compare visually Fig. 6.2 with Fig. 6.1 and Fig. 6.4 with Fig. 6.3. The K^0 and ρ^0 resonances evident in the ratio of like to unlike pairs are absent as expected in the ratio of like to mixed cluster pairs. The mixed cluster pairs reproduce the distribution of unlike pairs

at large Q^2 fairly well for all data sets except the SPEAR J/ψ data set. This discrepancy is evident in the δ parameter of the fits. Recall that δ is a measure of long range correlations in the data. It measures the slope in the ratio of study sample to reference sample. If the δ measured using the mixed cluster reference sample is significantly different from the δ found using the unlike charged reference sample, then the mixed cluster reference sample is not reproducing the kinematical phase space of unlike charged pairs very well. We find that δ in SPEAR $q\bar{q}$, PEP $\gamma\gamma$, and PEP $q\bar{q}$ data sets measured using the mixed cluster reference sample is the same within errors as the δ found using the unlike charged pairs. Therefore, in these data sets the mixed cluster reference sample performs satisfactorily. In the case of the SPEAR J/ψ data, the mixed cluster reference sample finds a somewhat higher value of δ than that given by the unlike charged pairs. In this data, the mixed cluster reference sample is not as good an idealization of the unlike charged pairs for large Q^2 as it is in the other three data sets. This shortcoming does not appear to affect the parameters of interest, since we get nearly the same fitted values of α and r with the mixed cluster pairs as we do with the unlike charged pairs. The fit to the ratio of like to mixed cluster pairs for SPEAR J/ψ data also has a fairly high χ^2 per degree of freedom. From Fig. 6.4 we can see that this is due to the fact that our chosen fitting expression, which does well for the other data sets, does not fit the data precisely in this case.

Looking at Table 6.2 and Table 6.3, we indeed find that in the case of SPEAR J/ψ, SPEAR $q\bar{q}$, and PEP $q\bar{q}$ data, the mixed cluster reference sample tends to give the same values of α as the unlike charged pair reference sample. The PEP $\gamma\gamma$ data shows a slightly higher value of α with the mixed cluster reference sample.

The mixed cluster reference sample gives about the same value of r in the SPEAR J/ψ and SPEAR $q\bar{q}$ data sets as the r found using the unlike charged pair reference sample. In addition, r in the SPEAR J/ψ data set is nearly equal to r in the SPEAR $q\bar{q}$ data set and is independent of corrections applied. The value of r in the PEP $\gamma\gamma$ and PEP $q\bar{q}$ data sets given by the mixed cluster reference sample is significantly higher than the r given by the unlike charged pair reference sample.

However, the mixed cluster reference sample gives the same r in both the PEP $\gamma\gamma$ data and the PEP $q\bar{q}$ data, independent of corrections applied.

6.2 GGLP Effect in Pion Triplets

6.2.1 Calculation and Fitting of the Triplet Correlation Function

We correct individual study sample and reference sample distributions for Coulomb effects using the appropriate Gamow factors (section 5.2.2). These Coulomb corrected distributions are then corrected for pion misidentification (section 5.2.3), and their ratio $R_{3\pi}$ is fitted to a slightly modified form of Eqn. 5.2:

$$R_{3\pi} = \gamma\ (1 + \alpha_{3\pi}\ e^{-r_{3\pi}^2 Q_{3\pi}^2}),$$

where γ normalizes the relative numbers of study sample and reference sample triplets. As in the analysis of pion pairs, all the fits are done with the utility minimization routine MINUIT used in pair analysis fitting. The fit to $R_{3\pi}$ is done over

$$0.01\ GeV^2 < Q_{3\pi}^2 < 1.00\ GeV^2,$$

both for the $\pm\pm\mp$ reference sample and for the mixed cluster reference sample.

The results of the fits for the triplet study sample are shown in Table 6.4 and Table 6.5 for no corrections and all corrections, respectively. The corresponding distributions and fitted curves are shown in Fig. 6.5, Fig. 6.6, Fig. 6.7, and Fig. 6.8.

As in the case of pairs, we show triplet ratios which have been pre-normalized (section 5.2.3) to make visual comparisons easier. The pre-normalization affects only the fitted value of γ, which after pre-normalization is close to 1.00.

6.2.2 Mixed Cluster Reference Sample in Triplet Analysis

In this section we discuss an obvious consistency check of the mixed cluster algorithm in triplet analysis. We take the $\pm\pm\mp$ triplet reference sample and divide it by the mixed cluster reference sample. The ratio of these uncorrected

Table 6.4 *Fit results for the pion triplet study sample with no corrections. The first error shown is statistical while the second is systematic.*

PION TRIPLETS IN TRIPLET ANALYSIS EVENTS ($N_\pi \geq 5$) NO CORRECTIONS FIT TO: $R_{3\pi} = \gamma(1 + \alpha_{3\pi}\exp(-r_{3\pi}^2 Q_{3\pi}^2))$				
parameter	SPEAR J/ψ	SPEAR $q\bar{q}$	PEP $\gamma\gamma$	PEP $q\bar{q}$
REFERENCE SAMPLE: $\pm\pm\mp$ TRIPLETS (contains correlation in one like pair)				
$\alpha_{3\pi}$	$2.46 \pm 0.17 \pm 0.30$	$1.12 \pm 0.12 \pm 0.13$	$1.61 \pm 0.42 \pm 0.19$	$0.86 \pm 0.17 \pm 0.12$
$r_{3\pi}$ (fm)	$0.47 \pm 0.02 \pm 0.02$	$0.41 \pm 0.03 \pm 0.02$	$0.51 \pm 0.05 \pm 0.02$	$0.66 \pm 0.04 \pm 0.03$
γ	$0.95 \pm 0.01 \pm 0.01$	$0.94 \pm 0.02 \pm 0.01$	$0.97 \pm 0.02 \pm 0.01$	$0.99 \pm 0.01 \pm 0.01$
χ^2/DOF	99/95	106/95	112/95	86/95
REFERENCE SAMPLE: MIXED CLUSTER TRIPLETS				
$\alpha_{3\pi}$	$3.37 \pm 0.24 \pm 0.40$	$1.69 \pm 0.16 \pm 0.20$	$2.94 \pm 0.63 \pm 0.35$	$0.83 \pm 0.16 \pm 0.10$
$r_{3\pi}$ (fm)	$0.53 \pm 0.01 \pm 0.02$	$0.44 \pm 0.02 \pm 0.02$	$0.54 \pm 0.04 \pm 0.02$	$0.66 \pm 0.04 \pm 0.03$
γ	$0.97 \pm 0.01 \pm 0.01$	$0.95 \pm 0.02 \pm 0.01$	$0.97 \pm 0.02 \pm 0.01$	$0.99 \pm 0.01 \pm 0.01$
χ^2/DOF	92/95	94/95	119/95	90/95

distributions in $Q_{3\pi}^2$ is expected to exhibit a Bose-Einstein enhancement due to the one like charged pair present in the $\pm\pm\mp$ reference sample.

When we attempt to fit the ratio of $\pm\pm\mp$ to mixed cluster pairs, we run into the problem of low triplet statistics in the bins close to $Q_{3\pi}^2 = 0$. The largest data

Table 6.5 *Fit results for the pion triplet study sample with both Coulomb and pion misidentification corrections. The first error shown is statistical while the second is systematic.*

PION TRIPLETS IN TRIPLET ANALYSIS EVENTS ($N_\pi \geq 5$) COULOMB AND PION MISIDENTIFICATION CORRECTIONS FIT TO: $R_{3\pi} = \gamma(1 + \alpha_{3\pi} \exp(-r_{3\pi}^2 Q_{3\pi}^2))$				
parameter	SPEAR J/ψ	SPEAR $q\bar{q}$	PEP $\gamma\gamma$	PEP $q\bar{q}$
REFERENCE SAMPLE: $\pm\pm\mp$ TRIPLETS (contains correlation in one like pair)				
$\alpha_{3\pi}$	$3.80 \pm 0.23 \pm 0.46$	$1.83 \pm 0.16 \pm 0.22$	$2.58 \pm 0.36 \pm 0.31$	$1.60 \pm 0.21 \pm 0.19$
$r_{3\pi}$ (fm)	$0.48 \pm 0.01 \pm 0.02$	$0.42 \pm 0.02 \pm 0.02$	$0.47 \pm 0.03 \pm 0.02$	$0.64 \pm 0.03 \pm 0.03$
γ	$0.93 \pm 0.02 \pm 0.01$	$0.92 \pm 0.02 \pm 0.01$	$0.91 \pm 0.03 \pm 0.01$	$0.99 \pm 0.01 \pm 0.01$
χ^2/DOF	138/95	147/95	163/95	140/95
REFERENCE SAMPLE: MIXED CLUSTER TRIPLETS				
$\alpha_{3\pi}$	$4.92 \pm 0.31 \pm 0.59$	$2.57 \pm 0.22 \pm 0.31$	$4.40 \pm 0.88 \pm 0.53$	$1.54 \pm 0.20 \pm 0.18$
$r_{3\pi}$ (fm)	$0.53 \pm 0.01 \pm 0.02$	$0.45 \pm 0.02 \pm 0.02$	$0.54 \pm 0.03 \pm 0.02$	$0.64 \pm 0.03 \pm 0.03$
γ	$0.95 \pm 0.01 \pm 0.01$	$0.92 \pm 0.02 \pm 0.01$	$0.94 \pm 0.02 \pm 0.01$	$0.99 \pm 0.01 \pm 0.01$
χ^2/DOF	130/95	133/95	166/95	134/95

set, SPEAR J/ψ data, is the only one where we can make a statistically significant fit to this ratio. We find

$$\alpha = 0.53 \pm 0.15, \quad r = 0.77 \pm 0.07 \ fm.$$

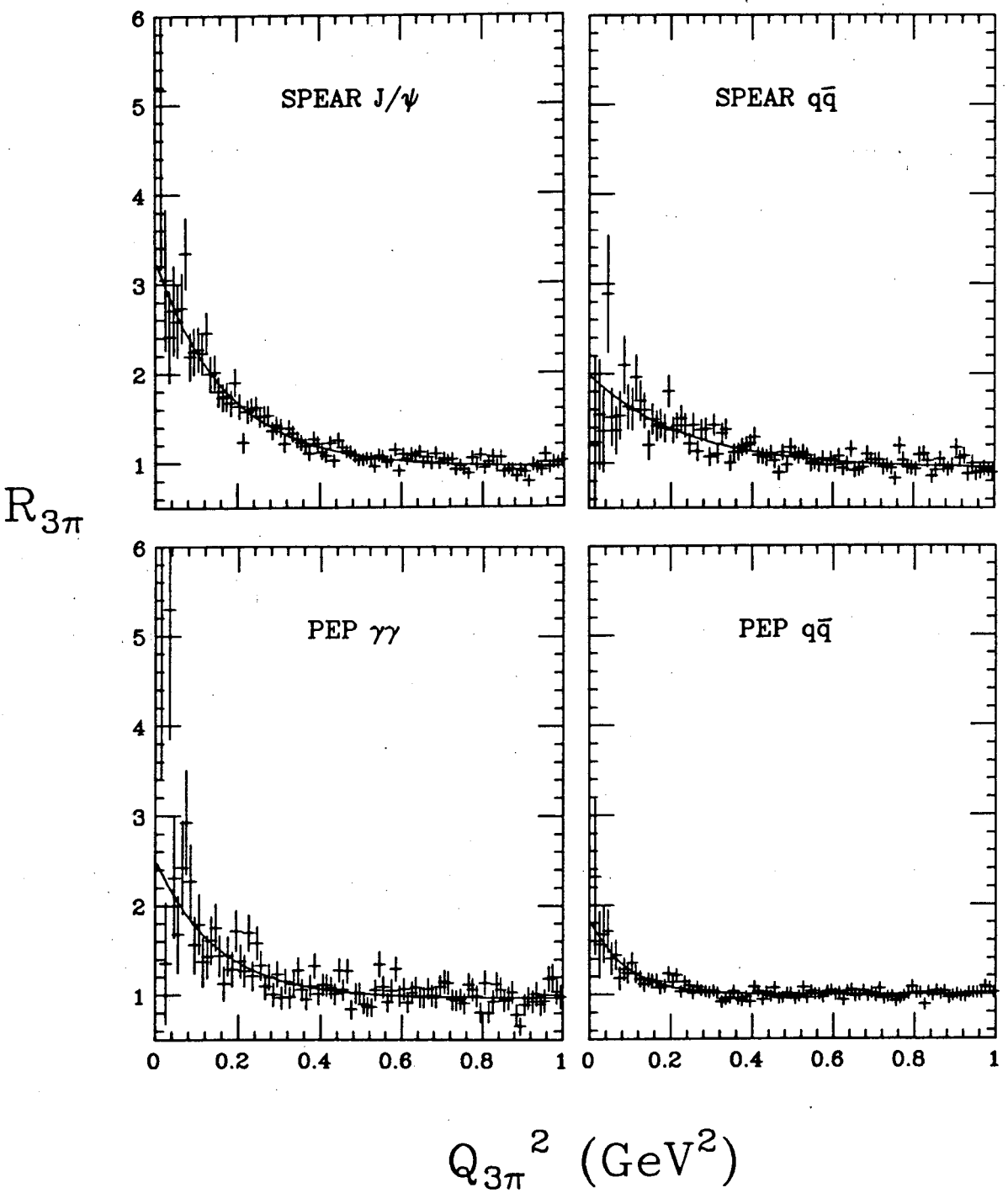

Figure 6.5 PION TRIPLETS IN TRIPLET EVENTS (N_π>5)
NO CORRECTIONS
REFERENCE SAMPLE: $\pm\pm\mp$ TRIPLETS

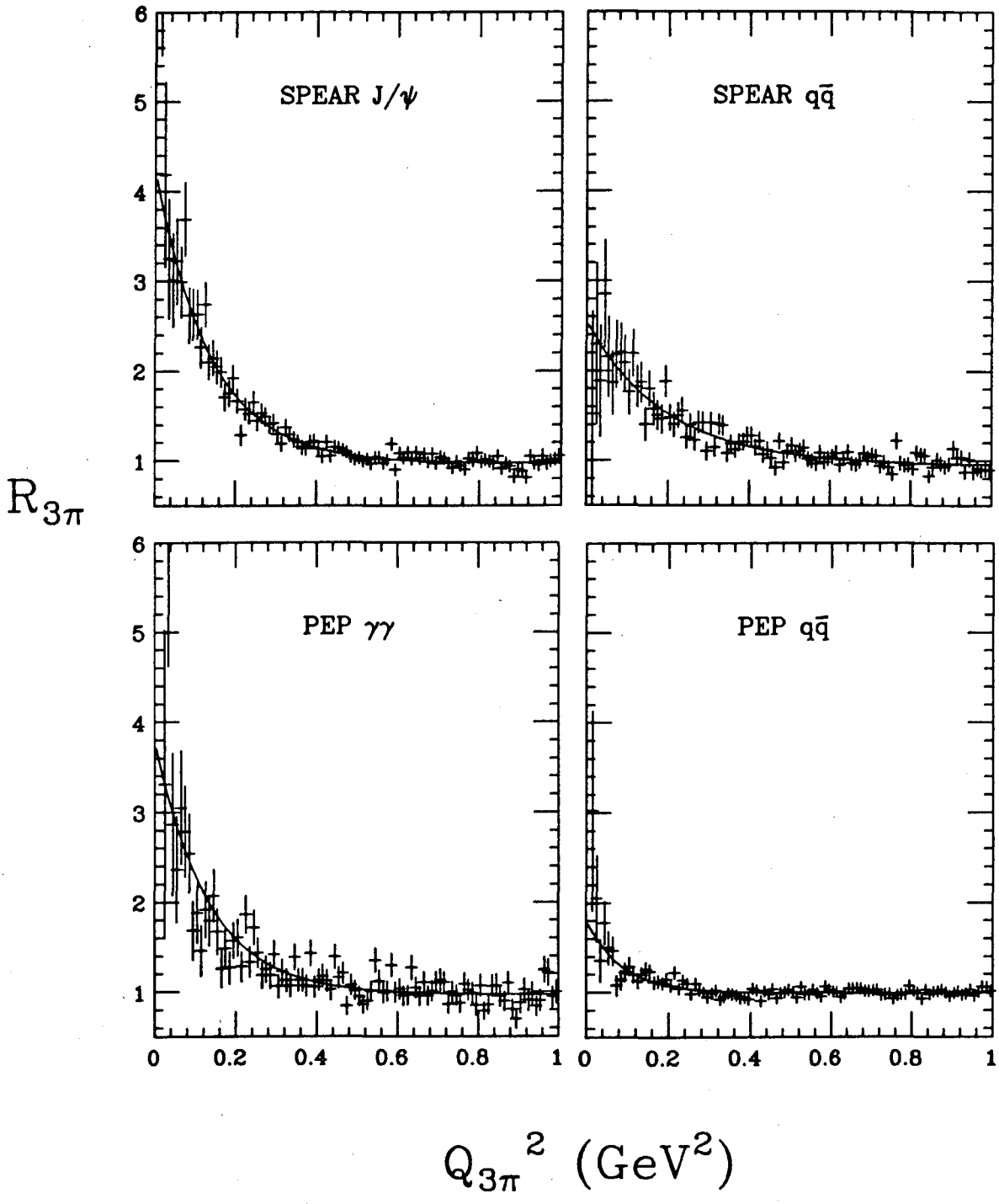

Figure 6.6 PION TRIPLETS IN TRIPLET EVENTS (N_π>5)
NO CORRECTIONS
REFERENCE SAMPLE: MIXED CLUSTER TRIPLETS

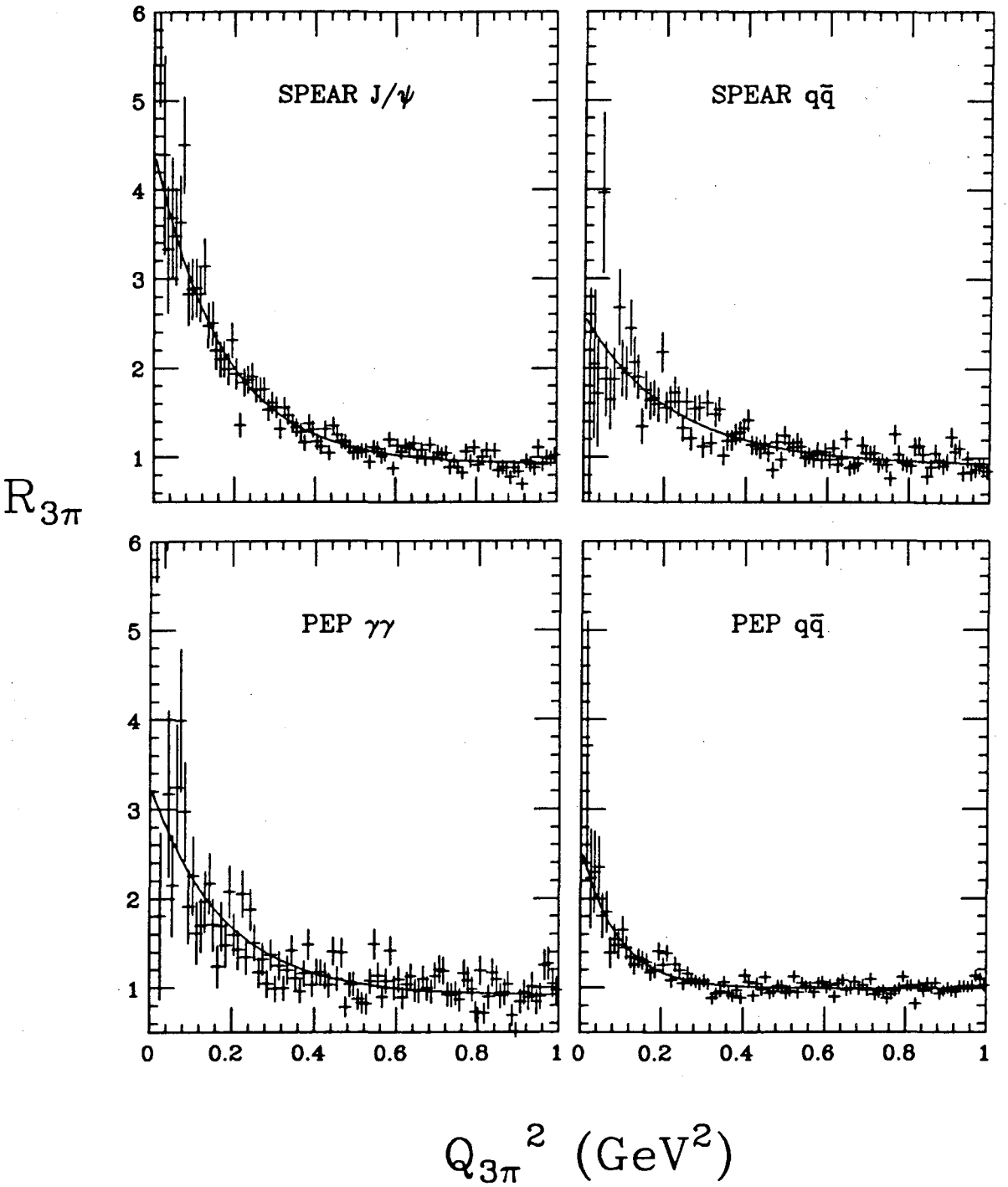

Figure 6.7 PION TRIPLETS IN TRIPLET EVENTS (N_π>5)
COULOMB AND PION MISIDENTIFICATION CORRECTIONS
REFERENCE SAMPLE: $\pm\pm_\mp$ TRIPLETS

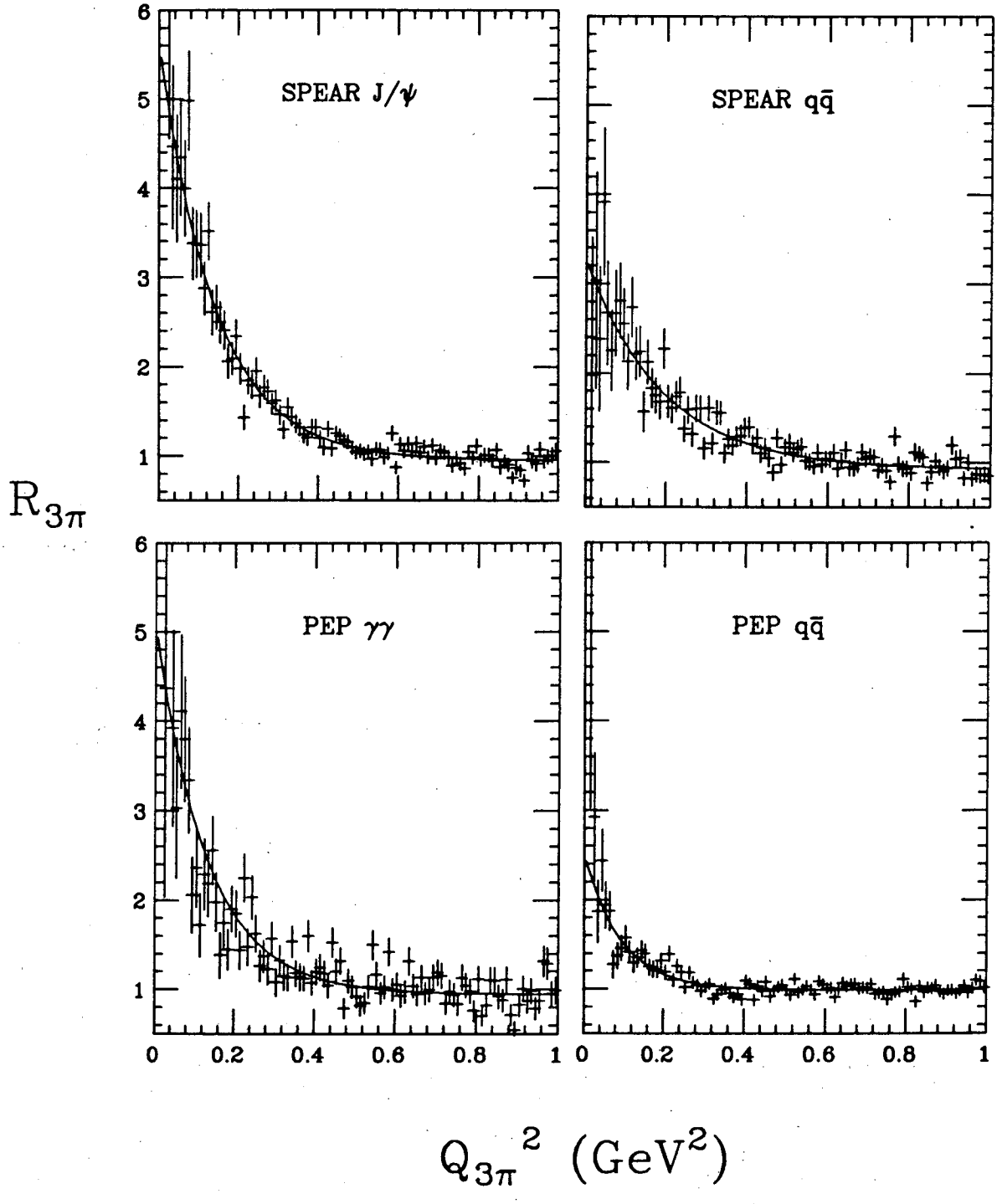

Figure 6.8 PION TRIPLETS IN TRIPLET EVENTS (N_π>5)
COULOMB AND PION MISIDENTIFICATION CORRECTIONS
REFERENCE SAMPLE: MIXED CLUSTER TRIPLETS

This fit and the unfitted ratios for the other three data sets are shown in Fig. 6.9 Although we can fit only the SPEAR J/ψ data set, all four data sets show indications of some enhancement near $Q^2_{3\pi}$. This is consistent with the expectation that the mixed cluster reference sample behaves like a triplet of non-identical pions.

6.2.3 Parameters $\alpha_{3\pi}$ and $r_{3\pi}$

The fitted values of $\alpha_{3\pi}$ and $r_{3\pi}$ follow the same general patterns as α and r do for pairs.

As we discussed in 5.2.1, the $\pm\pm\mp$ reference sample contains one like charged pair, so it is not surprising that $\alpha_{3\pi}$ found using this reference sample is less than the maximum expected value of 5.00. However, the same reference sample shows that the SPEAR J/ψ and PEP $\gamma\gamma$ data sets have higher values of $\alpha_{3\pi}$ than the other two data sets. The PEP $\gamma\gamma$ data set suffers from comparatively low statistics and thus has higher errors, but we can still see in triplets the same data set grouping we see in pairs: SPEAR J/ψ and PEP $\gamma\gamma$ data have similar values of $\alpha_{3\pi}$, while SPEAR $q\bar{q}$ and PEP $q\bar{q}$ data also have similar values of $\alpha_{3\pi}$ after applying the pion misidentification correction. Again, these are the overall features of the triplet analysis done with the $\pm\pm\mp$ reference sample.

Looking at the values of $\alpha_{3\pi}$ found using the mixed cluster reference sample, we see the same data groupings as described in the previous paragraph. This reference sample, however, contains no Bose-Einstein correlations, and after all corrections have been applied we measure close to maximum values of $\alpha_{3\pi}$ for the SPEAR J/ψ and PEP $\gamma\gamma$ data sets. The fully corrected fits of $\alpha_{3\pi}$ for the SPEAR $q\bar{q}$ and PEP $q\bar{q}$ data sets show about a half to a third of the maximum values. As in the case of the pair analysis, these results indicate nearly full chaoticity for the SPEAR J/ψ and PEP $\gamma\gamma$ data sets.

Both reference samples show values of $r_{3\pi}$ to be uniform over data sets and over corrections. Only the PEP $q\bar{q}$ data set has $r_{3\pi}$ slightly higher than the other three. The values of $r_{3\pi}$ found using the $\pm\pm\mp$ reference sample are within errors of $r_{3\pi}$ measured with the mixed cluster reference sample, so this parameter is also

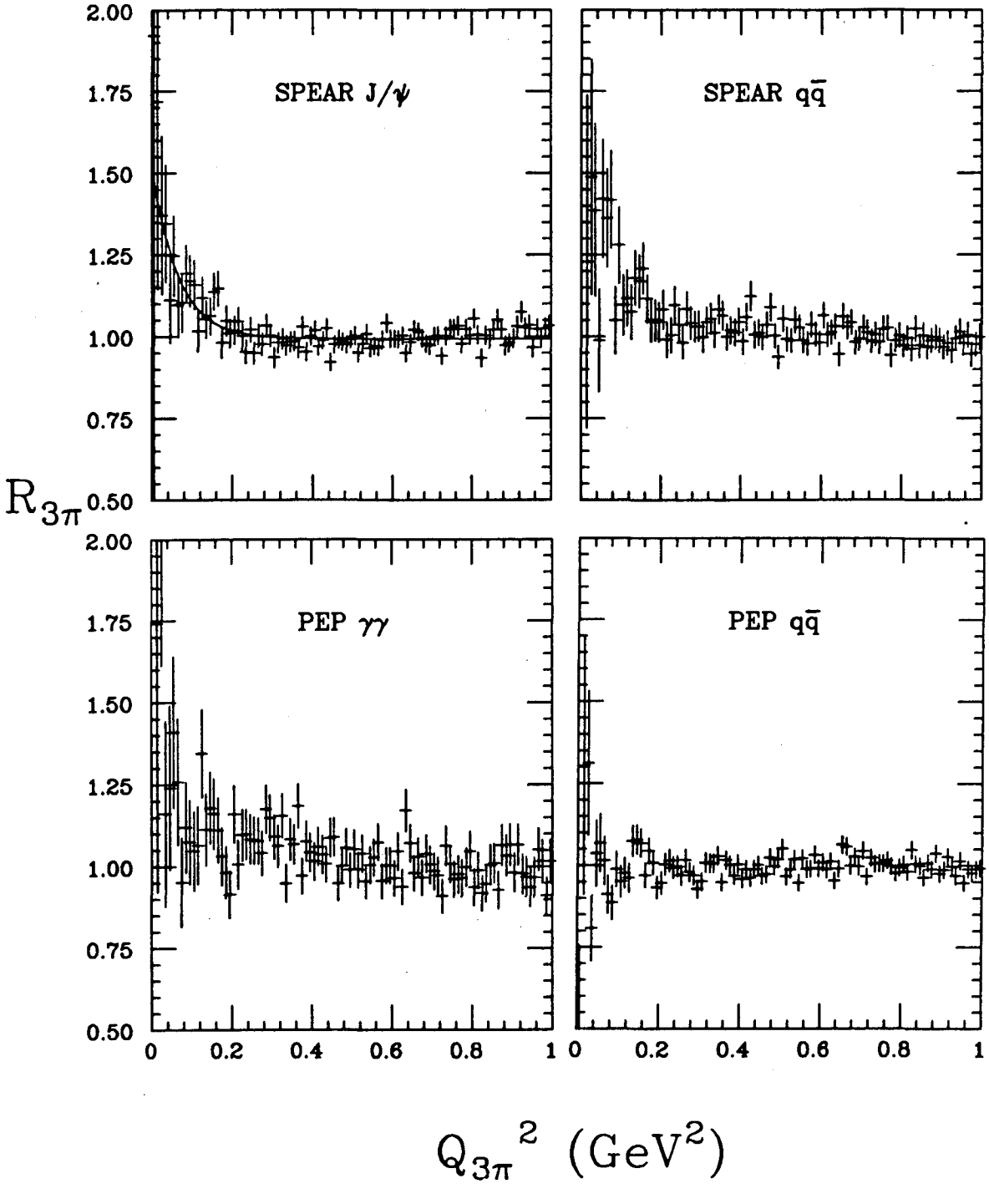

Figure 6.9 *Ratios in $Q^2_{3\pi}$ of $\pm\pm\mp$ triplets to mixed cluster triplets (no corrections), where we expect to see evidence of the Bose-Einstein enhancement in the single like pair within the $\pm\pm\mp$ triplet. Only the SPEAR J/ψ data has enough statistics to permit fitting this ratio. The other data sets suffer from low statistics but seem to indicate some enhancement near $Q^2_{3\pi} = 0$.*

independent of the reference sample used.

6.2.4 *Comparison of Triplets and Pairs*

We will now calculate the purely triplet Bose-Einstein enhancement μ described in section 5.1.2 using the measured values of the enhancement in triplets and in pairs.

The pion pairs we use in this calculation must of course come from the same events used in the triplet analysis. Recall that the pion multiplicity requirement for pair analysis events is $N_\pi \geq 3$, while the requirement for triplet analysis events is $N_\pi \geq 5$. In Table 6.6 we show the pion misidentification fractions for pairs in triplet analysis events. These values differ slightly from Table 4.5 because the pion multiplicity requirements make the average pion momentum in a triplet analysis event lower than the one in a pair analysis event. A lower average momentum means a better average pion identification efficiency (see section 4.6.1). Using these misidentification fractions, we form pair distribution ratios (for pairs in triplet events) with no corrections and with both coulomb and pion misidentification corrections. The results of the fits to these ratios are shown in Table 6.7 and Table 6.8.

Table 6.6 *Pion misidentification fractions for pion pairs in triplet analysis events.*

Monte Carlo Data Set	$T_{\pi\pi} \equiv \left\langle \frac{\pi_t \pi_t}{\pi\pi} \right\rangle$
MC SPEAR J/ψ	0.88
MC SPEAR $q\bar{q}$	0.88
MC PEP $\gamma\gamma$	0.82
MC PEP $q\bar{q}$	0.72

Note that before any corrections, pion pairs in pair analysis events have significantly lower values of α than pion pairs in triplet analysis events, but this difference disappears after the pion misidentification correction is applied.

Table 6.7 *Fit results for pion pairs in triplet events with no corrections. The first error shown is statistical while the second is systematic.*

PION PAIRS IN TRIPLET ANALYSIS EVENTS ($N_\pi \geq 5$) NO CORRECTIONS FIT TO: $R = \gamma(1+\delta Q^2)(1+\alpha\exp(-r^2Q^2))$				
parameter	SPEAR J/ψ	SPEAR $q\bar{q}$	PEP $\gamma\gamma$	PEP $q\bar{q}$
REFERENCE SAMPLE: UNLIKE CHARGED PAIRS				
α	$0.79 \pm 0.04 \pm 0.04$	$0.60 \pm 0.12 \pm 0.03$	$0.56 \pm 0.09 \pm 0.03$	$0.28 \pm 0.03 \pm 0.02$
r (fm)	$0.75 \pm 0.03 \pm 0.03$	$0.53 \pm 0.07 \pm 0.02$	$0.63 \pm 0.09 \pm 0.03$	$0.75 \pm 0.07 \pm 0.03$
δ (GeV^{-2})	$-0.02 \pm 0.03 \pm 0.01$	$0.21 \pm 0.12 \pm 0.02$	$-0.06 \pm 0.09 \pm 0.01$	$0.18 \pm 0.03 \pm 0.01$
γ	$0.99 \pm 0.02 \pm 0.01$	$0.87 \pm 0.07 \pm 0.01$	$0.98 \pm 0.06 \pm 0.01$	$0.95 \pm 0.02 \pm 0.01$
χ^2/DOF	68/53	61/53	40/53	91/53
REFERENCE SAMPLE: MIXED CLUSTER PAIRS				
α	$0.89 \pm 0.04 \pm 0.04$	$0.58 \pm 0.04 \pm 0.03$	$0.74 \pm 0.07 \pm 0.05$	$0.26 \pm 0.04 \pm 0.02$
r (fm)	$0.72 \pm 0.03 \pm 0.03$	$0.75 \pm 0.04 \pm 0.03$	$0.92 \pm 0.07 \pm 0.04$	$0.99 \pm 0.12 \pm 0.04$
δ (GeV^{-2})	$0.69 \pm 0.07 \pm 0.02$	$0.06 \pm 0.03 \pm 0.01$	$0.07 \pm 0.05 \pm 0.01$	$0.13 \pm 0.02 \pm 0.01$
γ	$0.82 \pm 0.02 \pm 0.01$	$0.97 \pm 0.02 \pm 0.01$	$0.97 \pm 0.02 \pm 0.01$	$0.97 \pm 0.01 \pm 0.01$
χ^2/DOF	99/95	94/95	89/95	138/95

Table 6.8 *Fit results for pion pairs in triplet events with both Coulomb and pion misidentification corrections. The first error shown is statistical while the second is systematic.*

PION PAIRS IN TRIPLET ANALYSIS EVENTS ($N_\pi \geq 5$) COULOMB AND PION MISIDENTIFICATION CORRECTIONS FIT TO: $R = \gamma(1+\delta Q^2)(1+\alpha\exp(-r^2Q^2))$				
parameter	SPEAR J/ψ	SPEAR $q\bar{q}$	PEP $\gamma\gamma$	PEP $q\bar{q}$
REFERENCE SAMPLE: UNLIKE CHARGED PAIRS				
α	$1.08 \pm 0.05 \pm 0.06$	$0.69 \pm 0.06 \pm 0.04$	$0.80 \pm 0.09 \pm 0.04$	$0.49 \pm 0.04 \pm 0.03$
r (fm)	$0.79 \pm 0.03 \pm 0.03$	$0.62 \pm 0.05 \pm 0.03$	$0.73 \pm 0.07 \pm 0.03$	$0.84 \pm 0.06 \pm 0.03$
δ (GeV^{-2})	$0.05 \pm 0.04 \pm 0.01$	$0.14 \pm 0.07 \pm 0.01$	$-0.10 \pm 0.07 \pm 0.01$	$0.23 \pm 0.03 \pm 0.02$
γ	$0.97 \pm 0.02 \pm 0.01$	$0.91 \pm 0.04 \pm 0.01$	$1.01 \pm 0.04 \pm 0.02$	$0.94 \pm 0.02 \pm 0.01$
χ^2/DOF	67/53	63/53	45/53	120/53
REFERENCE SAMPLE: MIXED CLUSTER PAIRS				
α	$1.14 \pm 0.03 \pm 0.07$	$0.71 \pm 0.04 \pm 0.04$	$1.01 \pm 0.09 \pm 0.06$	$0.44 \pm 0.05 \pm 0.03$
r (fm)	$0.74 \pm 0.01 \pm 0.03$	$0.77 \pm 0.04 \pm 0.03$	$0.94 \pm 0.06 \pm 0.04$	$1.02 \pm 0.09 \pm 0.04$
δ (GeV^{-2})	$0.81 \pm 0.01 \pm 0.05$	$0.06 \pm 0.03 \pm 0.01$	$0.06 \pm 0.05 \pm 0.01$	$0.18 \pm 0.02 \pm 0.01$
γ	$0.80 \pm 0.01 \pm 0.01$	$0.97 \pm 0.02 \pm 0.01$	$0.97 \pm 0.02 \pm 0.01$	$0.96 \pm 0.01 \pm 0.01$
χ^2/DOF	121/95	110/95	118/95	213/95

The pure triplet contribution to the Bose-Einstein enhancement is calculated using the approximate relation derived in section 5.1.2,

$$\mu \approx \frac{1}{2}(\alpha_{3\pi} - 3\alpha),$$

and the results are shown in Table 6.9. The large errors in $\alpha_{3\pi}$, which are the result of low triplet statistics, make the errors in μ large compared to the values of μ found. If we ignore the errors for a moment, the SPEAR J/ψ and PEP $\gamma\gamma$ data do seem to have higher values of μ than SPEAR $q\bar{q}$ and PEP $q\bar{q}$ data. Qualitatively, therefore, μ favors the same pattern as we saw in α for pairs. However, within the given statistical and systematic errors, the values of μ in all four data sets are consistent with each other as well as with the conclusion that $\mu \approx 0$ in all four data sets.

Table 6.9 *Results of the calculation of the pure triplet contribution to the Bose-Einstein enhancement in triplets. The α listed here is for the pion pairs in triplet events (see text). All the values are for fully corrected ratios using the mixed cluster reference sample is used.*

Data Set	$\alpha_{3\pi}$	α	μ
SPEAR J/ψ	$4.92 \pm 0.31 \pm 0.59$	$1.14 \pm 0.03 \pm 0.07$	$0.75 \pm 0.31 \pm 0.59$
SPEAR $q\bar{q}$	$2.57 \pm 0.22 \pm 0.31$	$0.71 \pm 0.04 \pm 0.04$	$0.22 \pm 0.22 \pm 0.31$
PEP $\gamma\gamma$	$4.40 \pm 0.88 \pm 0.53$	$1.01 \pm 0.09 \pm 0.06$	$0.66 \pm 0.88 \pm 0.53$
PEP $q\bar{q}$	$1.54 \pm 0.20 \pm 0.18$	$0.44 \pm 0.05 \pm 0.03$	$0.11 \pm 0.21 \pm 0.18$

Next, we compare $r_{3\pi}$ in triplets with r in pairs. In section 5.1.2 we discussed why it is plausible to expect

$$r_{3\pi}^2 \approx \begin{cases} r^2/3 \\ \text{to} \\ r^2/2 \end{cases} .$$

Table 6.10. indeed shows that $r_{3\pi}$ for all four data sets is within these values. The SPEAR J/ψ data has a ratio of about 1/2, while the other three data sets are closer to 1/3.

Table 6.10 *Results of the comparison of $r_{3\pi}$ and r. The r listed here is for the pion pairs in triplet events (see text). All the values are for fully corrected ratios using the mixed cluster reference sample.*

Data Set	$r_{3\pi}$ (fm)	r (fm)	$r_{3\pi}^2/r^2$
SPEAR J/ψ	$0.53 \pm 0.01 \pm 0.02$	$0.74 \pm 0.01 \pm 0.03$	≈ 0.51
SPEAR $q\bar{q}$	$0.45 \pm 0.02 \pm 0.02$	$0.77 \pm 0.04 \pm 0.03$	≈ 0.34
PEP $\gamma\gamma$	$0.54 \pm 0.03 \pm 0.02$	$0.94 \pm 0.06 \pm 0.04$	≈ 0.33
PEP $q\bar{q}$	$0.64 \pm 0.03 \pm 0.03$	$1.02 \pm 0.09 \pm 0.04$	≈ 0.39

6.3 GGLP Effect in PEP $\gamma\gamma$ Data

Recall from section 1.4.1 that in PEP $\gamma\gamma$ data different hadronization mechanisms are expected to dominate in different regions of p_T, where p_T is the component of the net hadron three-momentum perpendicular with respect to the beam axis. The two photons annihilate directly into $q\bar{q}$ in the region of high p_T, while for low p_T they annihilate predominantly in their vector meson form (VDM).

Our goal in this section is to find out if the source parameters measured by the GGLP effect vary as a function of p_T. In other words, does the GGLP effect distinguish between the two hadronization processes in PEP $\gamma\gamma$ data? Instead of using p_T, the component of net hadronic three-momentum, we follow convention and use the highest single hadron track component in an event, p_{Tmax}. Figure 6.10 shows the distribution of p_{Tmax} in PEP $\gamma\gamma$ events. To maximize statistical significance, we choose three bins in p_{Tmax} with an approximately equal number of events in each bin. Then we form ratios of like to unlike charged pairs within each p_{Tmax} bin and fit these ratios as we fitted pairs in section 6.1.

The results of these fits are listed in Table 6.11. We see a clear decrease of α with p_{Tmax}. The corrected ratio shows full chaoticity within errors in the lowest p_{Tmax} bin. In the highest p_{Tmax} bin, the value of α approaches the value for the SPEAR $q\bar{q}$ and PEP $q\bar{q}$ data sets listed in Table 6.3. Thus the VDM hadronization process appears more chaotic than the high p_T process, and the latter is consistent

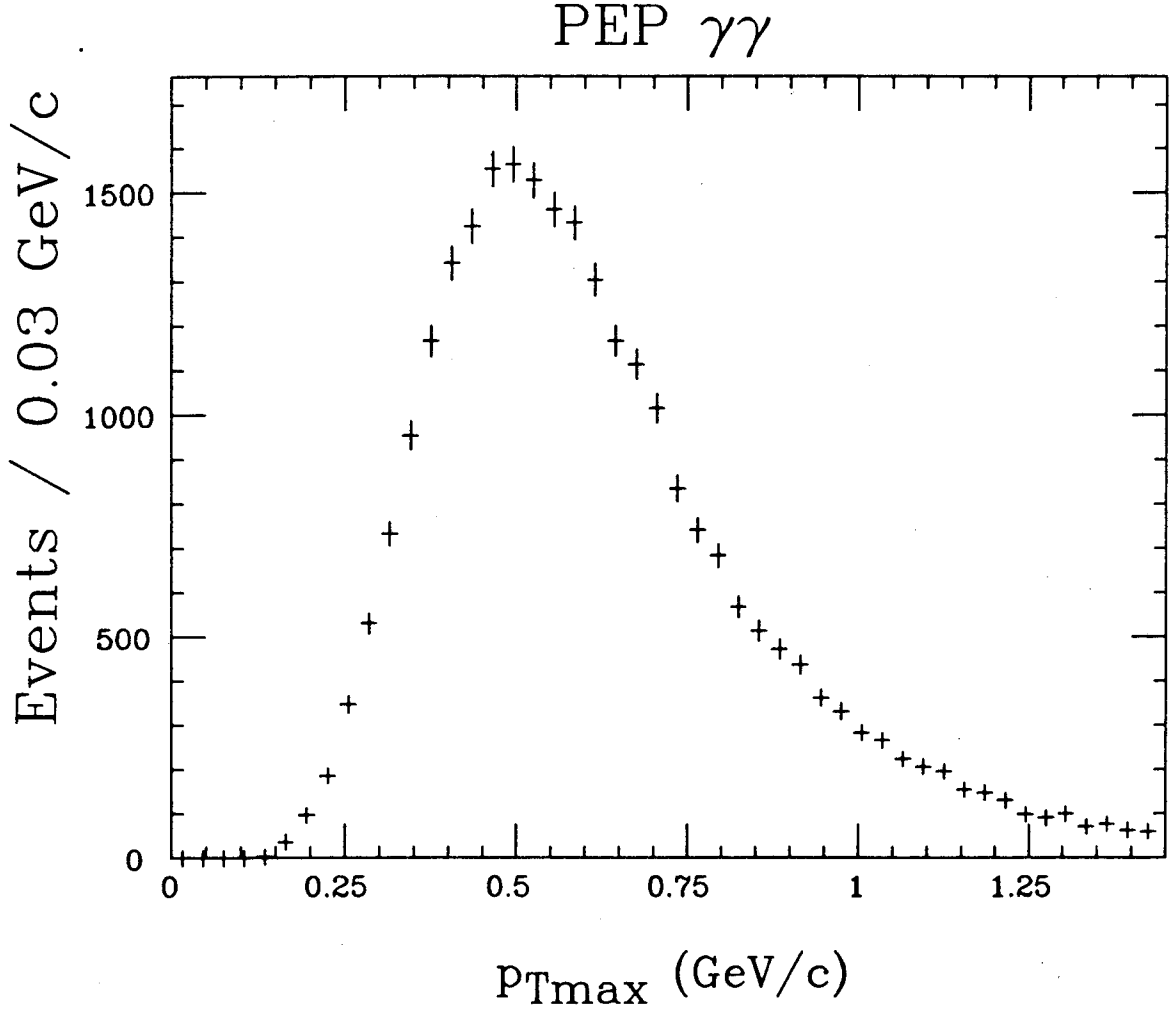

Figure 6.10 *Distribution of p_{Tmax} for PEP $\gamma\gamma$ data. p_{Tmax} is the highest single hadron track component in an event.*

with measurements done on other $q\bar{q}$ hadronization processes (SPEAR $q\bar{q}$ and PEP $q\bar{q}$ data). Within errors, the value of r is independent of p_{Tmax} and of corrections applied.

Table 6.11 *PEP $\gamma\gamma$ data is divided into three bins of p_{Tmax}, and the ratio of like to unlike charged pairs in each bin is fitted as in section 6.1.*

	p_{Tmax} (GeV/c)		
parameter	$0.0 - 0.5$	$0.5 - 0.7$	> 0.7
$N_{\pi\pm\pi\pm}/N_{\pi+\pi-}$	19,480/30,911	21,340/32,506	20,922/31,243
NO CORRECTIONS			
α	$0.72 \pm 0.07 \pm 0.04$	$0.61 \pm 0.08 \pm 0.04$	$0.53 \pm 0.09 \pm 0.03$
r (fm)	$0.72 \pm 0.08 \pm 0.03$	$0.55 \pm 0.12 \pm 0.02$	$0.79 \pm 0.10 \pm 0.03$
WITH COULOMB AND PION MISID. CORRECTIONS			
α	$1.03 \pm 0.09 \pm 0.06$	$0.84 \pm 0.08 \pm 0.05$	$0.78 \pm 0.11 \pm 0.04$
r (fm)	$0.76 \pm 0.07 \pm 0.03$	$0.63 \pm 0.09 \pm 0.03$	$0.83 \pm 0.08 \pm 0.03$

6.4 GGLP Effect in Components of Q^2

6.4.1 Motivation

Here we consider the GGLP effect in terms of some of the variables introduced in section 1.3. The purpose behind separating Q^2 into components is to measure a source dimension parameter corresponding to each "direction" defined by the components. Recall from section 1.3 that we have a choice between the classical formulation (Gaussian space-time source distribution)

$$R = 1 + \alpha\, e^{-r_T^2 q_T^2 - r_L^2 q_L^2 - r_0^2 q_0^2}$$

and the invariant formulation based on an expansion of Q^2

$$R = 1 + \alpha\, e^{-r_T^2 q_T^2 - r_L^2 q_L^2 + r_0^2 q_0^2}$$

$$R = 1 + \alpha\, e^{-r_T^2 q_T^2 - r_C^2 q_C^2}$$

where

$$\vec{q}_T \equiv \vec{q} \times \hat{u},$$

$$q_L \equiv \vec{q} \cdot \hat{u},$$

$$q_C^2 \equiv q_L^2 - q_0^2.$$

Thus q_T^2 and q_L^2 are the transverse and longitudinal components, respectively, of $|\vec{q}|^2$ relative to some unit axis $\hat{u}$ defined by the pair or in the event. Recall from chapter one that q_T^2 and q_C^2 are invariant under a boost along the axis $\hat{u}$, while the other variables are not. The parameter r_0 is usually interpreted as a measure of the source lifetime τ in the laboratory: $r_0 = c\tau$. In the sections that follow, we consider two natural choices for the axis $\hat{u}$.

6.4.2 Kopylov Axis Variables

In the Kopylov formulation, $\hat{u}$ is the direction defined by the vector sum of the three-momenta of the pions in a pair:

$$\hat{u} \equiv \frac{(\vec{k}_1 + \vec{k}_2)}{|\vec{k}_1 + \vec{k}_2|}.$$

Unlike the beam direction in nuclear collision experiments or the jet axis in two-jet events, the Kopylov axis can be defined pair by pair in any kind of pion production data.

To study individual components of Q^2, we cumulate uncorrected two dimensional histograms of like and unlike charged pairs, as well as mixed cluster pairs, in three sets of variables: (q_T^2, q_C^2), (q_T^2, q_0^2), and (q_T^2, q_L^2). The ratios of like to unlike charged pairs are then fitted to the following expressions:

$$R(q_T^2, q_C^2) = \gamma(1 + \alpha e^{-r_T^2 q_T^2 - r_C^2 q_C^2})$$

$$R(q_T^2, q_0^2) = \gamma(1 + \alpha e^{-r_T^2 q_T^2 - r_0^2 q_0^2})$$

$$R(q_T^2, q_L^2) = \gamma(1 + \alpha e^{-r_T^2 q_T^2 - r_L^2 q_L^2}).$$

The $R(q_T^2, q_0^2)$ distribution in all four data sets favors the given fitting expression (same sign for both q_T^2 and q_0^2 terms) over the invariant formulation (opposite signs for the q_T^2 and q_0^2 terms). However, we still define $q_C^2 = q_L^2 - q_0^2$ as an invariant component of $Q^2 = q_T^2 + q_C^2$. These fits are also performed on the ratio of like to mixed cluster pairs.

Of course, the same decay products of the K^0 and ρ^0 that we have seen so clearly in the Q^2 distribution of unlike pairs are also present in two-dimensional distributions of unlike pairs. These decay products populate bands of constant $Q^2 = q_T^2 + q_C^2$ and are easily spotted in the ratio of like to unlike pairs in the (q_T^2, q_C^2) distribution. In the case of the other two distributions, (q_T^2, q_0^2) and (q_T^2, q_L^2), we are integrating over one variable (q_L and q_0, respectively), so areas of constant Q^2 are not clear cut bands as in the (q_T^2, q_C^2) distribution. There is no simple way to cut out the regions of these decay products from the fitting region. In order to minimize the effect of the K^0 and ρ^0 on the fitting results, we also study the mixed cluster reference sample. We fit the two-dimensional distributions both for the ratio of like to unlike and the ratio of like to mixed cluster pairs, and we take the average of the two fit values as the measured value. In this way we reduce the effect of the K^0 and ρ^0 distortions on the fitted parameters. We take half of the difference between the two fit values as part of the systematic error to the measured value. The results of these calculations are listed in Table 6.12, and some of the corresponding two-dimensional distributions are shown in Fig. 6.11 and Fig. 6.12.

We see that for each data set (going along a row in Table 6.12), α does not vary much as a function of the three sets of variables. The variation of α with data set (going along a column) follows the pattern seen in pairs: the SPEAR $q\bar{q}$ and PEP $q\bar{q}$ data sets show a significantly lower value of α than the SPEAR J/ψ and PEP $\gamma\gamma$ data sets.

The values of α found by fitting these uncorrected two-dimensional distributions are systematically slightly higher than the values of alpha found by fitting

Table 6.12 *Results of fits to two-dimensional distributions in Kopylov variables. No corrections have been applied to this data. The calculation of these values and the corresponding statistical (first) and systematic (second) errors is discussed in the text. Values of the parameters r_T, r_C, r_0, and r_L are in fm. Since these values are an average of the results found using the unlike pairs and the mixed cluster pairs, we give the χ^2 for the unlike pair analysis first and for the mixed cluster analysis second.*

Data Set	(q_T^2, q_C^2)	(q_T^2, q_0^2)	(q_T^2, q_L^2)
SPEAR J/ψ	$\alpha = 0.74 \pm 0.02 \pm 0.09$ $r_T = 0.77 \pm 0.02 \pm 0.09$ $r_C = 0.88 \pm 0.05 \pm 0.07$ $\chi^2/DOF =$ 1.90, 1.26	$\alpha = 0.70 \pm 0.02 \pm 0.06$ $r_T = 0.85 \pm 0.02 \pm 0.05$ $r_0 = 0.64 \pm 0.03 \pm 0.16$ $\chi^2/DOF =$ 1.58, 1.38	$\alpha = 0.77 \pm 0.02 \pm 0.07$ $r_T = 0.84 \pm 0.02 \pm 0.04$ $r_L = 0.58 \pm 0.02 \pm 0.08$ $\chi^2/DOF =$ 1.59, 1.24
SPEAR $q\bar{q}$	$\alpha = 0.58 \pm 0.03 \pm 0.07$ $r_T = 0.66 \pm 0.04 \pm 0.08$ $r_C = 0.73 \pm 0.07 \pm 0.06$ $\chi^2/DOF =$ 1.13, 1.16	$\alpha = 0.54 \pm 0.03 \pm 0.08$ $r_T = 0.82 \pm 0.05 \pm 0.03$ $r_0 = 0.45 \pm 0.04 \pm 0.03$ $\chi^2/DOF =$ 1.00, 1.19	$\alpha = 0.57 \pm 0.03 \pm 0.06$ $r_T = 0.78 \pm 0.05 \pm 0.06$ $r_L = 0.39 \pm 0.04 \pm 0.03$ $\chi^2/DOF =$ 1.09, 1.18
PEP $\gamma\gamma$	$\alpha = 0.93 \pm 0.10 \pm 0.11$ $r_T = 0.86 \pm 0.06 \pm 0.20$ $r_C = 0.93 \pm 0.13 \pm 0.07$ $\chi^2/DOF =$ 1.21, 1.02	$\alpha = 0.84 \pm 0.05 \pm 0.12$ $r_T = 1.00 \pm 0.05 \pm 0.15$ $r_0 = 0.45 \pm 0.05 \pm 0.03$ $\chi^2/DOF =$ 1.30, 1.02	$\alpha = 0.89 \pm 0.07 \pm 0.10$ $r_T = 0.97 \pm 0.06 \pm 0.16$ $r_L = 0.46 \pm 0.05 \pm 0.03$ $\chi^2/DOF =$ 1.09, 1.06
PEP $q\bar{q}$	$\alpha = 0.40 \pm 0.20 \pm 0.09$ $r_T = 0.90 \pm 0.12 \pm 0.04$ $r_C = 1.41 \pm 0.45 \pm 0.50$ $\chi^2/DOF =$ 1.13, 1.03	$\alpha = 0.25 \pm 0.06 \pm 0.03$ $r_T = 0.94 \pm 0.15 \pm 0.16$ $r_0 = 0.49 \pm 0.15 \pm 0.22$ $\chi^2/DOF =$ 0.90, 0.98	$\alpha = 0.34 \pm 0.11 \pm 0.04$ $r_T = 1.06 \pm 0.15 \pm 0.25$ $r_L = 0.64 \pm 0.18 \pm 0.25$ $\chi^2/DOF =$ 1.13, 1.15

uncorrected distributions in Q^2 (Table 6.2). To understand this, let us consider the Bose-Einstein enhancement in the (q_T^2, q_C^2) distribution. We pick this distribution because the fact that $Q^2 = q_T^2 + q_C^2$ makes this demonstration simpler. Figure 6.13(a) shows the enhancement in the SPEAR J/ψ data, where it is strongest. The enhancement is in the shape of a sombrero centered on the z axis. In the region

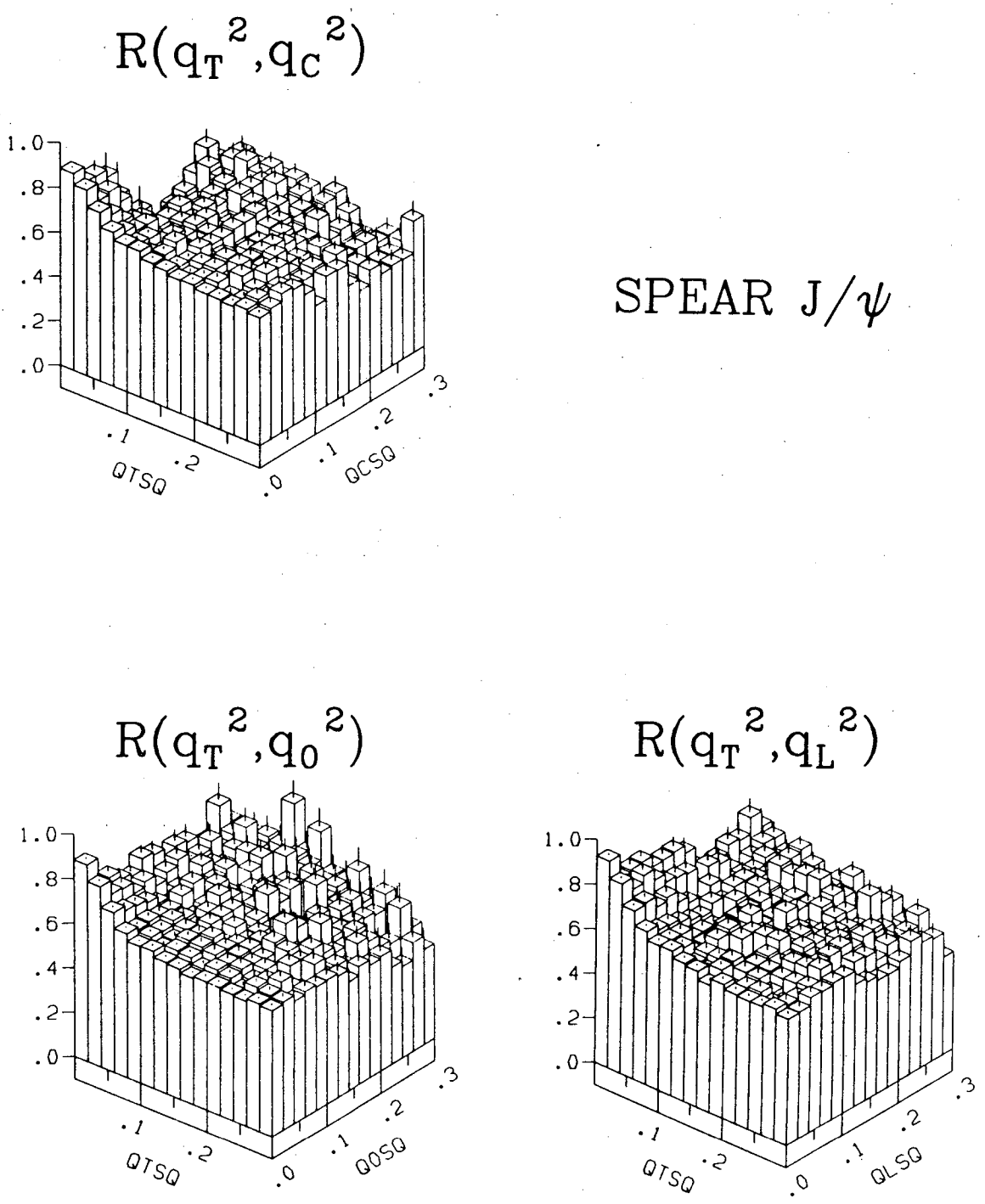

Figure 6.11 *The ratio of like to unlike pairs (no corrections) in the SPEAR J/ψ data. The variables q_T^2, q_L^2, and q_C^2 are defined with respect to the Kopylov axis, and all variables are given in GeV^2.*

$R(q_T^2, q_C^2)$

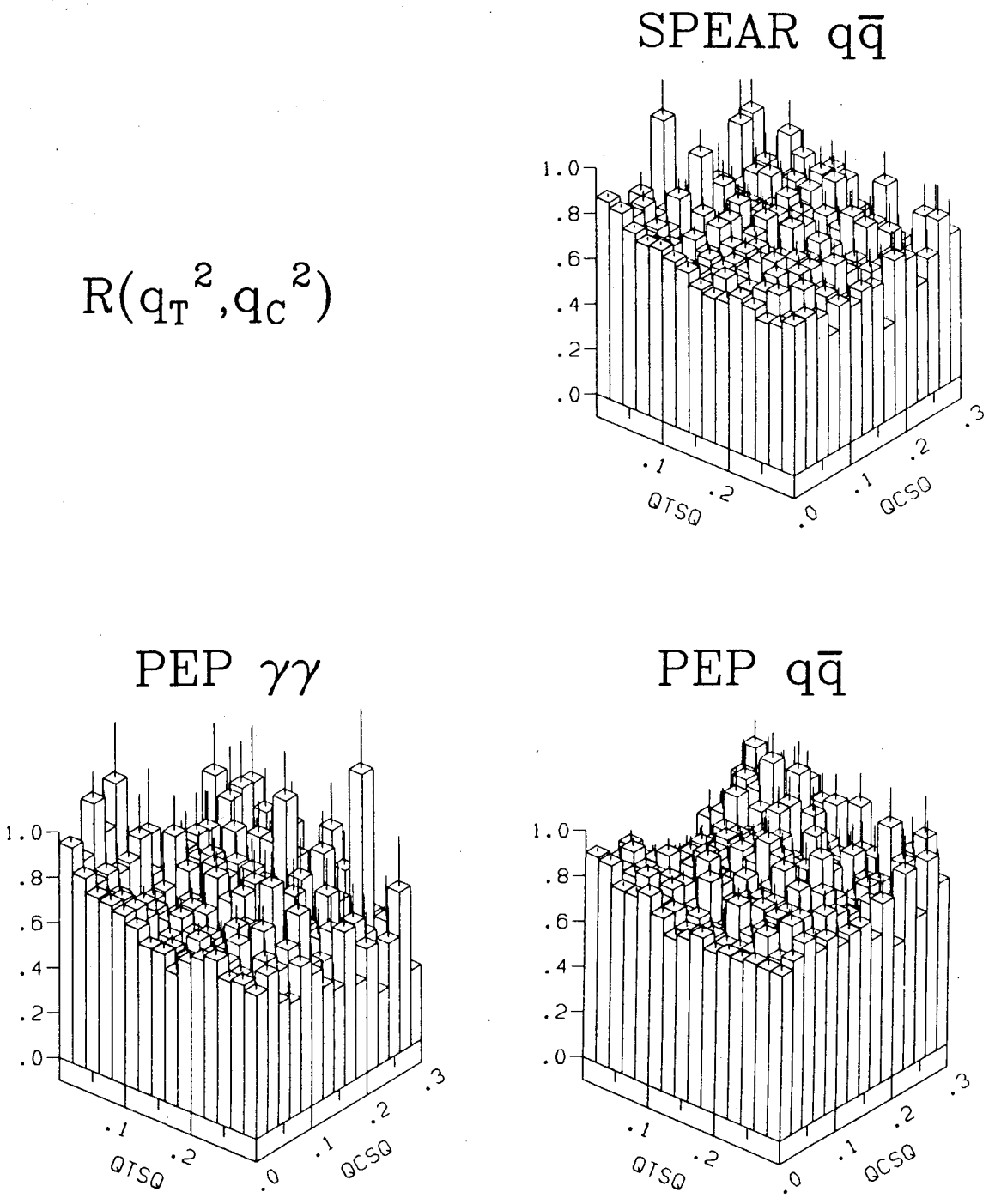

Figure 6.12 *The ratio of like to unlike pairs $R(q_T^2, q_C^2)$ (no corrections) in the SPEAR $q\bar{q}$, PEP $\gamma\gamma$, and PEP $q\bar{q}$ data. The variables q_T^2 and q_C^2 are defined with respect to the Kopylov axis and are given in GeV^2.*

of the rise of the sombrero, the distribution in Q^2 averages over the independent rises in q_T^2 and q_C^2, with the result that the fitted α from the $R(Q^2)$ distributions is slightly lower than the fitted α from the (q_T^2, q_C^2) distribution. This effect can also be seen by fitting slices of the (q_T^2, q_C^2) distribution independently. These slices and their fitted curves are shown in Fig. 6.13(b) and (c). Excluding the K^0 and ρ^0 regions from the fit, we find (statistical errors only):

1. for (q_T^2, $0.00\ GeV^2 < q_C^2 < 0.06\ GeV^2$),

$$\alpha = 0.65 \pm 0.02,$$

$$r_T = 0.78 \pm 0.01\ fm.$$

2. for ($0.00\ GeV^2 < q_T^2 < 0.06\ GeV^2$, q_C^2),

$$\alpha = 0.57 \pm 0.03,$$

$$r_C = 0.76 \pm 0.06\ fm.$$

These α's are smaller than the α derived from the (q_T^2, q_C^2) distribution, because the Bose-Einstein enhancement falls off significantly within the width of the slice. Averaging over the slice, therefore, reduces the observed α. Within error, the measured radii are the same in the two slices as in the (q_T^2, q_C^2) distribution. Note that although the values of α found by fitting the two dimensional distributions are slightly higher than those derived from $R(Q^2)$, the difference is only a few percent. Thus we do not expect that α goes above one (within errors) after full corrections are applied to the SPEAR J/ψ and PEP $\gamma\gamma$ data.

The value of $r_0 \approx r_L < r_T \approx r_C$ in all four data sets, with r_T and r_C approximately equal to the radius r found in the fits to $R(Q^2)$. Similar observations are reported by CLEO[43] and TASSO[44]. In addition, $r_T \approx r_C \approx r$, where r is the parameter extracted by fitting to $R(Q^2)$. Although the definition of q_C^2 clearly indicates that q_C^2 is the longitudinal component of the three-momentum difference

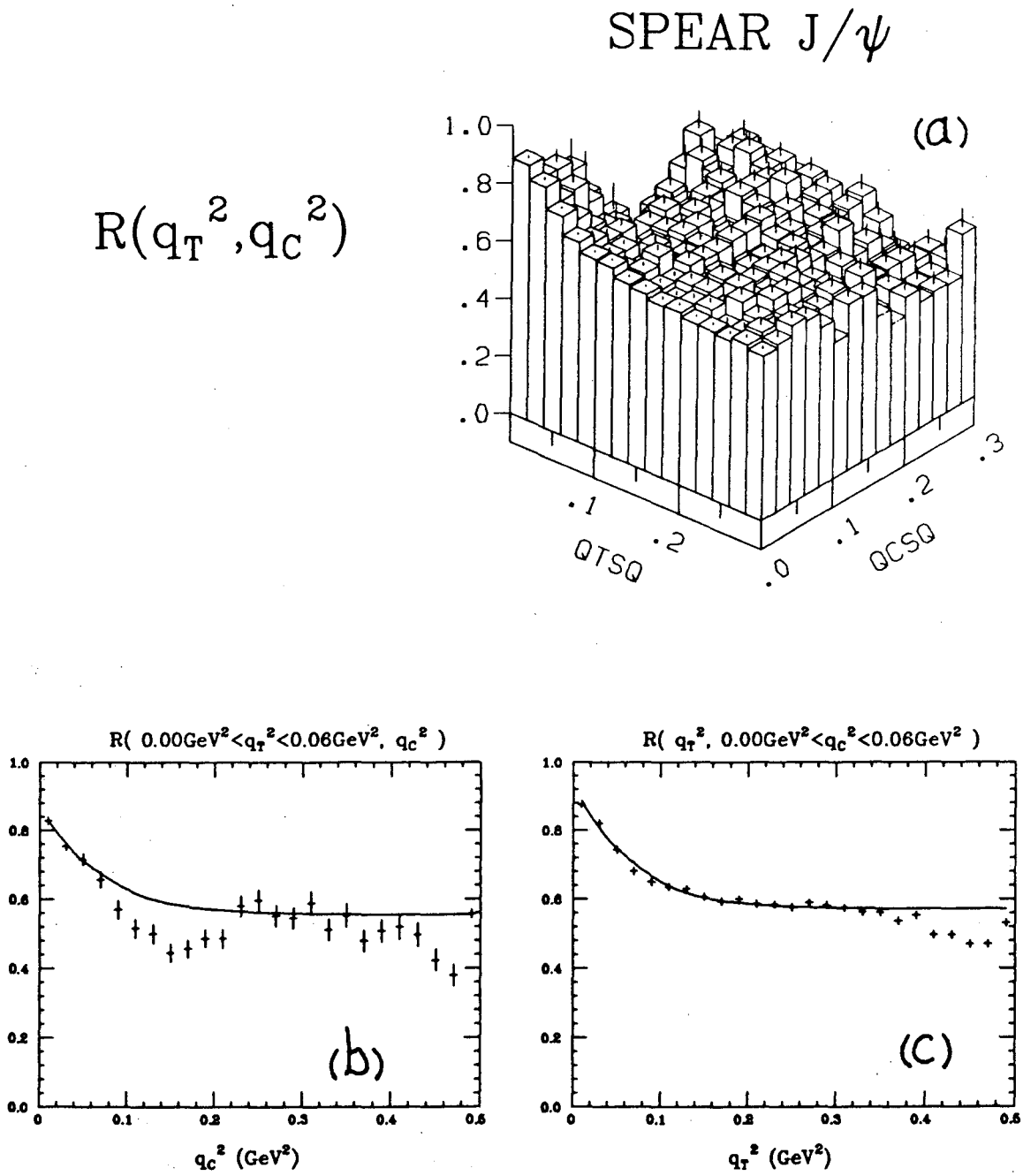

Figure 6.13 *(a) The Bose-Einstein enhancement in $R(q_T^2, q_C^2)$ for the uncorrected ratio of like to unlike pairs in the SPEAR J/ψ data set. The dips due to the K^0 and ρ^0 in the unlike pairs become more evident in (b) when we take a slice consisting of $0.00GeV^2 < q_T^2 < 0.06\ GeV^2$ and project it onto the q_C^2 axis; and in (c) when the slice $0.00GeV^2 < q_C^2 < 0.06\ GeV^2$ is projected onto the q_T^2 axis. The K^0 dip in (b) is nearly absent in (c) due to kinematical constraints. The ρ^0 dip is clearly present in (b) and (c).*

in the pair rest frame (since $q_0 = 0$ in that frame), the interpretation of r_C is highly model dependent. The pair rest frame is different for each pair, so that a fit to a distribution in q_C represents some average over all of these frames. It is therefore not clear whether r_C has a straightforward spatial interpretation. In summary, we find that r_T, a purely spatial parameter, is approximately equal to r_C and to r, two different averages over space and time parameters.

6.4.3 Jet Axis Variables

In a data set consisting of two-jet events, $\hat{u}$ can also be naturally defined as the jet axis. We study r_T, r_C, and r_L defined with respect to this axis using a subset of PEP $q\bar{q}$ data consisting of two-jet events. Again, no corrections have been applied to the data.

Following the fitting procedure described in the previous section, we calculate the values shown in Table 6.13. We find that α does not vary much for the three distributions, and that these values of α are within error of the values found with the Kopylov variables. We also find that $r_0 \approx r_L < r_T \approx r_C$, the same relationship we found using the Kopylov variables. Here, also, we have r_T and r_C approximately equal to the radius r found in the fits to $R(Q^2)$. Similar results showing (in our notation) $r_0 \approx r_L < r_T \approx r_C$ have been found by the AFS Collaboration[4] in two-jet events produced in pp collisions at the ISR.

All the r values found using the jet axis variables are systematically smaller than the corresponding r values found with the Kopylov variables. Note, however, that the jet axis study is done with a subset of the PEP $q\bar{q}$ data (two-jet events only), and that the Kopylov axis study of the previous section is done with all PEP $q\bar{q}$ data, which includes roughly 30% three-jet events.

6.5 Results From Other e^+e^- Experiments

There are three major experiments which have published studies of the Bose-Einstein correlation in e^+e^- annihilation. Their results for pion pair analysis are listed in Table 6.14.

Table 6.13 *Results of fits to jet axis variables in a sample consisting of two-jet events from PEP $q\bar{q}$ data. No corrections have been applied to this data. The calculation of the measured values and the statistical (first) and systematic (second) errors is analogous to the procedure described in the previous section for Kopylov variables. Values of the parameters r_T, r_C, r_0, and r_L are in fm. Since these values are an average of the results found using the unlike pairs and the mixed cluster pairs, we give the χ^2 for the unlike pair analysis first and for the mixed cluster analysis second.*

Data Set	(q_T^2, q_C^2)	(q_T^2, q_0^2)	(q_T^2, q_L^2)
PEP $q\bar{q}$	$\alpha = 0.40 \pm 0.03 \pm 0.06$	$\alpha = 0.33 \pm 0.04 \pm 0.09$	$\alpha = 0.38 \pm 0.04 \pm 0.06$
	$r_T = 0.66 \pm 0.07 \pm 0.07$	$r_T = 0.61 \pm 0.11 \pm 0.04$	$r_T = 0.59 \pm 0.09 \pm 0.08$
	$r_C = 0.71 \pm 0.08 \pm 0.10$	$r_0 = 0.33 \pm 0.08 \pm 0.06$	$r_L = 0.39 \pm 0.09 \pm 0.13$
	$\chi^2/DOF =$ 1.01, 1.03	$\chi^2/DOF =$ 0.94, 0.94	$\chi^2/DOF =$ 0.94, 0.89

The CLEO group[43] has looked at the $\Upsilon(1S)$ region and the continuum below and above the $\Upsilon(4S)$. They use unlike charged pairs as the reference sample and make no Coulomb or pion misidentification corrections. Their (thus uncorrected) value of α is the same within errors for these regions and is very close to our uncorrected value of α for the SPEAR $q\bar{q}$ data set. The latter contains open charm production, while CLEO's data above the $\Upsilon(1S)$ contains both open charm and bottom production. As we have seen earlier, our analysis indicates a significant difference between the values of α for the SPEAR J/ψ data and the SPEAR $q\bar{q}$ data. The CLEO group also attempts to correct for the presence of long lived resonances in the data, assuming that pions from the decay of these resonances would not contribute to the Bose-Einstein enhancement of the pions from the primary source. Their correction for this effect raises the value of α above the maximum of one, leaving no room for other detector and source effects which act to lower α.

The TPC group[36] studied two-jet events at $\sqrt{s} = 29\ GeV$. They use pairs from mixed events as the reference sample and correct for both Coulomb effects and pion misidentification. We can thus compare their corrected measurements with our fully corrected values for the PEP $q\bar{q}$ data set. Our measurement of α is

Table 6.14 *Summary of studies of the GGLP effect in pion pairs by other major e^+e^- experiments.*

	CLEO	TPC	TASSO
$\sqrt{s}$	$\Upsilon(1S) \sim 10.5\ GeV$	$29\ GeV$	$29 - 34\ GeV$
corrections	none	Coulomb, pion misid.	R/R_{MC}
our comparable data set	uncorrected SPEAR J/ψ SPEAR $q\bar{q}$	corrected PEP $q\bar{q}$	corrected PEP $q\bar{q}$
R	$R(q_T)$	$R(Q)$	$R(Q^2)$
fitting form for R	$\gamma(1+\alpha e^{-r^2 q_T^2})$	$\gamma(1+\delta Q)\times$ $(1+\alpha e^{-r^2Q^2})$	$\gamma(1+\alpha e^{-r^2Q^2})$
measured values, statistical errors only	$\alpha = 0.43 \pm 0.07$ $r = 0.86 \pm 0.15$	$\alpha = 0.61 \pm 0.05$ $r = 0.65 \pm 0.04$	$\alpha = 0.60 \pm 0.09$ $r = 0.76 \pm 0.12$
shape of jet source		ellipsoid, but consistent with sphere	spherical $r \sim 0.7\ fm$
triplets			$R(like/\pm\pm\mp)$ $\alpha_{3\pi} = 1.65 \pm 0.36$ $r_{3\pi} = 0.52 \pm 0.07$

slightly lower than theirs, while our measurement of r is slightly higher, but the measurements agree within errors. The TPC group uses the familiar

$$R = 1 + \alpha e^{-r^2Q^2}$$

with

$$r \equiv \frac{r_a}{\sqrt{\sin^2\theta + \cos^2\theta/k^2}}$$

to investigate the shape of the pion source with respect to the jet axis. Here θ is the angle between the net three-momentum of the pair and the jet axis, and k and

r_a are fitted parameters. They find that

$$k = 2.0^{+1.3}_{-0.8},$$

indicating that an ellipsoidal shape is preferred (long axis along jet axis), but that the data is consistent with a sphere within errors. We have seen in the preceding section that we find a spherical source shape in an equivalent analysis with jet axis variables.

The TASSO Collaboration[44] studied pion pairs and triplets at $\sqrt{s} = 29 - 34\ GeV$. They performed corrections on their data by fitting the ratio of R/R_{MC}, as we discussed in section 6.1.3. Their values of α and r are within errors of our values for the fully corrected PEP $q\bar{q}$ data set. The TASSO group investigated the shape of the jet source by looking at two dimensional distributions of q_T^2 and q_C^2 (which they label Q_T^2 and Q_L^2) and fitting this distribution to the expression

$$R = (1 + \delta q_T^2 + \epsilon q_C^2)(1 + \alpha e^{-r_T^2 q_T^2 - r_C^2 q_C^2}).$$

This is similar to the procedure we followed in the previous section (jet axis variables). As we see in Table 6.14, they find a spherical source with nearly the same radii and α as we find in the PEP $q\bar{q}$ data set using the jet axis variables. Finally, the TASSO group also studied pion triplets. Their values for the ratio of like charged triplets to $\pm\pm\mp$ triplets are (statistical errors only):

$$\alpha_{3\pi} = 1.65 \pm 0.36,$$

$$r_{3\pi} = 0.52 \pm 0.07\ fm.$$

These are within errors of the fully corrected values we find with the PEP $q\bar{q}$ data set.

6.6 CONCLUSIONS

Figure 6.14 displays the values of α and r for the pair analysis of the four data sets, arranged roughly in the order of increasing energy available for hadron

production. We find that after all corrections have been applied, the SPEAR J/ψ and PEP $\gamma\gamma$ data sets show nearly maximum values of α. There is no evidence of a decrease in α due to long lived resonances (section 4.2) such as the ρ, ω, and ϕ. Like CLEO (section 6.5), we find that correcting for long lived resonances would bring α above its maximum expected value of one in these two data sets. Similarly, no suppression due to the effects of the final state strong interaction (section 4.5.2) is evident within errors in these data sets.

The SPEAR $q\bar{q}$ and PEP $q\bar{q}$ data sets show significantly smaller values of α. In appendix B we use a Monte Carlo calculation to show that a major fraction of this suppression in α can be ascribed to the presence of charm mesons in the SPEAR $q\bar{q}$ data and both charm and bottom mesons in the PEP $q\bar{q}$ data, leaving only a small part of the suppression as possible evidence of source coherence. The values of the parameter r seem to be fairly constant for the four data sets.

Results of the triplet analysis in the four data sets are summarized in Figure 6.15, which displays the values of $\alpha_{3\pi}$ and $r_{3\pi}$ found using the mixed cluster reference sample. Although statistics are more limited in triplet analysis than in pair analysis, overall we find qualitatively similar patterns in $\alpha_{3\pi}$ and $r_{3\pi}$ as we do in α and r. The SPEAR J/ψ data set, with the largest statistics, clearly shows nearly maximum value of $\alpha_{3\pi}$ using the mixed cluster reference sample with all corrections. We find evidence for a purely triplet enhancement term μ in triplet Bose-Einstein correlations in all four data sets. Within the limitations imposed by available statistics, we also find that μ qualitatively follows the same pattern as α does in these data sets. The value of $r_{3\pi}$ is approximately the same for all the data and is between 1/3 and 1/2 of the value of r, as expected (section 5.1.2).

We consider α and r as a function of p_{Tmax} in the PEP $\gamma\gamma$ data in order to establish if the GGLP effect sees a difference between the hadronic source dominant at high p_{Tmax} and the one dominant at low p_{Tmax}. Figure 6.16 displays the values of α and r for pair analysis in the PEP $\gamma\gamma$ data as a function of p_{Tmax}. Within the available statistics, we find that α in the lowest p_{Tmax} bin is consistent with maximum value, and that α decreases with increasing p_{Tmax} as the direct annihilation

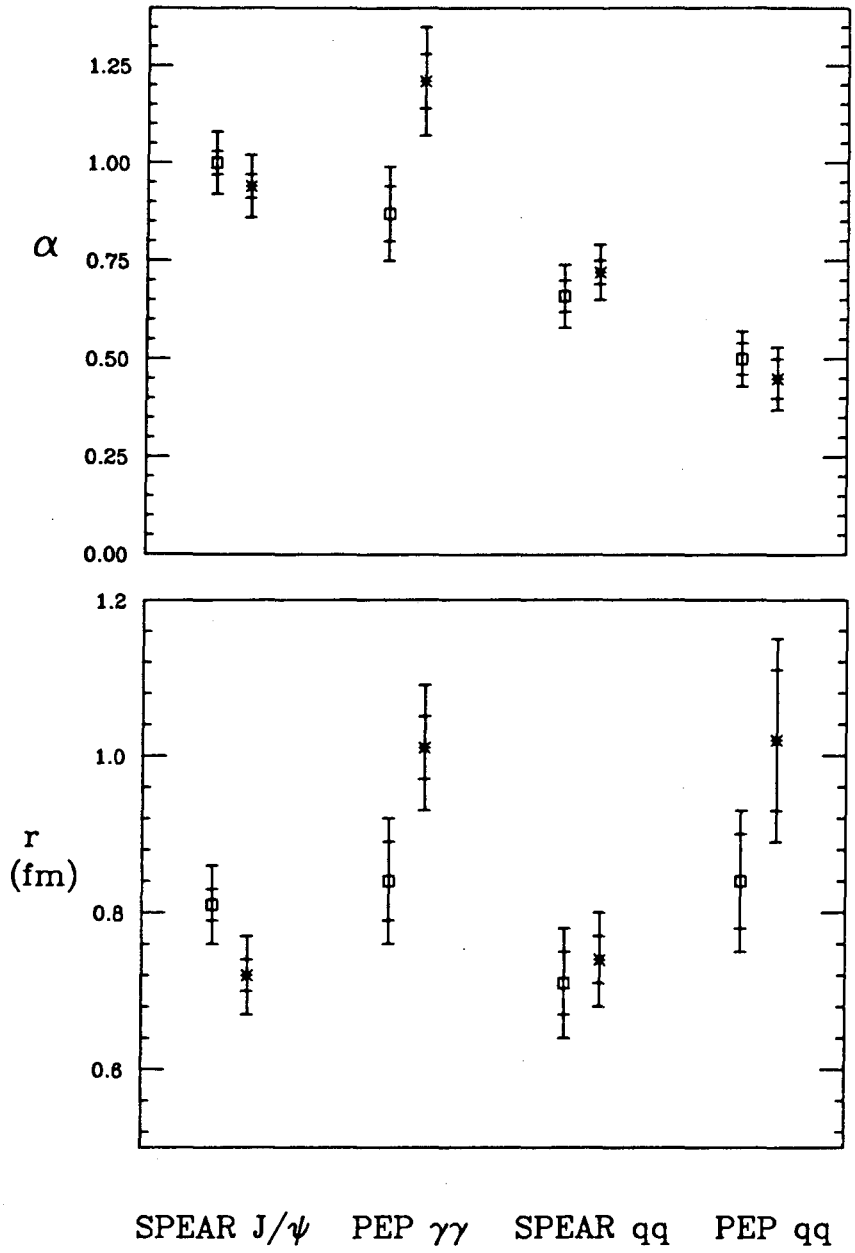

Figure 6.14 *Plots of α and r for the four data sets, arranged roughly in the order of increasing energy available for hadron production. The values shown are for the fully corrected ratio of like to unlike charged pairs (circles) and of like to mixed cluster pairs (stars). The errors indicated are statistical (inner) plus systematic (outer).*

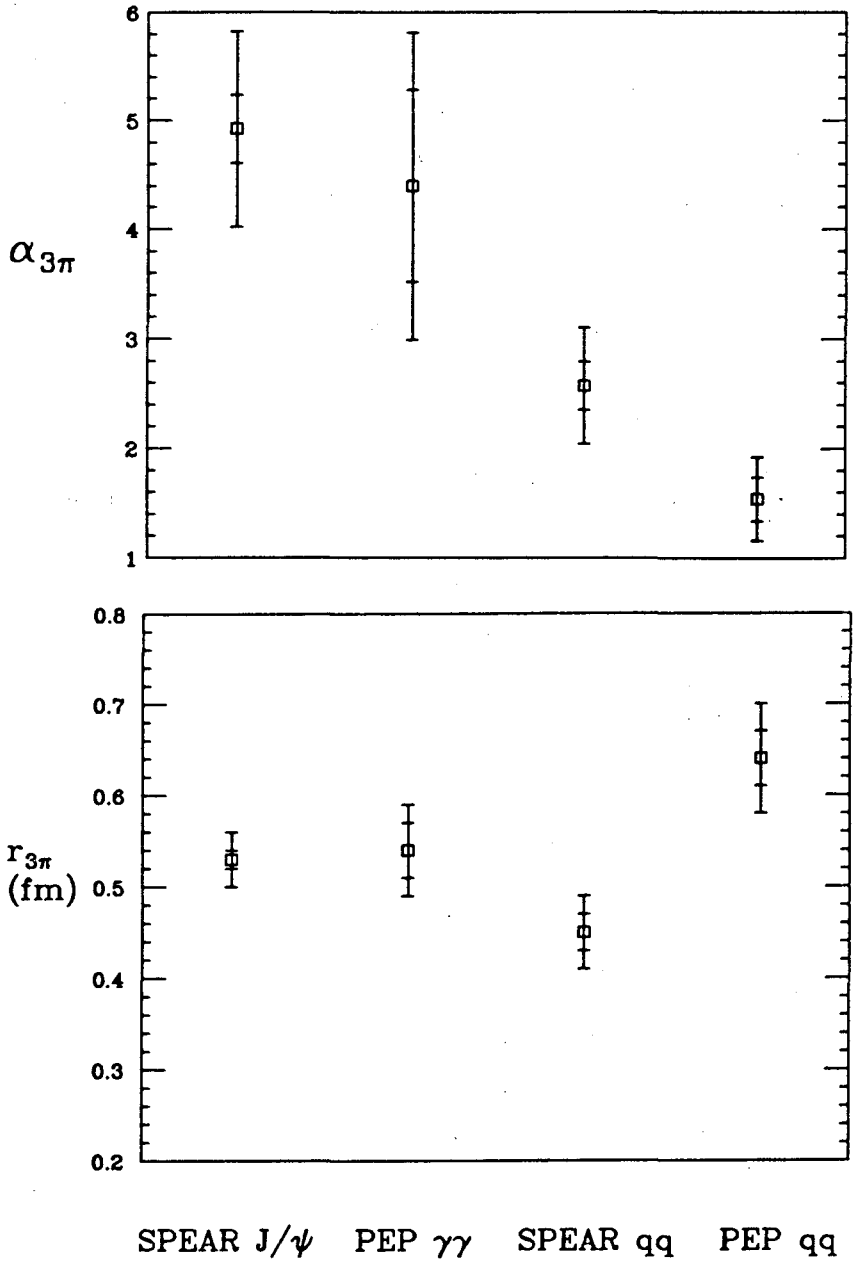

Figure 6.15 *Plots of $\alpha_{3\pi}$ and $r_{3\pi}$ for the four data sets, arranged roughly in the order of increasing energy available for hadron production. The values shown are for the fully corrected ratio of like to mixed cluster triplets. Statistical errors are indicated by the inner bars while systematic errors are indicated by the difference between the inner and outer bars.*

of the two photons into $q\bar{q}$ becomes the dominant hadronic source.

A study of the pion pair Bose-Einstein enhancement in the two-dimensional distribution $R(q_T^2, q_C^2)$ gives the same value for the purely spatial parameter r_T as for r_C and r, two different averages of space and time parameters. This result is obtained both when q_T is calculated with respect to the net pair three-momentum and when it is calculated with respect to the jet axis for two-jet events in the PEP $q\bar{q}$ data set. Similar results have been reported by CLEO[43], TASSO[44], and AFS[4]. Fits to the two-dimensional distributions $R(q_T^2, q_L^2)$ and $R(q_T^2, q_0^2)$, which contain the non-invariant variables q_L and q_0, indicate $r_0 \approx r_L \approx \frac{2}{3} r_T$ to $\frac{1}{2} r_T$.

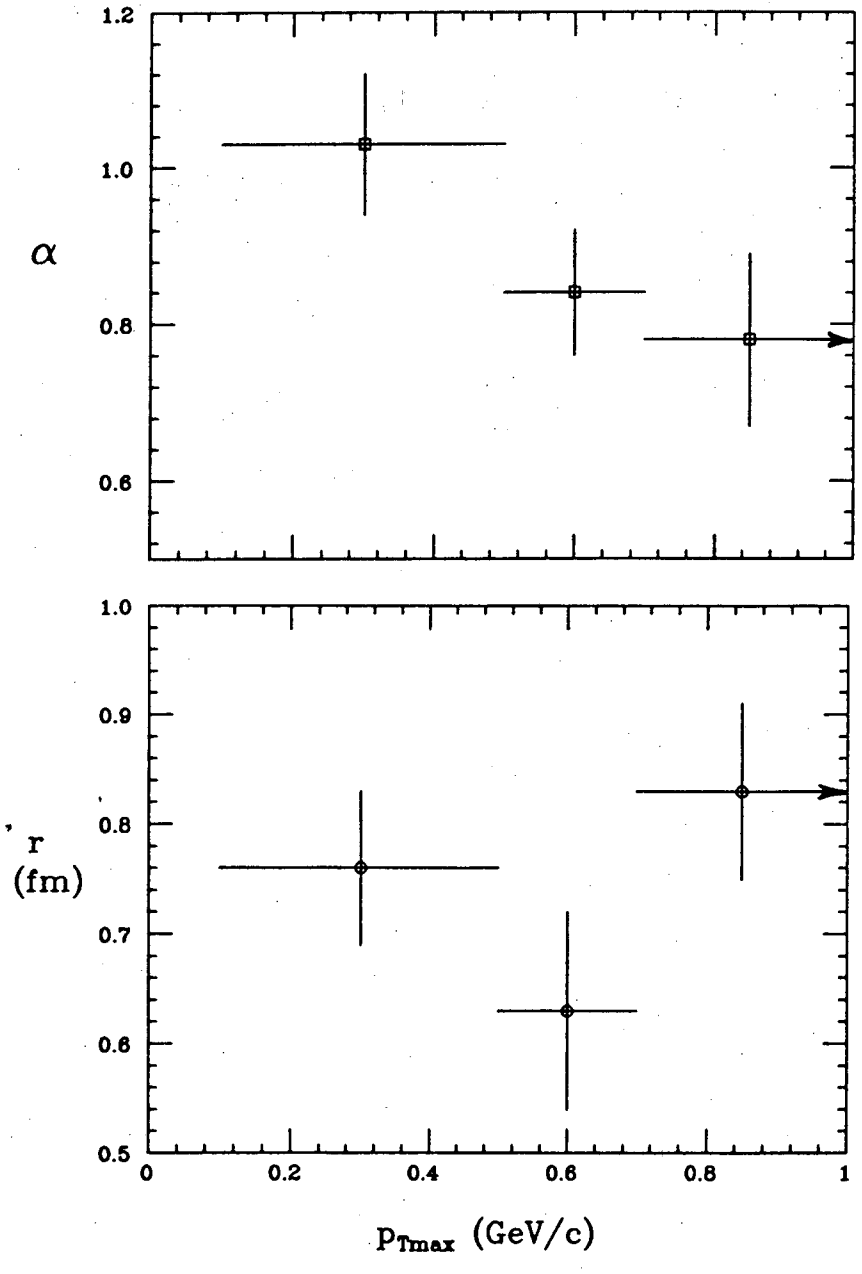

Figure 6.16 *Plots of α and r for the PEP $\gamma\gamma$ data set as a function of p_{Tmax}. The values shown are for the fully corrected ratio of like to unlike charged pairs, and the errors indicated are statistical.*

Appendix A. RESIDUAL CORRELATIONS

Recall that in order to do pair analysis we require that at least three pions and both charges be present in the event. In an unlike charged pair, therefore, at least one pion comes from a set of two or more like charged (Bose-Einstein correlated) pions. A residual correlation arises from the fact that the phase space density of single pions in the presence of the Bose-Einstein correlation, the measured $\rho_{be}(k)$, is different from the one in the absence of the Bose-Einstein correlation, the ideal $\rho(k)$. In this section we estimate the effect of this residual correlation on the reference samples we use.

Let us denote the suitably normalized pair phase space density in the study sample as $\rho^s(k_1, k_2)$, where k_1 and k_2 are pion four-momenta. Note that $\rho^s(k_1, k_2)$ contains all the correlations between like charged pairs, including the Bose-Einstein enhancement. Similarly, let $\rho^r(k_1, k_2)$ represent the pair phase space density in the ideal reference sample. The reference density is factored into

$$\rho^r(k_1, k_2) = \rho(k_1)\rho(k_2),$$

where $\rho(k_1)$ and $\rho(k_2)$ represent the single particle phase space densities of the two pions in the absence of the Bose-Einstein correlation. We saw in chapter one that the correlation function is given by Eqn. A.1

$$R(k_1, k_2) = \frac{\rho^s(k_1, k_2)}{\rho^r(k_1, k_2)} = \frac{\rho^s(k_1, k_2)}{\rho(k_1)\rho(k_2)}. \qquad (A.1)$$

Both of our reference samples, unlike charged pairs and mixed cluster pairs, consist of pions which populate $\rho_{be}(k)$ rather than $\rho(k)$, so that the correlation we measure is given by

$$R_{be}(k_1, k_2) = \frac{\rho^s(k_1, k_2)}{\rho_{be}(k_1)\rho_{be}(k_2)},$$

where

$$\rho_{be}(k_1) \equiv \int \rho^s(k_1, k_2)\ dk_2.$$

Substituting from Eqn. A.1, we get

$$\rho(k_1) = \rho_{be}(k_1) \frac{1}{\int R(k_1, k_2)\rho(k_2)\ dk_2} \equiv \rho_{be}(k_1) W(k_1).$$

Thus in order to get the ideal single pion density $\rho(k_1)$ we must weight each pion in the measured single pion density $\rho_{be}(k_1)$ by a correction factor $W(k_1)$. In effect, $1/W(k_1)$ measures the average Bose-Einstein correlation between a pion of momentum k_1 and a set of pions populating $\rho(k)$.

Since we do not know $R(k_1, k_2)$ or $\rho(k_2)$, we calculate a first approximation as follows:

$$\rho_1(k_1) = \rho_{be}(k_1) \frac{1}{\int R_{be}(k_1, k_2)\rho_{be}(k_2)\ dk_2} \equiv \rho_{be}(k_1) W_{be}(k_1),$$

and

$$R_1(k_1, k_2) = \frac{\rho^s(k_1, k_2)}{\rho_1(k_1)\rho_1(k_2)}.$$

We use an iterative procedure [37] to get the n'th approximation to R:

$$\rho_n(k_1) = \rho_{be}(k_1) \frac{1}{\int R_{n-1}(k_1, k_2)\rho_{n-1}(k_2)\ dk_2} \equiv \rho_{be}(k_1) W_{n-1}(k_1),$$

and

$$R_n(k_1, k_2) = \frac{\rho^s(k_1, k_2)}{\rho_{n-1}(k_1)\rho_{n-1}(k_2)}.$$

Now we consider the specific case of our study and reference samples. We calculate R_1 and compare it to R_{be} in order to get an estimate of the effect of the residual correlation. Because of the complexity and variety of events in the four data sets, we focus on representative special cases.

The first step is to map out the single pion phase space density $\rho_{be}(k)$ in terms of the variables (k_x, k_y, k_z) which are used to calculate $R_{be}(k_1, k_2)$. The map consists of a three dimensional histogram, since k_0 is calculated from the space components when needed. Rigorously, the density $\rho_{be}(k)$ depends on both the π^+ and the π^- multiplicity in the event. Table A.1 shows the charged pion multiplicities in the four data sets. In order to apply the same procedure to all four data sets, we again work with clusters in an event rather than events themselves. In the case of SPEAR J/ψ, SPEAR $q\bar{q}$, and PEP $\gamma\gamma$ data sets, almost always there is only one cluster per event, so the average pion multiplicities in the event as well as the cluster are approximately two π^+'s and two π^-'s. In the PEP $q\bar{q}$ data set pion multiplicities per event are of course higher, but the average pion multiplicities in each cluster are approximately two π^+'s and two π^-'s. Keeping track of the single pion phase space density in three variables, for four data sets, and for each possible combination of $N_{\pi+}$ and $N_{\pi-}$ would be prohibitive in terms of computer time and memory. Therefore, with the average multiplicities in mind, we consider the representative case in each data set of events with two π^+'s and two π^-'s per cluster.

Table A.1 *Average charged pion multiplicity in an analysis event.*

	per cluster		per event	
Data Set	$N_{\pi\pm}$	$\langle N_{\pi\pm}\rangle$	$N_{\pi\pm}$	$\langle N_{\pi\pm}\rangle$
SPEAR J/ψ	$1.0 < N_{\pi\pm} < 5.0$	1.8	$1.0 < N_{\pi\pm} < 5.0$	1.8
SPEAR $q\bar{q}$	$1.0 < N_{\pi\pm} < 7.0$	2.0	$1.0 < N_{\pi\pm} < 7.0$	2.0
PEP $\gamma\gamma$	$1.0 < N_{\pi\pm} < 8.0$	1.9	$1.0 < N_{\pi\pm} < 8.0$	1.9
PEP $q\bar{q}$	$1.0 < N_{\pi\pm} < 9.0$	2.1	$1.0 < N_{\pi\pm} < 11.0$	3.9

Once we have a map of $\rho_{be}(k)$, $W_{be}(k)$ is calculated using $R_{be}(k_1, k_2)$ fitted to the expression $R(Q^2) = 1 + \alpha \exp(-r^2 Q^2)$, the standard parameterization discussed in chapter one. The parameters α and r are the fitted values for each data set

from chapter six. Like $\rho_{be}(k)$, $W_{be}(k)$ is a three dimensional histogram of weights associated with each pion momentum $\vec{k}$.

To create the reference sample represented by $\rho_1(k_1)\rho_1(k_2)$, we weight each unlike charged pion pair by the product of the individual pion weights $W_{be}(k_1)W_{be}(k_2)$. Then R_1 is calculated and fitted using the resulting reference sample in the same way that R_{be} is calculated and fitted using $\rho_{be}(k_1)\rho_{be}(k_2)$. Table A.2 shows that the fitted parameters of R_{be} and R_1 are well within statistical errors of each other.

Table A.2 *Fitted values of α and r for R_{be} and R_1. The parameterization is the standard $R(Q^2) = 1 + \alpha\exp(-r^2Q^2)$. As discussed in the text, the events (or clusters in the case of PEP $q\bar{q}$ data) used in this comparison are required to have two π^+'s and two π^-'s, and the errors quoted are statistical.*

	R_{be}		R_1	
Data Set	α	$r\ (fm)$	α	$r\ (fm)$
SPEAR J/ψ	0.58 ± 0.06	0.86 ± 0.11	0.59 ± 0.06	0.81 ± 0.12
SPEAR $q\bar{q}$	0.32 ± 0.07	0.68 ± 0.25	0.33 ± 0.07	0.60 ± 0.27
PEP $\gamma\gamma$	0.79 ± 0.10	0.66 ± 0.18	0.83 ± 0.11	0.56 ± 0.17
PEP $q\bar{q}$	0.24 ± 0.04	0.79 ± 0.21	0.24 ± 0.05	0.76 ± 0.31

Because of the nature of the cluster mixing algorithm, the calculation of the residual correlation in the mixed cluster reference sample is analogous to the one described above for the unlike charged pairs. Thus the fitted parameters of R_{be} and R_1 using mixed cluster pairs are also expected to be the same within errors.

Since the correction in the first iteration $R_1 - R_{be}$ is relatively small, we conclude that the effect of the residual correlation can be neglected: the ideal R is nearly the same as the ratio R_{be} that we measure using the uncorrected unlike pair or mixed cluster pair reference sample. In summary, therefore, we make no residual correlation corrections in this analysis.

Appendix B. LONG LIVED RESONANCES AND PARTICLES

Recall from section 4.2 that many of the charged pions in the study sample are the decay products of resonances and particles, such as K^0, ρ^0, ω^0, etc., and charm and bottom mesons. We say that a resonance is long lived if it decays over a time which is long compared to the size of the primary source. If a pion from a long lived resonance is paired with a pion from the primary source, such a pair will reflect the resonance decay length rather than the dimension of the primary source. The study sample will then measure some complicated average of the source dimension and all the decay lengths. From the familiar parameterization of R,

$$R = 1 + \alpha\, e^{-r^2Q^2},$$

we can also see that, for a given value of α, as the value of r increases the Bose-Einstein enhancement gets narrower in Q^2. As we determined in section 4.6.2, for $r > 5.9\ fm$ the MARK II drift chamber is unable to resolve the $\triangle Q$ of the two tracks, and we in effect lose that pair and its contribution to the Bose-Einstein enhancement. One explanation of the observation of a less than maximum value of α has been the claim that the presence of long lived resonances and their corresponding ultra-narrow and unobservable contribution to the Bose-Einstein enhancement in effect suppresses the measured value of α from its true value.

Our measurement of α in the SPEAR J/ψ and PEP $\gamma\gamma$ data sets finds a value close to maximum, with no apparent suppression by the long lived resonances present in these data sets. The SPEAR $q\bar{q}$ and PEP $q\bar{q}$ data sets, however, show a significantly smaller α. The major difference between the SPEAR J/ψ, PEP $\gamma\gamma$ data sets and the SPEAR $q\bar{q}$, PEP $q\bar{q}$ data sets, in terms of resonances produced, is the presence of charm mesons in SPEAR $q\bar{q}$ data and charm and bottom mesons in PEP $q\bar{q}$ data. If we assume on the basis of the measurement of α in SPEAR J/ψ and PEP $\gamma\gamma$ data that other long lived resonances introduce no suppression of

α, then we can use Monte Carlo data to estimate how large a suppression we can expect from the presence of charm and bottom mesons alone.

In order to make this estimate, we analyze Monte Carlo data with the same cuts and in the same way as we do the four data sets. The ratio of the resulting like to unlike charged pair distributions is of course flat near $Q^2 = 0$ since our Monte Carlo does not model the Bose-Einstein correlation (see Fig. 4.8). We introduce a representation of the Bose-Einstein correlation into the Monte Carlo by weighting a like charged pair with the expression above and a given set of α and r. In this study, we use $(\alpha, r) = (1.0, 0.8fm)$. If we weight only pairs of pions which are correctly identified as pions, the resulting distribution corresponds to data distributions which have been fully corrected. (Recall that Monte Carlo data does not simulate the final state Coulomb interaction, so no correction is required for that effect here.)

Figure B.1(a) shows the ratio of weighted like to unlike charged pairs in the Monte Carlo, where all the like charged pairs have been weighted. We show this distribution in order to establish that the input variables α and r come out the same within errors in the fit. The solid curve in Fig. B.1(a) is the fitted expression

$$R = \gamma\ (1 + \delta\ Q^2)\ (1 + \alpha\ e^{-r^2Q^2})$$

with

$$\alpha = 0.98 \pm 0.03$$

$$r = 0.80 \pm 0.02\ fm$$

$$\delta = 0.16 \pm 0.02\ GeV^{-2}.$$

The PEP $q\bar{q}$ data set contains both charm and bottom mesons. To model this data we weight all like charged Monte Carlo pairs of correctly identified pions except the decay products of charm and bottom mesons. Figure B.1(b) shows the ratio of these weighted like to unlike Monte Carlo data pairs, The solid curve corresponds to

$$\alpha = 0.63 \pm 0.03$$

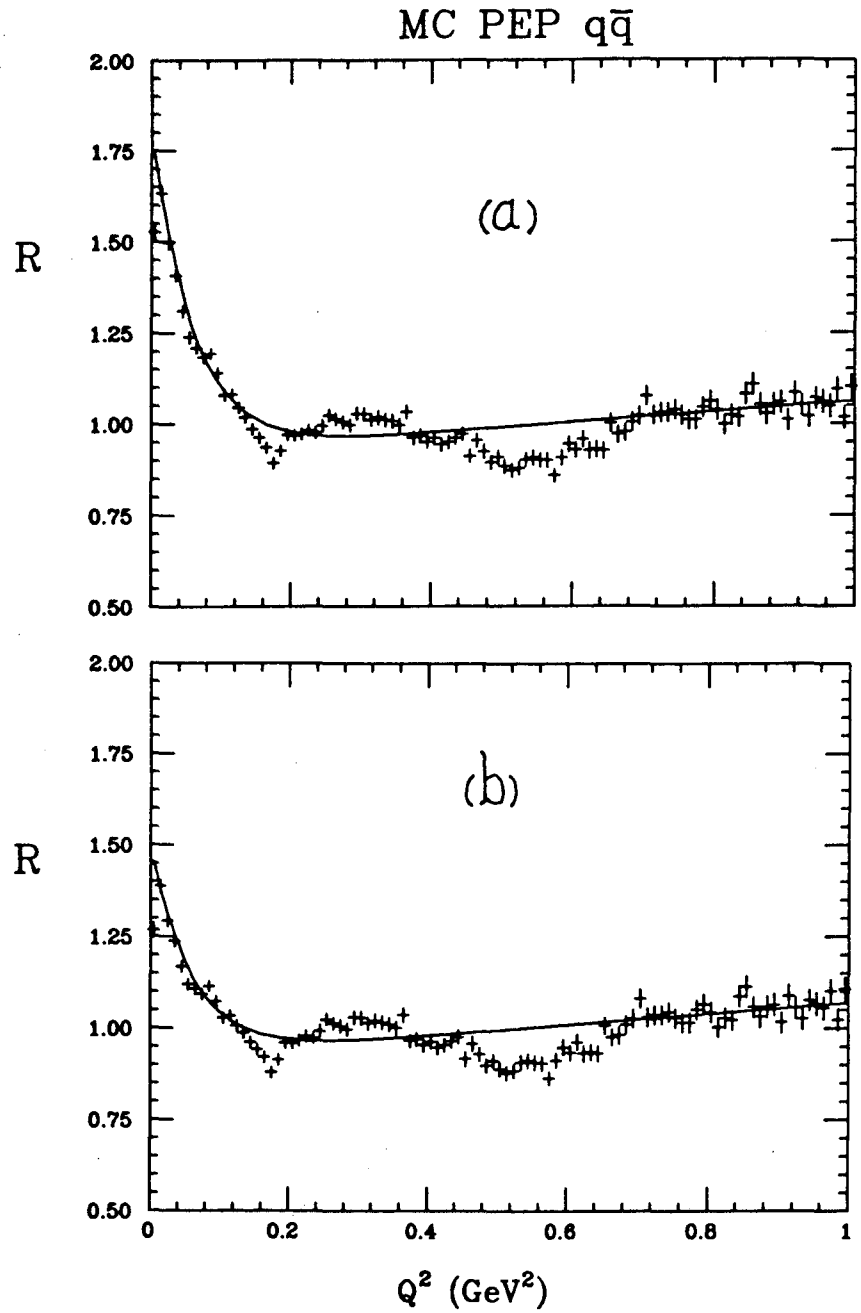

Figure B.1 *Ratios of weighted like to unlike charged pairs in the Monte Carlo data and the corresponding fitted curves. (a) All like charged pairs have been weighted. (b) Here we weight all like charged pairs of correctly identified pions except the decay products of charm and bottom mesons. This distribution corresponds to a fully corrected data distribution.*

$$r = 0.81 \pm 0.04\ fm$$

$$\delta = 0.16 \pm 0.02\ GeV^{-2}.$$

The SPEAR $q\bar{q}$ data set contains charm but no bottom mesons. To see what effect this combination has on α, we weight all like charged Monte Carlo pairs of correctly identified pions except the decay products of charm mesons. The fitted values are essentially the same:

$$\alpha = 0.66 \pm 0.03$$

$$r = 0.82 \pm 0.04\ fm$$

$$\delta = 0.16 \pm 0.02\ GeV^{-2}.$$

Comparing these results with the fitted parameters in the fully corrected PEP $q\bar{q}$ data set (Table 6.3),

$$\alpha = 0.50 \pm 0.04$$

$$r = 0.84 \pm 0.06\ fm$$

$$\delta = 0.23 \pm 0.03\ GeV^{-2},$$

we see that the presence of charm and bottom mesons seems to account for the major fraction of the suppression of α from its maximum value. Only a small part of the suppression remains as possible evidence of source coherence.

REFERENCES

1. E. Merzbacher, QUANTUM MECHANICS, John Wiley & Sons, Inc., New York, 1970.
2. G. Goldhaber *et al.*, Phys. Rev. Lett. **3**, 181 (1959).
3. G. Goldhaber *et al.*, Phys. Rev. **120**, 300 (1960).
4. T. Åkesson *et al.*, AFS Collaboration, Phys. Lett. **155B**, 128 (1985).
5. Zarbaksh *et al.*, Phys. Lett. **46**, 1268 (1981).
6. W. A. Zajc, HADRONIC MULTIPARTICLE PRODUCTION, World Scientific Book, edited by Peter Carrutherrs, (1988).
7. G. Goldhaber and I. Juricic, PROCEEDINGS OF THE SECOND INTERNATIONAL WORKSHOP ON LOCAL EQUILIBRIUM IN STRONG INTERACTION PHYSICS, edited by P. Carruthers and D. Strottman, World Scientific Publishing Co. (1986), (LBL-25131).
8. G. I. Kopylov and M. I. Podgoretskii, Sov. J. Nucl. Phys. **15**, 219 (1972).
9. E. V. Shuryak, Phys. Lett. **44B**, 387 (1973).
10. G. Cocconi, Phys. Lett. **49B**, 459 (1974).
11. R. Hanbury-Brown and R. Q. Twiss, Nature **178**, 1046 (1956).
12. A. D. Chacon *et al.*, LBL-18709 (1987). To be submitted to Phys. Rev. Lett.
13. B. Andersson and W. Hoffman, Phys. Lett. **169B**, 364 (1986).
14. M. G. Bowler *et al.*, Z. Phys. C **29**, 617 (1985).
15. M. G. Bowler, Phys. Lett. **180B**, 299 (1986).
16. R. H. Schindler, *et al.*, Phys. Rev. D **24**, 78 (1981).
17. J. Jaros, PROCEEDINGS OF THE INTERNATIONAL CONFERENCE ON INSTRUMENTATION FOR COLLIDING BEAM PHYSICS, SLAC-Report 250, (1982), edited by W. Ash.
18. W. Davies-White, *et al.*, Nuc. Instr. Meth. **160**, 227 (1979).
19. R. H. Schindler, Ph.D. Thesis, Stanford University, SLAC-Report 219, (1979), (unpublished).
20. There were 98 phototubes at SPEAR. Because of difficulties with the magnet coil at PEP, three of the phototubes had to be removed for running in the

PEP configuration.

21. G. S. Abrams, *et al.*, IEEE Trans. NS-**25**, 309 (1978); NS-**27**, 59 (1980).
22. K. G. Hayes, Ph.D. Thesis, Stanford University, SLAC-Report 2371, (1981), (unpublished).
23. J. D. Fox and M. E. B. Franklin, IEEE Trans, NS-**28**, 3 (1981).
24. J. F. Patrick, Ph.D. Thesis, University of California, Berkeley, LBL-14585, (1982), (unpublished).
25. H. M. Schellman, Ph.D. Thesis, University of California, Berkeley, LBL-18699, (1984), (unpublished).
26. T. Himel, Ph.D. Thesis, Stanford University, SLAC-Report 2231, (1979), (unpublished).
27. D. E. Amidei, Ph.D. Thesis, University of California, Berkeley, LBL-17795, (1984), (unpublished).
28. M. W. Eaton, Ph.D. Thesis, University of California, Berkeley, LBL-14581, (1982), (unpublished).
29. M. E. Nelson, Ph.D. Thesis, University of California, Berkeley, LBL-16724, (1983), (unpublished).
30. PROCEEDINGS OF THE WORKSHOP ON RADIATION DAMAGE TO WIRE CHAMBERS, Lawrence Berkeley Laboratory, January 1986, LBL-21170, edited by J. Kadyk.
31. B. Andersson *et al.*, Phys. Rep. **97**, 31 (1983).
32. Electrons and muons are considered well identified if they satisfy the MARK II criteria for electron and muon candidates described in the section on event reconstruction.
33. The number of jets in the event is found by a MARK II utility program called JETCAL which uses sphericity and sphericity-like variables in its calculations.
34. M. Gyulassy *et al.*, Phys. Rev. C **20**, 2267 (1979).
35. M. Suzuki, Phys. Rev. D **35**, 3359 (1987).

36. H. Aihara *et al.*, TPC Collaboration, Phys. Rev. Lett. **54**, 270 (1985).

37. W. A. Zajc *et al.*, Phys. Rev. C **29**, 2173 (1984).

38. G. Goldhaber, PROCEEDINGS OF THE INTERNATIONAL CONFERENCE ON HIGH ENERGY PHYSICS, Lisbon, Portugal, July 9-15, 1981 (LBL-13291).

39. A. S. Davydov, QUANTUM MECHANICS, translated, edited, and with additions by D. ter Haar, Pergamon Press, London (1965).

40. G. Goldhaber, PROCEEDINGS OF THE FIRST INTERNATIONAL WORKSHOP ON LOCAL EQUILIBRIUM IN STRONG INTERACTION PHYSICS, edited by D. K. Scott and R. M. Weiner, World Scientific Publishing Co. (1985) (LBL-19417).

41. Y. Liu, Ph.D. Thesis, University of California, Riverside, (1985), (unpublished).

42. F. James and M. Ross, MINUIT, CERN program library D506/D516.

43. P. Avery *et al.*, CLEO Collaboration, Phys. Rev. D **32**, 2294 (1985).

44. M. Althoff *et al.*, TASSO Collaboration, Z. Phys. C **30**, 355 (1986).

LAWRENCE BERKELEY LABORATORY
TECHNICAL INFORMATION DEPARTMENT
UNIVERSITY OF CALIFORNIA
BERKELEY, CALIFORNIA 94720